A STUDY OF OPTOELECTRONIC PROPERTIES OF CARBON NANO MATERIALS: TRANSISTORS, SENSORS, AND BEYOND

By

YUNHAO CAO

Dissertation

Submitted to the Faculty of the

Graduate School of Vanderbilt University

in partial fulfillment of the requirements

for the degree of

DOCTOR OF PHILOSOPHY

in

Electrical Engineering

December, 2013

Nashville, Tennessee

Approved:

Prof. Yaqiong Xu

Prof. Daniel M. Fleetwood

Prof. Weng Poo Kang

Prof. Bharat Bhuva

Prof. Deyu Li

To my beloved wife and my parents

for everything

ACKNOWLEDGEMENT

This thesis would not have been possible without the financial support of the National Science Foundation (NSF), the technical support and research opportunities provided by the Vanderbilt Institute of Nanoscale Science and Engineering (VINSE), the Cornell Nanoscale Science & Technology Facility (CNF), the Center for Nanophase Materials Sciences (CNMS) at Oak Ridge National Laboratory (ORNL).

Each member of my Dissertation Committee has provided extensive professional comments and guidance on this research. First and foremost, I want to thank my advisor Dr. Yaqiong Xu, for her great support and encouragement during my Ph.D. study. She has shown such insightful expertise, and has provided me with the most important influence and most helpful guidance in my research. I would also like to express my deep gratitude to Dr. Weng Poo Kang, for his much-needed encouraging words and constructive advice. Special thanks are owed to Dr. Daniel Fleetwood, Dr. Bharat Bhuva and Dr. Deyu Li, for their thoughtful and instructive comments for this thesis.

I am grateful to all of those with whom I have had the pleasure to work during my Ph.D. study. I would like to thank my fellow lab mates, Tu Hong, Binbin Zhang, Roel Flores, for their friendship and assistance.

Finally, I want to thank my family, for their endless love and encouragement. I would not have accomplished this if it were not for my parents, who have been incredibly understanding and supportive. Last but not the least, I wish to thank my wife, for sharing my passion and being by my side and enjoying this life together. Thank you.

TABLE OF CONTENTS

Page

LIST OF FIGURES

LIST OF TABLES

CHAPTER 1

INTRODUCTION

1.1 Introduction to carbon nanomaterials

The study of nanomaterials has quickly spread around the world since the starting of the 21st century. It opens a new era in science and all of a sudden, it becomes a fashion and researchers in all fields try to dig out the hidden treasure in this unknown continent. So why is nanomaterial so fascinating? Nanomaterial refers to the materials with morphological features with the metric length of 10^{-9} m. Comparing to traditional materials, such materials could be significantly influenced by quantum size effect and exhibit some superior electrical, mechanical and optical properties.

Among all the nanomaterials, the carbon nanomaterials are indubitably the most popular members. They have been the topics for thousands of studies in all fields including physics, chemistry, engineering, and medicine, which have lead to the winning of three major science awards so far. Richard Smalley, Sir Harold Kroto, and Robert Curl won the Nobel Prize in chemistry in 1996 for the discovery of C_{60} buckyballs (first row in Figure 1.1). Sumio Iijima won the Kavli Prize in nanoscience in 2008 for carbon nanotube (CNT) characterizations (second row in Figure 1.1). Recently, Andre Geim and Konstantin Novoselov developed a feasible technique to obtain high quality pristine graphene which led to the research booming of this two dimensional material (third row

in Figure 1.1). They won the Nobel Prize in Physics in 2010 for their contributions to graphene.

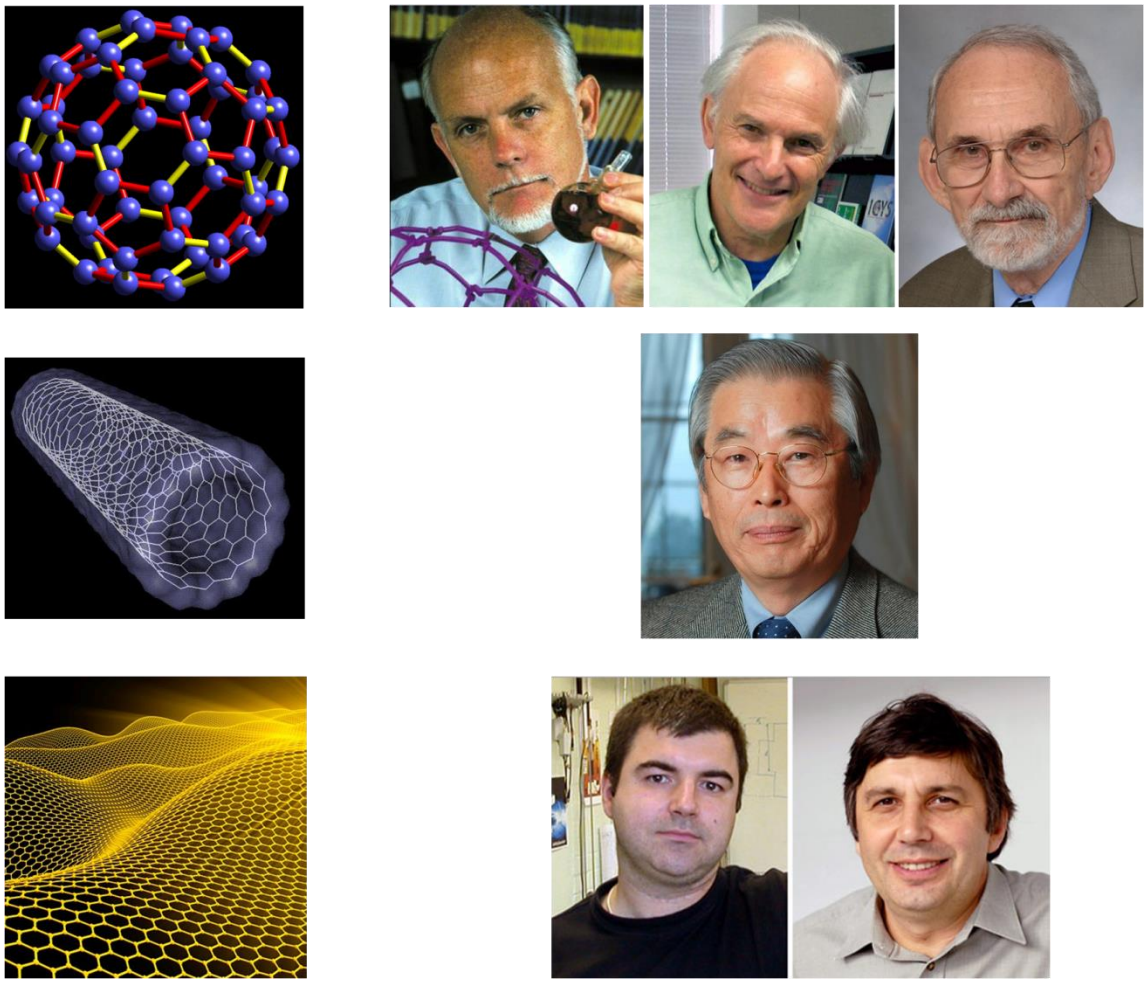

Figure 1.1 Carbon nanomaterials and their discoverers. First row: C60 buckyball (www.godunov.com) and Richard Smalley, Sir Harold Kroto, Robert Curl; Second row: CNT (davemark.com) and Sumio Iijima; Third row: graphene (i.telegraph.co.uk) and Andre Geim, Konstantin Novoselov.

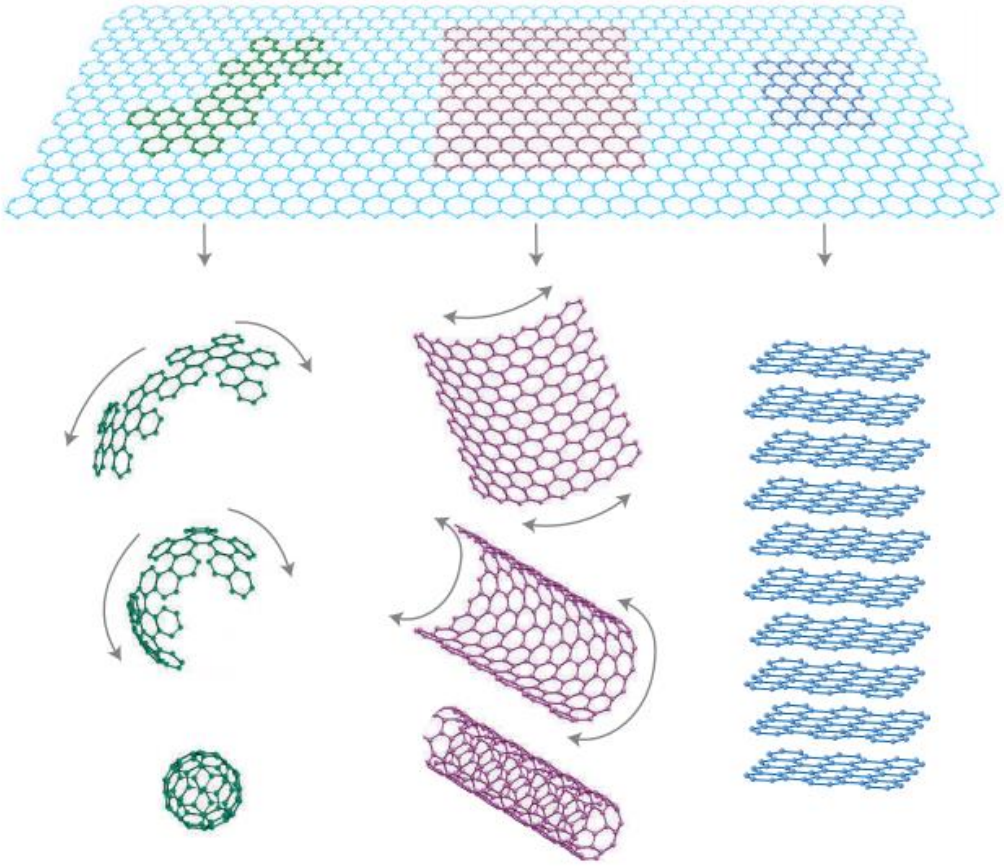

Figure 1.2 Three typical forms of carbon nanomaterials[1]

The reason why nano-carbon family is so intriguing is that they are all allotropes of carbon but with different ways of folding (Figure 1.2), which gives them unique and extraordinary properties. C_{60} buckyball is a spherical fullerene molecule with a size of few nanometers. It is hence considered as a zero dimensional system. Though small, the nanoscale "soccer ball" has bound large numbers of hydrogen atoms within a single molecule, showing a great potential to be the medium of accessible hydrogen fuel[2]. Instead of folding into a sphere, when the single graphitic plane was curled up into a tube with a diameter in nanometers, we could obtain a one-dimensional system called CNTs.

Compared to buckyballs, CNTs show great potential in many application fields due to their superior electrical, optical and mechanical properties that exceed the conventional materials. The single graphitic plane itself makes another carbon allotrope referred as graphene. Graphene also exhibits appealing electrical, optical and mechanical properties. The versatile and integratable nature of this two dimensional material makes it a more feasible option for future electronics. This thesis is devoted to explore the optoelectronic potentials of carbon nanomaterials. Thus CNTs and graphene will be the main topics. More details about the structures and properties of these two carbon nanomaterials will be introduced in this chapter.

1.2 Carbon nanotubes (CNTs)

CNTs are one-dimensional materials with cylindrical nanostructures. The diameter of a typical CNT is normally in the nanometer scale, but the length of the CNT could go to the centimeter scale[3]. As hollow cylinders made from single graphene sheet, CNTs have presented tremendous surface-to-volume ratio. CNTs also exhibit excellent mechanical, optical and electrical properties, which make them a very promising material in many application fields, such as energy storage, sensing, future very-large-scale integration (VLSI), etc.[4-7]

1.2.1 Structure of CNTs

A single-walled CNT could be visualized as a rolled-up single atomic layer of graphite. The way how the carbon atoms arrange themselves along the circumference of

the CNT is described by chirality. The vector, along which the single layer graphite (graphene) is rolled, is called the chiral vector C_h. As illustrated in Figure 1.3 A, the chiral vector is usually specified by two lattice vectors of graphene in real space, that is, $\mathbf{C_h} = n\mathbf{a_1} + m\mathbf{a_2}$.

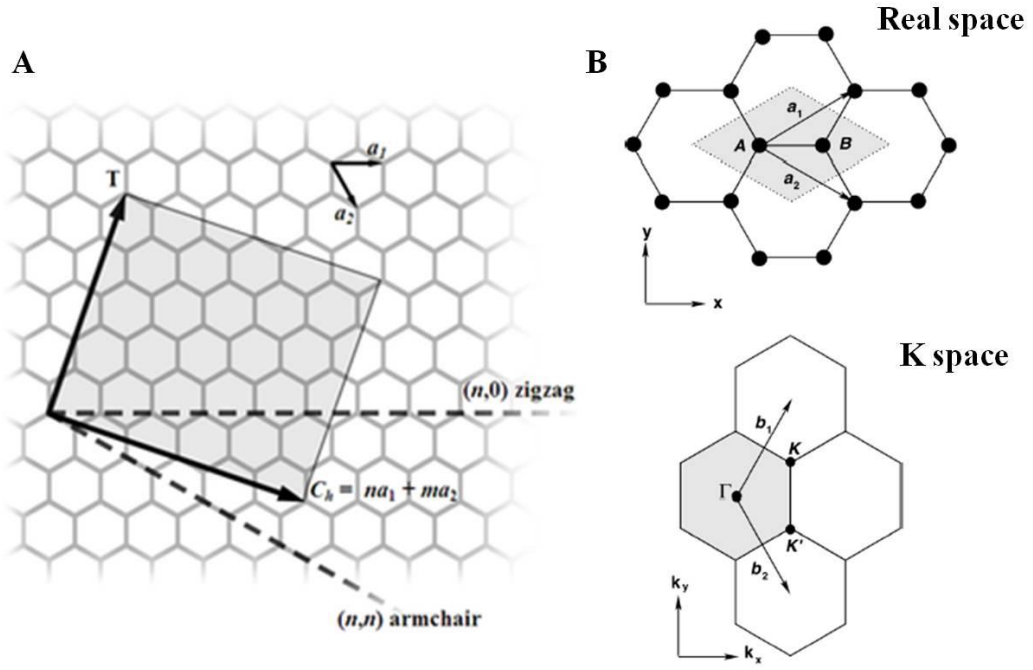

Figure 1.3 (A) the naming scheme for CNTs; T denotes the tube axis, a_1 and a_2 are the unit vector of graphene in real space[8]. (B) the lattice structure of a unrolled CNT, or graphene, in both real space and K space[9]. In the real-space lattice, the lattice vectors $\mathbf{a_1} = (\frac{a\sqrt{3}}{2}, \frac{a}{2})$, $\mathbf{a_2} = (\frac{a\sqrt{3}}{2}, -\frac{a}{2})$. The corresponding lattice vectors in K-space $\mathbf{b_1} = (\frac{2\pi}{a\sqrt{3}}, \frac{2\pi}{a})$, $\mathbf{b_2} = (\frac{2\pi}{a\sqrt{3}}, -\frac{2\pi}{a})$. The shaded area shows the first Brillouin zone.

Generally, a single-walled CNT is named by a pair of indices (n,m). For instance, when m = 0, the resulting structure is named as zigzag; similarly, the armchair structure refers to the circumstance where n = m. The values of the (n,m) indices are very important parameters for CNTs. They not only specify the structure of a CNT, but also determine whether a CNT is semiconducting or metallic. By applying the periodic boundary conditions, we obtain that if the wavevector $\boldsymbol{k}$ (the component of the momentum along the circumference of the CNT) passes the K point of graphene (Figure 1.1 B), where the conduction band meets the valence band, the following equation could be drawn

$$\boldsymbol{C_h} \cdot \boldsymbol{k_K} = 2\pi\left(\frac{2}{3}n + \frac{1}{3}m\right) = 0 \; mod \; 2\pi \tag{1}$$

Once equation (1) is satisfied, the resulting CNTs will be metallic. Otherwise, we will have semiconducting CNTs.

1.2.2 Physical properties of CNTs

The one-dimensional nature of CNTs strongly affects their electrical properties. Electrons in CNTs are confined in the direction perpendicular to the tube axis and can only propagate along the tube axis. The electron mobility of CNTs exhibits an extraordinary value of more than 100,000 $cm^2/V{\cdot}s$ at room temperature[10]. In theory, if quantum resistance is the only resistance considered, the electron transport in CNTs could be ballistic.

As previously introduced, the type of CNTs depends on the structure of the CNTs and how they arrange themselves along the tube axis. Once the chiral vector is known, the type of the nanotube and its diameter is determined. In another word, the physical properties of CNTs are strongly related with their diameters. According to the theoretical calculation, the band gap energy of a semiconducting nanotube could be expressed as:

$$E_g = 2\gamma_0 a_{c-c}/d \tag{2}$$

where γ_0 is the nearest-neighbor overlap integral and a_{c-c} is the lattice constant of a graphene layer.[11] This result was experimentally proved in 1998,[12] where both the chiral angles and the tube diameters were precisely measured by high resolution scanning tunneling microscopy to determine the chiral vector (n,m). By linking the correlations between atomic structures of CNTs and their electronic properties, they found a good agreement with the theoretical calculations. The correlation between the diameter and the band gap energy makes semiconducting nanotubes a very promising material in electronic applications, since their band gaps are highly modifiable if the chiral numbers of as-grown CNTs can be controlled as desired. Although controlling the chirality of CNTs remains to a very difficult topic, the recent success regarding the highly preferential growth of CNTs with certain chiral indices shines a light in the future study.[13, 14]

Recently the researchers at Cornell University found that in a CNT photodiode, a single photon was able to excite multiple electron-hole pairs at low temperature, exhibiting unprecedented photo-conversion efficiency.[15] In their work, a PN junction was created within a single CNT transistor by inserting the split-gate beneath the tube which

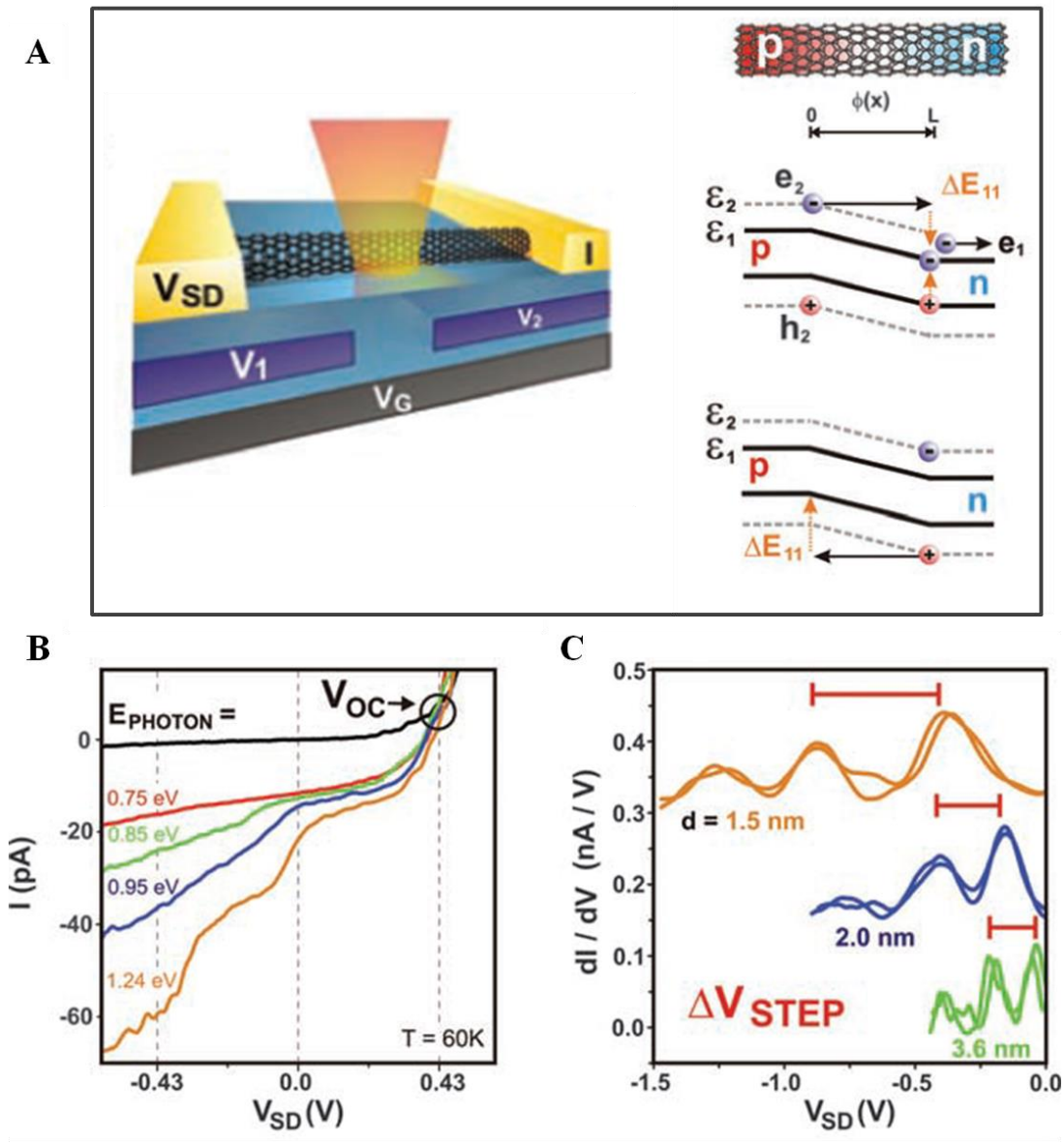

Figure 1.4 Extremely efficient electron-hole generation in carbon nanotube photodiodes[15]. (A) Schematic diagram for the carbon nanotube photodiode and the energy diagram for the mechanism of possible pathways for electron-hole generation; (B) I-Vsd behaviors at T = 60K at different photon energies; (C) The Vsd spacing for nanotubes with different diameters.

could electrostatically dope the nanotube transistor (Figure 1.4 A). They found that the I-Vsd curve of the nanotube photodiode exhibited distinct behaviors with various photon energies at reverse bias, which indicated that multiple electron-hole pairs were generated during the process (Figure 1.4 B). This phenomenon was further found to be related with the tube diameters (Figure 1.4 C), a strong evidence to link the excitation with the band gap energies. This new discovery has broken the standard limit in photovoltaic devices established by Shockley and Queisser[16], where they demonstrated that only one electron-hole pair could be generated by one photon. This physical potential of CNTs may lead to the development of next-generation ultra-efficient photovoltaic devices.

1.2.3 CNT growth

The first successful synthesis of CNTs can be dated back to 1991, when they were observed after an arc discharge process using graphite as the carbon source. Since then, a number of studies have been conducted systematically, and many techniques have risen to produce CNTs in highly controllable manners. Large quantities of CNTs can be synthesized through these methods, which make them a commercially viable carbon nanomaterial. Among all the synthesis techniques, chemical vapor deposition (CVD) is a very commonly used method for CNT growth in many research groups and commercial companies, because of its simplicity and high repeatability. CVD is also one of the best methods to produce nanotubes with minimal defects and mass production. Therefore, CVD is the growth method that we mainly focus on in this thesis.

The CVD growth of CNTs is usually considered as an in-situ growth because the resulting nanotubes are synthesized exactly on the intended sites. Shown in Figure 1.5 are two widely accepted CNT growth mechanisms: tip-growth and base-growth.[17] During a typical growth process, the carbon containing gases, also referred as the *precursor*, will decompose into carbon and hydrogen species at high *temperature*. With the help of the *catalysts*, which are normally metal nanoparticles, the carbon will dissolve into the metal and further precipitate into cylindrical carbon networks. The growth process will continue unless the catalysts get deactivated.

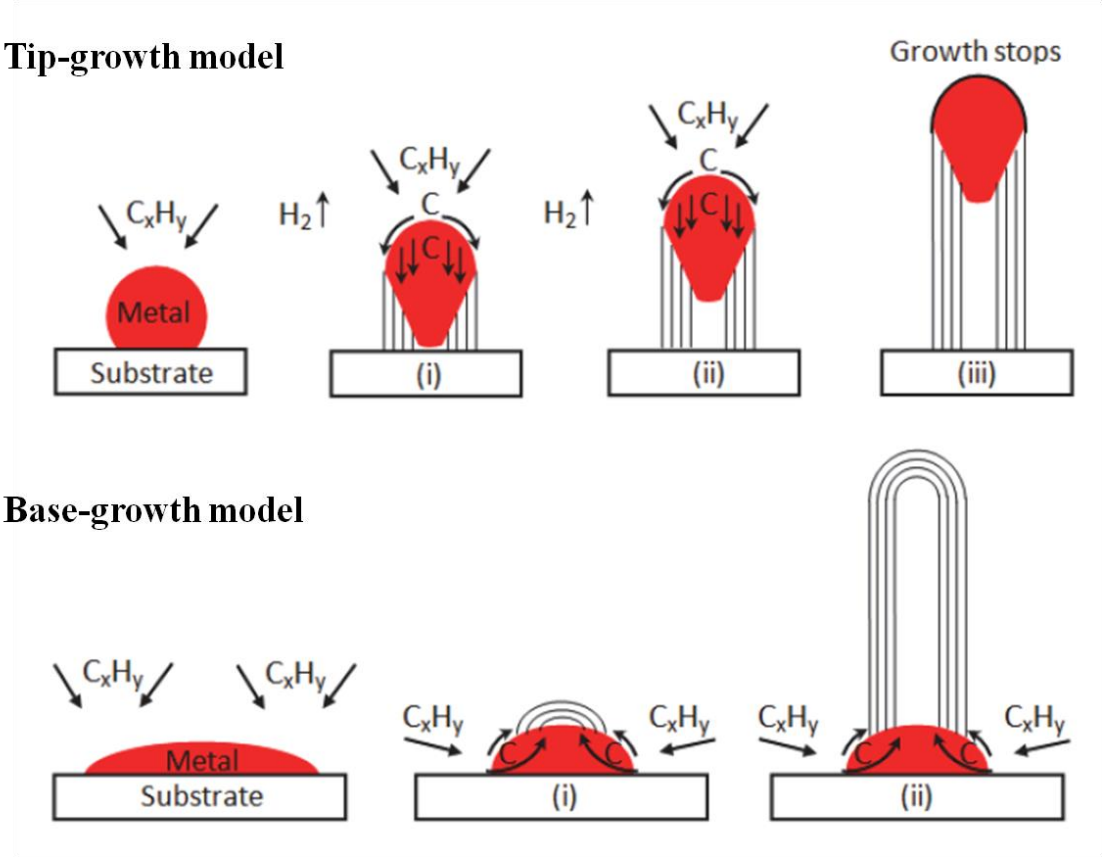

Figure 1.5 Widely accepted models for CNT growth mechanism[17]

Many parameters could influence the outcome during a typical CVD growth process. One important parameter is the precursor, which acts as the carbon source during the growth. The common precursors used in the CVD process are normally carbon containing vapors, including methane, acetylene, ethylene, carbon monoxide, benzene, etc. However, inert gases through carbon containing liquid bubblers (such as ethanol, methanol) could also serve as alternative precursors. Different precursors may result in different amount of by-products after the CVD process. For instance, acetylene is always a tricky precursor to control since it easily brings along high amorphous carbon contaminations after the growth, while ethanol is known as a clean carbon source that produces nanotubes free of amorphous carbon[18]. Besides, recent studies have also shown that the molecular structures of the precursors may also determine the resulting morphologies of CNTs[19], suggesting that a more prudent choice of precursors should be made depending on what kind of nanotubes is wanted for the growth. In 2004, it was found that by introducing water during the CVD process, the growth efficiency could be significantly increased to an unprecedented level[20]. This water-assisted high efficient growth is also known as the "super-growth". Water plays as a growth enhancer in this process to selectively etch the amorphous carbon and extend the lifetime of catalyst. Other compounds such as carbon dioxide and acetone could also act as the growth enhancer.[21]

Catalyst is another important issue for CNT growth. It could be related with the morphology, diameter, and distribution of the resulting CNTs. The diameter of the CNTs highly depends on the size of the catalysts, or the thickness of catalyst films. Figure 1.6 lists the commonly used CNT catalysts, including Fe, Fe-Mo, Ni, Cu, Pb, etc. Although

CNTs are able to be grown by these catalysts, the density and the level of alignment of resulting CNTs vary from one to another. Among all the catalysts, Fe and Fe-Mo are most widely used due to their high efficiency and easy preparation. Cu is another important catalyst since it exhibits a superior ability to grow single-walled CNTs. The carbon solubility on Cu is low, which greatly reduces the chances of multi-walled CNTs

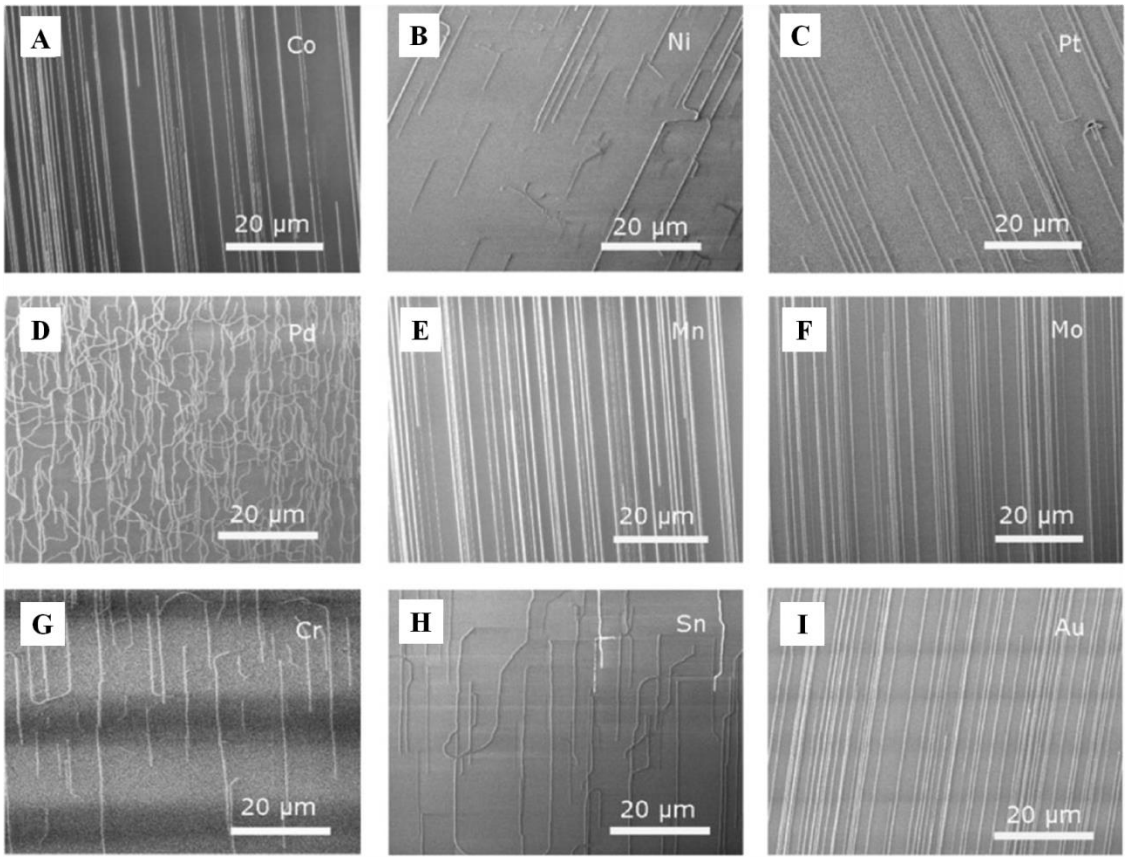

Figure 1.6 SEM images of horizontally aligned single-walled CNTs on ST-cut quartz[22] by different catalyst: (A) Co; (B) Ni; (C) Pt; (D) Pd; (E) Mn; (F) Mo; (G) Cr; (H) Sn; (I) Au.

and amorphous carbon. However, the weak catalyst activity of Cu also leads to a low efficiency of growth. Pb is also an efficient catalyst for growing single-walled CNTs. The solubility of carbon in Pb is very similar to that of Cu. More importantly, it has been shown that the single-walled CNTs grown by Pb are free of metal contaminants, which could be attributed to quick evaporation of Pb nanoparticles during the synthesis process.[23]

1.3 Graphene

Graphene is a two dimensional material that consists of a single layer of tightly bonded carbon atoms in hexagonal patterns. Due to the exceptional electrical, optical and mechanical properties, graphene has quickly become one of the most popular materials in science and engineering fields. Its potential applications currently being studied range from next-generation electronics[24], supercapacitors[25], to biomedical uses[26]. In this section, we will introduce the basic structures and optoelectronic properties of graphene and review the general methods to obtain graphene.

1.3.1 Structure of graphene

In graphene, carbon atoms are bonded in honeycomb structures with sp^2 hybridization. The monolayer carbon structure with honeycomb lattice is actually the basic building block for other carbon allotropes. The 1D CNTs and 3D graphite all originate from the 2D single layer graphene. As illustrated in Figure 1.7 A, each carbon

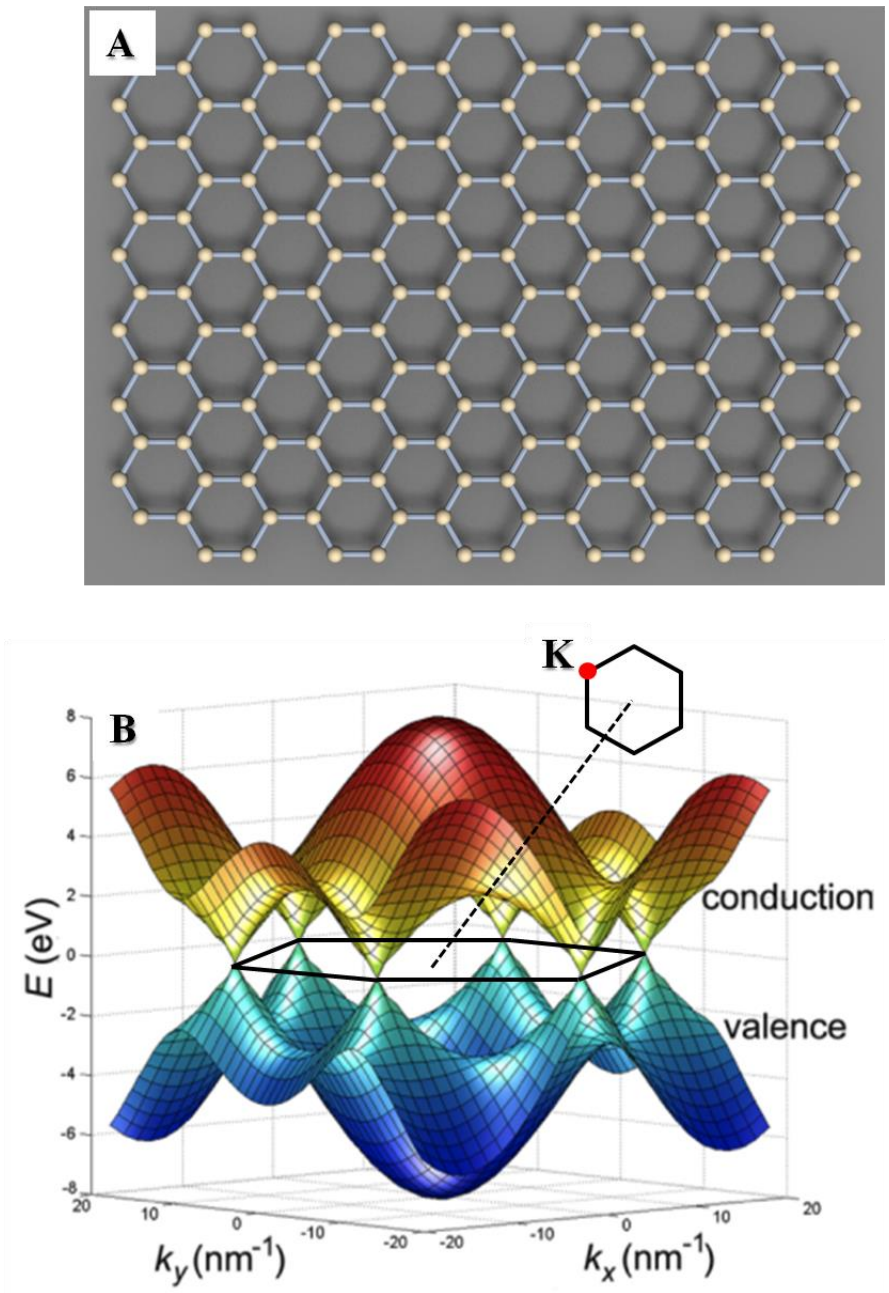

Figure 1.7 (A) The carbon atom arrangement in graphene[27]; (B) The band structure of graphene in k-space[28].

atom in graphene has three covalent bonds, with a separation of 1.42 angstrom in the x-y plane. The covalent C-C bonds are the second strongest carbon bonds, nearly equivalent to the covalent bonds that hold carbon atoms together in diamond, which is known to be one of the hardest materials in nature. The fourth valence electron of each carbon atom that does not participate in the covalent bonding binds with the nearest neighbors to form the π orbitals, which make graphene conducting.

Graphene is normally considered as semi-metal, since the conduction band and valence band meets at certain points in the k-space. Figure 1.7 B shows band structure obtained by tight binding-approximation. The points where the conduction band and valence band meets are referred as the Dirac points, or the K points. The band structures near the Dirac points disperse linearly as cones, which are very similar to the energy dispersion of massless photons.

1.3.2 Physical properties of graphene

The unique band structure of graphene provides an ideal platform for electron transport. Unlike traditional materials, where the charge carriers become immobile at low temperature as a result of the low density, the carrier mobility in graphene remains high and has been reported to reach 200,000 $cm^2 V^{-1} s^{-1}$ due to the reduced scattering.[29]

The 2D nature and zero band gap property of graphene also affect its optical properties. As shown in Figure 1.8, the optical transmission of single and double layer graphene was measured accordingly.[30] Although graphene is only one atom layer thick, it was found to absorb a significant fraction of light. The exactly same amount of white

light was absorbed by each layer. The optical absorption (A) was found to be solely defined by the fine structure constant and follow a simply relation:

$$A = \pi\alpha = 2.3\% \tag{3}$$

where the fine structure constant α = 1/137. The strong interaction with light is also the reason why graphene is visible on silicon chips.

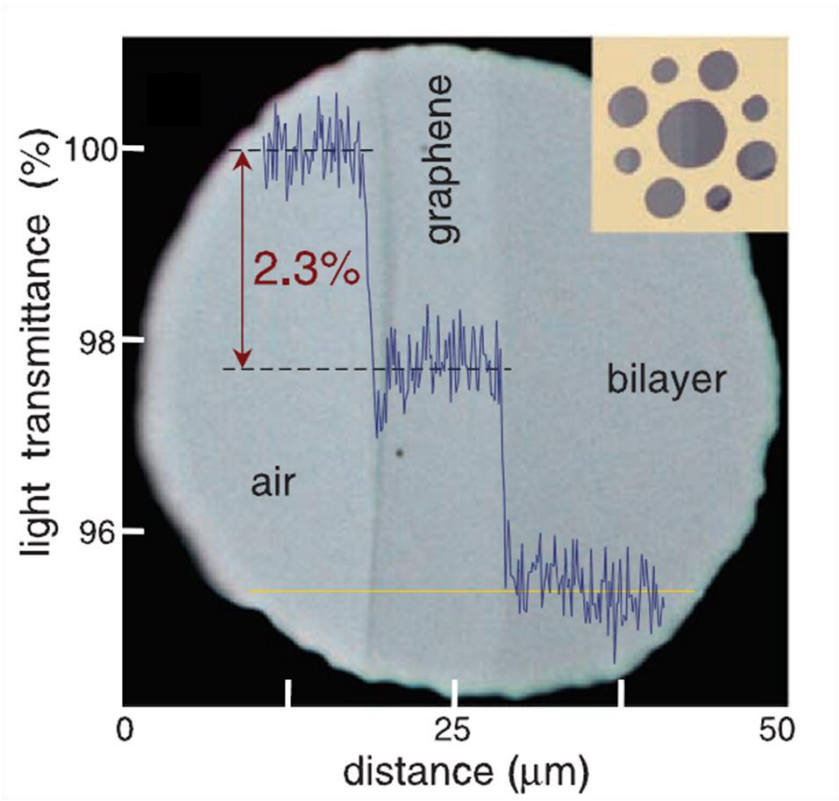

Figure 1.8 The light transmittance through the one layer thick, and two layer thick suspended graphene. Each layer absorbs 2.3% of the light[30].

1.3.3 Graphene synthesis

Although early studies relevant to graphene date back to the 1960s[31], the extensive studies towards graphene did not begin until the facile technique for isolating graphene from bulk graphite was developed in 2004[32]. The idea for this technique is simple. Highly ordered pyrolytic graphite (HOPG) is usually used as the source for graphene, and is rubbed onto Scotch tapes. The remaining HOPG fragments on tapes are then cleaved repetitively until thin films of graphene are found under the microscope. This Scotch tape technique, also referred as the mechanical exfoliation method, is very easy to achieve and could provide high purity graphene. However, the size of the graphene provided by this method is limited in micrometer scale, and the positions of good graphene membranes are also arbitrarily scattered on the substrate.

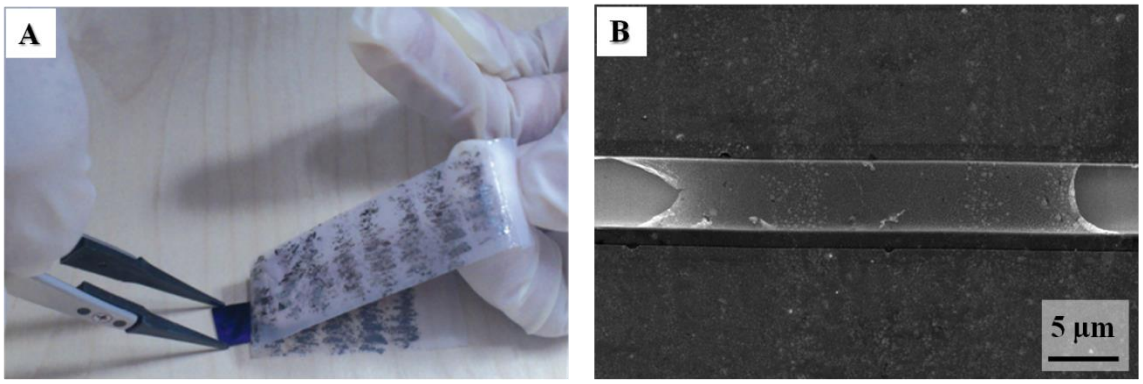

Figure 1.9 (A) Mechanical exfoliation method to cleave graphene by Scotch tapes[33]; (B) SEM image for CVD grown graphene with a scale bar of 5 µm.

The CVD method, which could produce graphene in larger scale, was developed a few years later[34, 35]. The resulting graphene through CVD could reach the centimeter

scale. The CVD method normally involves the use of carbon-containing gases and catalytic substrates. Depending on the conditions, CVD could produce either single-layer or few-layer graphene. Compared to the classic Scotch method, CVD is more advanced in aspects of large scale production, stability and controllability. However, due to the potential chemical contaminations, the quality of graphene from CVD may not be as good as that from the Scotch tape method.

1.3.4 Graphene transfer after growth

After the growth, we have to get graphene off the copper foils and transfer it to the desired substrates. Several groups have developed reliable transfer techniques to facilitate this process. A common method is the wet transfer technique, in which a PMMA layer is deposited on top of graphene/copper foil to hold the graphene while the copper foild is hence etched away by the copper etchant.

The basic steps are illustrated in Figure 1.10. Graphene was grown on top of the copper foils after the CVD process. Then the graphene/copper foil would be cut again into the desired size for each use (normally 1 cm squares). We spin-coated a thin layer of PMMA on the top of graphene/copper foil which applied good adhesion with graphene. The copper was hence etched away by soaking the sample in ion nitride solution for 1 hour. During this process, graphene was kept intact by the thin PMMA film. The PMMA/graphene film would be scooped up and tranferred to water baths and kept at least 5 minutes for rinsing, which was repeated for at least 3 times to completely clean the film. After rinsing, PMMA/graphene was floated to the desired substrate and dried in

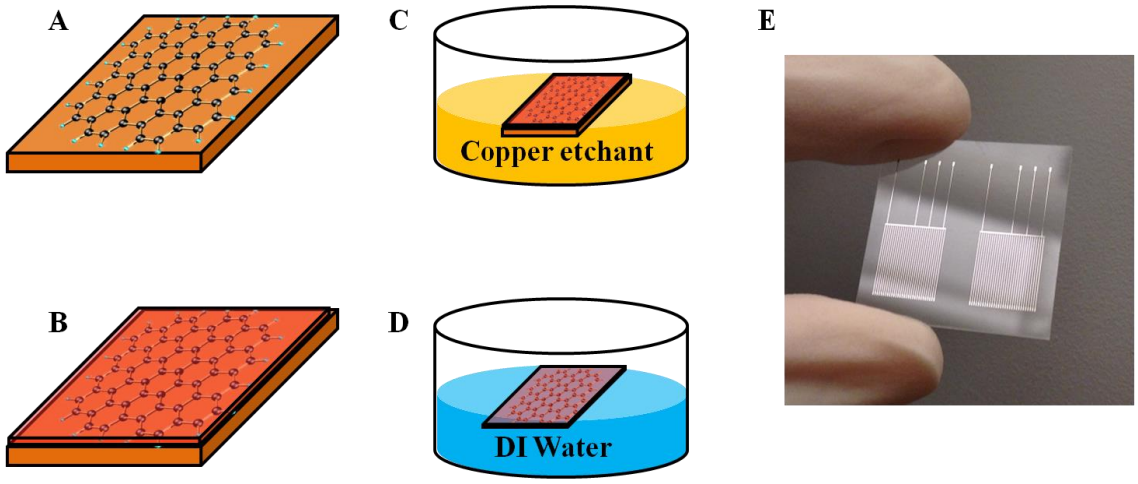

Figure 1.10 Graphene transfer process (A) Graphene sample after growth; (B) Graphene sample with a thin PMMA film coated on; (C) Wet etching to remove copper beneath graphene; (D) Water baths to clean the sample; (E) The target substrate to transfer graphene onto.

air. PMMA could be removed by either annealing in furnace at 400 °C, or soaking in acetone for 30 minutes.

1.3.5 Raman characterization

Raman spectroscopy is a laser-based spectroscopic technique to collect the information about vibration modes in the material system. By shining the laser with the proper wavelength on the material, Raman spectroscopy is able to detect the shift of the laser energy induced by the interaction between the the laser light and molecular

vibrations in the material. It could reveal plenty of intrinsic properties of graphene, such as the quality and the layer number. Generally, for pristine single layer graphene, the D peak at ~1350 cm^{-1} is nearly invisible. The shape of 2D peak at ~2700 cm^{-1} is very sharp. When compared with the G peak at ~1580 cm-1, whose height increases significantly with the the layer number of graphene, 2D/G ratio is greater than 1 for single layer graphene.

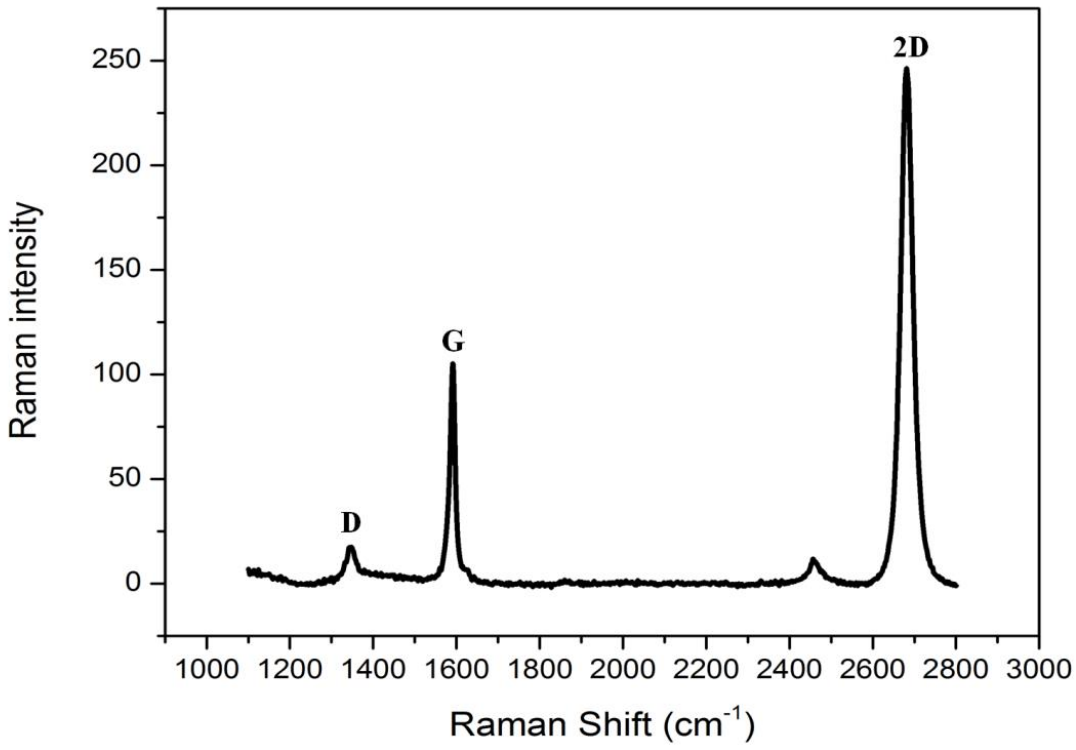

Figure 1.11 A typical Raman spectrum of graphene after the transfer process

In order to inspect the qualify of the CVD grown graphene, Raman spectroscopy has been performed for post-transfer characterization of graphene. A 532 nm excitation laser was focused by a 100X, 0.9 NA objective to provide a 1 μm diameter diffraction-

limited laser spot. As shown in Figure 1.11, the presence of the D peak indicates that there exists some degree of disorder, which is probably owing to the contaminations from the remaining residues of chemical solvents during the transfer process.

1.4 Outline of thesis

This chapter has presented an introduction to the properties, background and research motivations of carbon nanomaterials. The objective of the thesis is to combine synthesis, fabrication techniques and various characterization tools to investigate the optoelectronic properties of carbon nanomaterials, and explore their potential future applications. The main content consists of two topics, CNT and graphene. The synthesis and fabrication techniques are studied in order to produce high-quality and controllable devices, and potential application in optoelectronics is further investigated.

The first topic we discuss is CNTs. Chapter 2 describes the synthesis techniques that we developed to control the growth morphology and density of CNTs by CVD. Two different strategies are demonstrated to grow single-walled CNTs from suspended bridges to upright forest. Based on the synthesis techniques, we further build a platform to create CNT biosensors in Chapter 3. Suspended CNT transistors are used as nanoscale optoelectronic probes to investigate the electrical and optical processes in biological systems.

The second topic we study is graphene. In Chapter 4, we demonstrate a facile and reliable method to engineer the CVD-grown graphene membrane and change its morphology. The resulting curled graphene ribbons (CGRs) have exhibited distinct

optoelectronic properties compared with pristine graphene. Different factors that influence the formation of CGRs have been systematically studied to produce this novel structure in a controllable way. In Chapter 5, we further look into the optoelectronic properties of the new graphene structure. CGR based transistors have been fabricated and various characterization tools, such as Raman microscopy, SEM, gate-dependent scanning photocurrent microscopy, etc., have been utilized to investigate the mechanism of the photocurrent generation in CGR devices. The curling of graphene has been found to enhance the photocurrent response by two orders of magnitude. Unlike common optoelectronic devices, the photocurrent generation in CGRs is significantly influenced by the photothermoelectric effect.

CHAPTER 2

CONTROLLING GROWTH MORPHOLOGY OF CNTS

2.1 Overview

Over the years, many techniques have been developed for CNT growth, such as arc discharge[36], laser ablation[37], and chemical vapor deposition (CVD)[38]. Among them, CVD has been widely used for CNT synthesis due to the low cost and the essence of simplicity for wafer-scale production. During a typical CVD process, a sample with catalyst, mostly iron or nickel, will be put in a furnace and heated up to the desired temperature with the presence of carbon-containing gases. Depending on the conditions and the substrate used, the resulting CNTs could be in different forms, as shown in Figure 2.1.

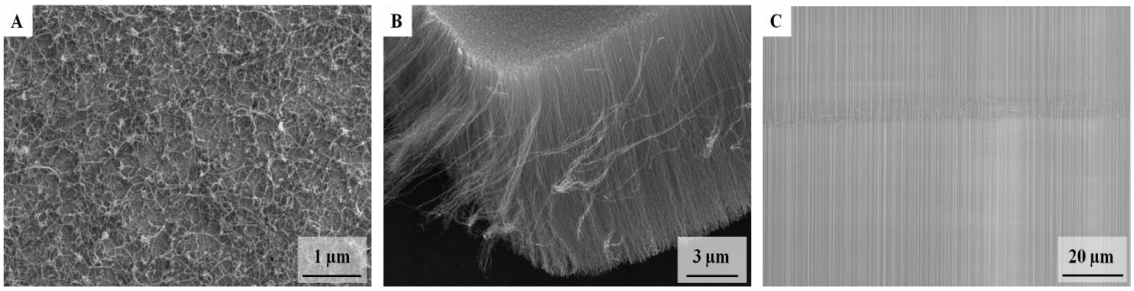

Figure 2.1 (A) randomly grown CNT surface network; (B) vertically-aligned CNT forest; (C) horizontally-aligned CNT arrays. Credit Roel Flores.

Various forms of CNTs grown by CVD have been reported to meet the usage for different purposes. For instance, surface growth of CNTs has been investigated and normally utilized to fabricate nanoscale biosensors or suspended CNT transistors which are promising for future electronics;[39-41] Water-assisted and plasma-enhanced CVD methods have been developed to produce vertically-aligned CNTs,[42-44] also known as CNT forests or CNT carpets, which are intriguing for their potentials in large varieties of electronic applications such as supercapacitors, touch screens and building blocks of integrated circuits.[45-47] All-CNT field-effect transistor devices that assemble both horizontally- and vertically-grown CNTs in complex three-dimensional structures have also been reported, in which horizontal CNT arrays and vertical CNT forests were prepared through two different growth procedures.[48] Nevertheless, few studies have been done regarding the integration of various growth morphology in a controllable way.

In this chapter, we present two different strategies to control the growth tendancy of CNTs and thus to provide various forms of CNT growth with the same catalyst preparation. We have observed the CNTs evolving from surface growth to forest growth by changing the acetylene pulse introduced at the beginning of growth, or by adjusting the growth temperature. We have also managed to produce CNT surface growth and forest growth simultaneously within a single growth procedure. In addition, Raman spectroscopy has been performed to characterize the properties of as-grown CNTs under different conditions. On the basis of Raman spectroscopic results, the effect of the two growth strategies on CNT quality has been investigated and the correlated growth mechanisms have also been discussed.

2.2 Materials and methods

2.2.1 Device fabrication

For the preparation, catalyst pads that consist of 0.4 nm Fe catalytic nanoparticles and a 10 nm intermediate layer of Al_2O_3 were deposited on top of Pt electrodes by e-beam evaporation. The presence of Al_2O_3 will lead to more nucleation sites hence improve the efficiency of catalytic nanoparticles during the growth.[41] In order to investigate the capability of horizontal growth for CNTs and rule out the substrate interference, a trench was etched between the catalyst pads.[49] CNTs will be synthesized on the catalyst pads in terms of either surface growth or forest growth.

2.2.2 CVD synthesis of CNTs

The CNT growth was implemented via "fast-heating" CVD process under atmospheric pressure in a quartz tube in a horizontal furnace system.[50] After purging the system with argon, the sample was heated up to 700 °C and treated for 10 minutes with water vapor introduced by passing argon (100 sccm Ar) through a water bubbler in order to oxidize Fe catalysts and to eliminate potential contaminants. The annealing procedure was then performed for 15 minutes under a hydrogen atmosphere (200 sccm H_2) at the same temperature to reduce the oxidized catalysts to a proper state for subsequent CNT growth procedure. After the annealing, the sample was taken out for cooling at room temperature and the furnace was ramped up to the growth temperature. The fast-heating step was achieved by rapidly inserting the sample into the center of the furnace when the

desired growth temperature was reached. From here, two different growth strategies would be used. A short pulse of acetylene (0.5 sccm C_2H_2) was added at the beginning of the growth under the growth temperature of 865 °C for the first strategy, while the second strategy only changed the growth temperature from 865 °C to 1015 °C with a constant flow of acetylene (0.5 sccm C_2H_2). For both strategies, a constant methane-hydrogen mixture (800 sccm CH_4, 200 sccm H_2) were introduced into the system throughout the growth procedure. The samples were rapidly cooled down to the room temperature after the growth.

2.3 Results and discussion

2.3.1 The influence of acetylene pulse

Samples prepared by CVD process have been imaged under scanning electron microscopy (SEM). In the first strategy, the growth temperature was set at 865 °C and an acetylene pulse was introduced at the beginning of the growth process. During a typical CVD process without acetylene pulse, CNTs were grown on surface with the length of micron size (Figure 2.2A) at a low yield. However, when a short pulse of acetylene was introduced into the system, the yield of CNTs would be considerably enhanced (Figure 2.2B and 2.2C). This can be attributed to the much higher carbon feeding rate provided by acetylene than that of methane. Acetylene has been known to be able to decompose in a single collision reaction and provide direct pathway to carbon incorporation during CNT growth.[51] Consequently, it is more capable to activate catalytic nanoparticles during

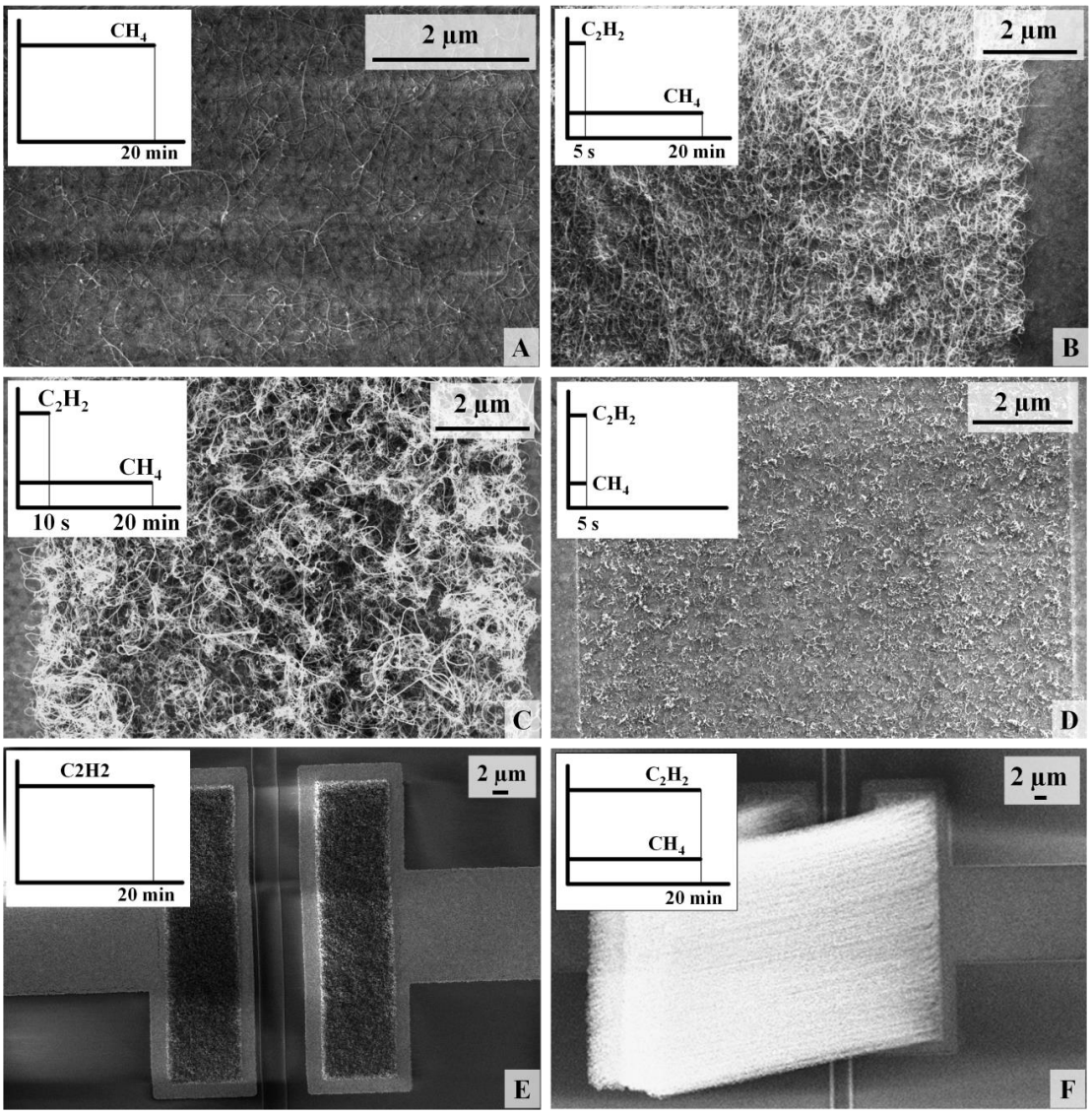

Figure 2.2 SEM images with samples under different gas feeding conditions at 865 °C, as indicated in corresponding insets. (A) CH_4 only for 20 min; (B) 5 s C_2H_2 pulse and constant CH_4 for 20 min; (C) 10 s C_2H_2 pulse and constant CH_4 for 20 min; (D) Constant C_2H_2 and CH_4 for 5 s; (E) C_2H_2 only for 20 min; (F) Constant C_2H_2 and CH_4 for 20 min.

the nucleation stage, which has been generally considered to be critical for the growth initialization.[52-55] As a result, the introduction of a short-time acetylene pulse would significantly affect the following growth stage, and boost the yield of CNT growth. This idea is positively illustrated by Figure 2.2D, where acetylene and methane have been applied together for a short growth time of 5 s, which is roughly the nucleation time. Though only short CNTs have been found, the high density distribution indicates the successful activation of large numbers of catalytic nanoparticles. However, we found that if acetylene was serving as the only carbon feeding source applied into the system during growth, CNT forest growth in absence of length would take place (Figure 2.2E). As shown in Figure 2.2F, where dense CNT forests were formed by introducing both acetylene and methane as carbon feeding source for the entire growth process, it is obvious that though much less effective in terms of activating catalytic nanoparticles, methane is efficient to extend the length of CNTs.

2.3.2 Fabricating suspended CNT transistor through pulse controlled strategy

We have also investigated the probability of growing suspended CNT transistors through this C_2H_2 pulse controlled strategy. A simple design has been made to prepare the acetylene pulse of 5 s many CNTs grow across the trench bridging two metal contacts underneath the catalyst pads (Figure 2.3 B). The electrical measurements that determine whether the two metal contacts are connected by CNT bridges have shown an average yield above 60% of conductive devices, exhibiting excellent efficiency of producing

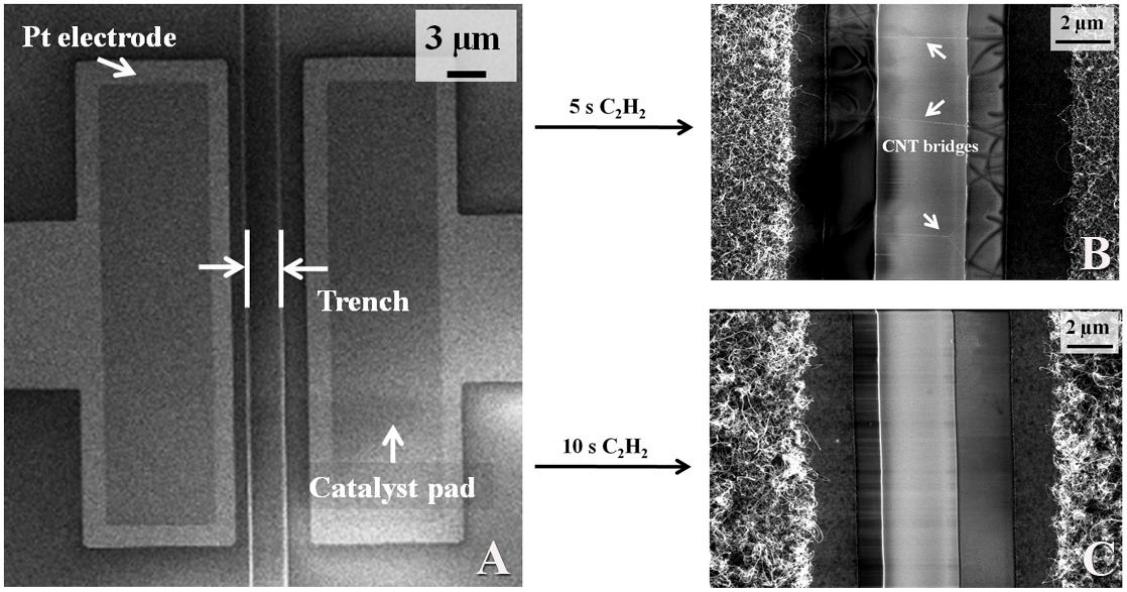

Figure 2.3 (A) Top view of a pre-treatment device intended for the growth of suspended CNT transistors. (B) Zoom-in trench view shows horizontal CNT-bridge structures (pointed by white arrows) with 5 s C_2H_2 pulse and constant CH_4 for 20 min; (C) Zoom-in trench view with 10 s C_2H_2 pulse and constant CH_4 for 20 min, no horizontal CNT-bridge structure is observed.

suspended CNT transistors. The yield of horizontal CNT transistors substantially degraded when the acetylene pulse time was extended to 10 s (Figure 2.3 C), owing to the increasing yield of vertically-aligned CNTs. Furthermore, from previous observations we have found that if the acetylene pulse is introduced together with methane for the entire growth procedure, it will result in full CNT forest growth instead of surface growth. These experiments have elucidated that the growth tendency and morphology of CNTs can be changed after a considerable dose of acetylene is involved into the growth process.

2.3.3 The role of temperature during growth

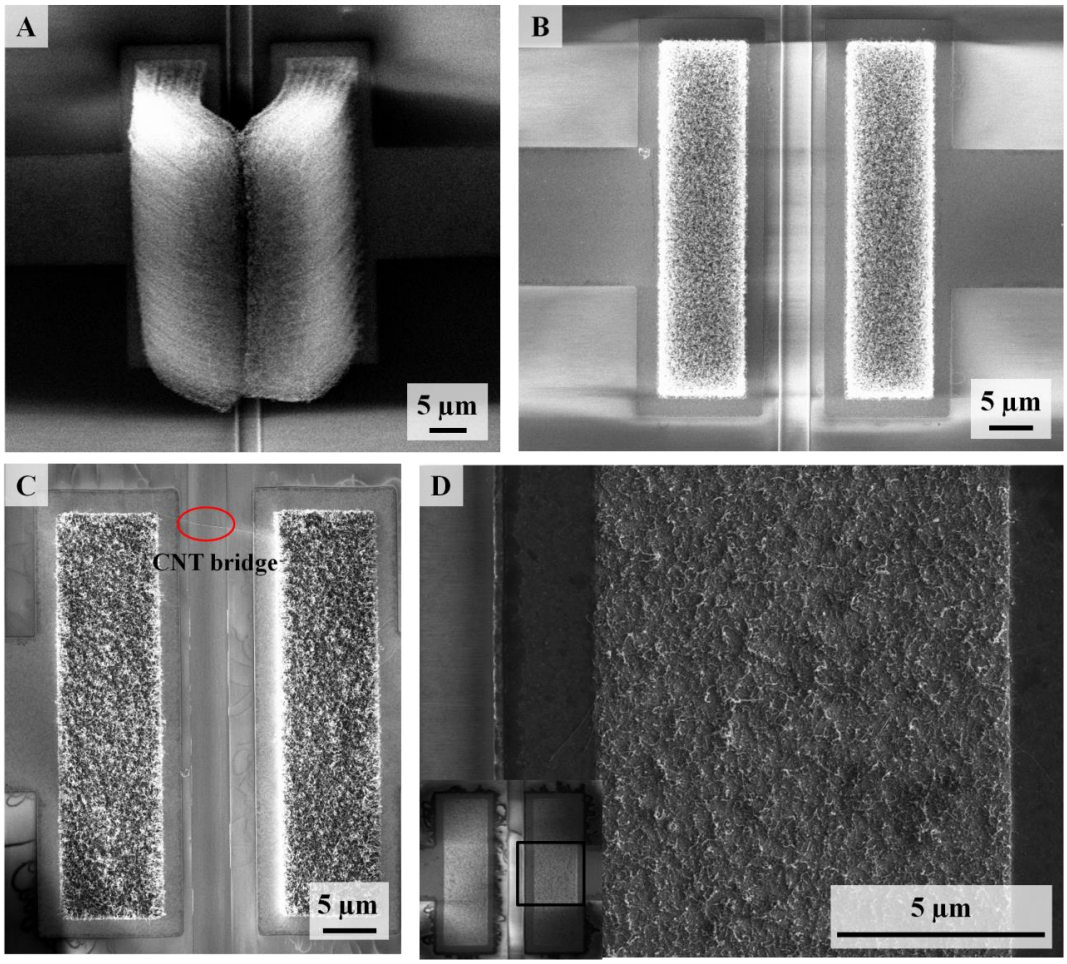

Figure 2.4 SEM images with samples under (A) 865 °C; (B) 915 °C; (C) 965 °C; (D) 1015 °C.

Our second strategy focuses on investigating the effect of growth temperature. It has been well-established that the growth temperature is a significant parameter of CNT synthesis, since it could affect both diameter distributions and growth duration time of CNTs during CVD process, and hence influence the final growth outcome.[56-59] In order to

explore the temperature dependency for CNT growth, we introduced acetylene along with methane for the entire growth procedure, which was able to produce high-density CNT forest growth at 865 °C (Figure 2.4 A), and then increased the growth temperature with an increasing interval of 50 °C up to 1015 °C (Figure 2.4 B,C,D). The results have shown that both the yield and length of CNTs have been compromised when the growth temperature goes up. Interestingly, as the length of CNTs shrank, the surface growth started to appear, along with the horizontal CNT-bridge structure that went across the trench (Figure 2.4 C). This indicates a transition from high-density forest growth to low-density surface growth. No forest growth was found when the temperature was ramped to 1015 °C. Instead, all the CNTs turned out to grow along the surface. Therefore, it is also possible to control the growth tendency and morphology of CNTs by adjusting the growth temperature only. In a reasonable growth temperature range, the lower temperature tends to produce high-density CNT forest while the higher temperature would result in low-density CNT surface growth.

2.3.4 Raman characterization and related analysis

Raman spectroscopy has been proven to be a powerful tool for revealing structural details and some optoelectronic properties of CNTs.[60-63] The radial breathing mode (RBM) could be used to tell the diameter of CNTs, while the disorder-induced D peak could help to determine the tube quality. In our Raman inspection, the spectra and images were obtained with 532 nm excitation under a 100X, 0.9 NA objective which provides a 1 μm spot size.

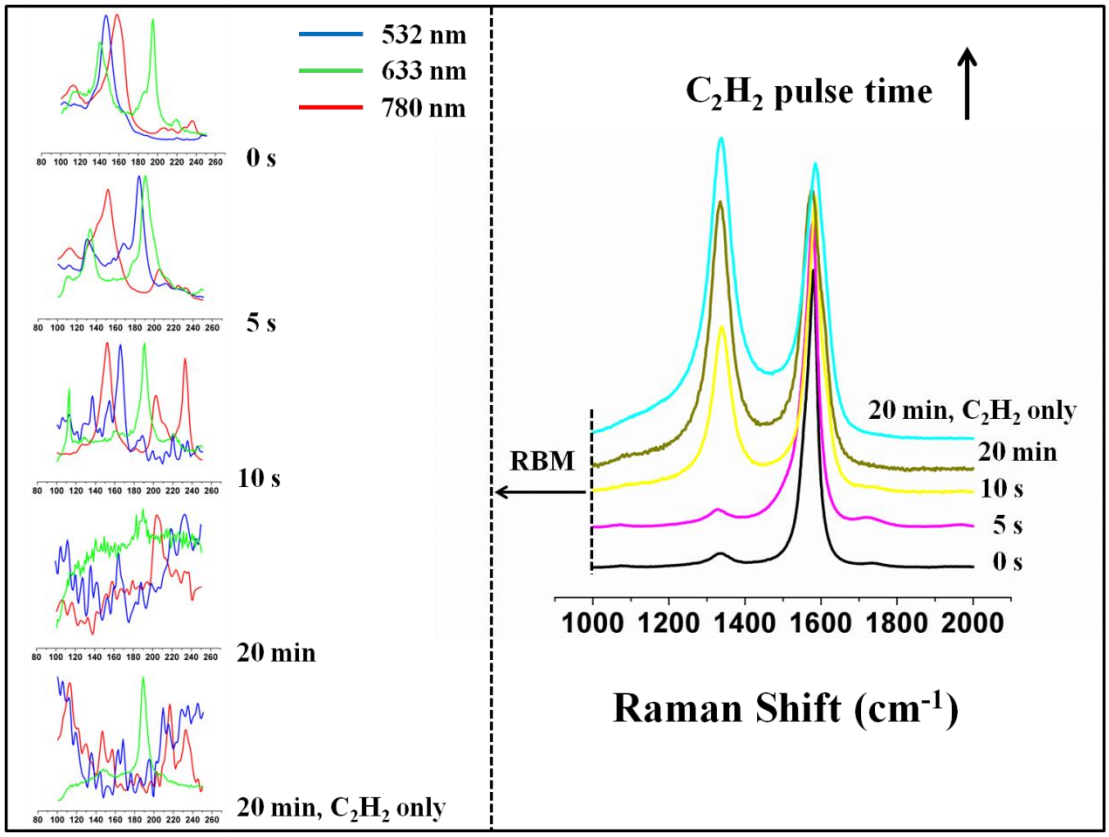

Figure 2.5 Raman spectral evolutions of as-grown CNTs prepared from different acetylene pulse time at 865 °C: CH_4 only for 20 min (Black); 5 s C_2H_2 pulse and constant CH_4 for 20 min (Red); 10 s C_2H_2 pulse and constant CH_4 for 20 min (Green); constant C_2H_2 and CH_4 for 20 min (Blue); and C_2H_2 only for 20 min (Cyan), respectively; The insets on the left of each figure are zoom-in RBM spectra.

As illustrated in Figure 2.5, the evolutions of Raman spectra for as-grown CNTs under different synthesis conditions have been observed. The rising of the D peak could be seen when the acetylene pulse time was increased (Figure 2.5 A). This suggests a significant increase of disorder in as-grown CNTs. When no acetylene was used and

methane was the only carbon feeding source, the D peak was almost invisible which indicated the growth of high quality nanotubes. The D peak intensity stayed unchanged when only 5 s of acetylene pulse was added at the beginning of the growth. However, when the pulse time of acetylene was increased to 10 s, a considerable increase of D peak could be noticed. The disorder became severe when acetylene was introduced for the entire 20 min growth procedure, where the G/D ratio nearly equaled to 1. Moreover, the D peak rose higher than the G peak when the CNTs were grown by acetylene only. The increase of the D peak may result from two causes, one is the increasing number of multi-walled CNTs, and the other is the contamination brought by amorphous carbon. As the acetylene pulse time increases, the resulting carbon flux to the catalyst may exceed the diffusion flux to nanotubes, which will lead to the formation of more disordered multiwalls. Besides, the excessive carbon may also deposit into amorphous carbon, introducing unnecessary contaminations into the system. Therefore, though acetylene appears to be useful to enhance the yield of CNT growth, it might compromise the tube quality.

We have also investigated the diamter distribution of as-grown CNTs via their RBM spectra. When no acetylene was added, the major absorption peak was between 160 and 190 cm^{-1} (Figure 2.5 A), indicating that the diameters were between 1.31 to 1.55 nm for the majority of CNTs. This feature stayed still when a very short pulse of acetylene (5 s) was introduced. However, the absorption peak became weaker and nearly invisible when 10 s and 20 min acetylene pulse were introduced respectively. We noticed that the major absorption peak reappeared but shifted to 97.5 cm^{-1} when acetylene was the only carbon feeding source used for the growth. The evolution of RBM spectra indicates that

the diameters of as-grown CNTs will increase if more dose (pulse time) of acetylene is introduced during the growth. Besides, because the tube deterioration has not shown up until the pulse time of acetylene is increased to 10 s, before which the major absorption peak of RBM spectra also stayed unchanged, we may consider the first 5 s of acetylene pulse time as a "clean boost". After that, there will be extra amount of acetylene which leads to substantially more disorder by bringing in either multi-walled CNTs or amorphous carbon contamination. Therefore, there may be a higher demand of acetylene for the nucleation stage than the subsequent growth stage. Keeping the acetylene pulse at a constant flowing rate for long would harm the tube quality. It is possible that taking a real-time control of the acetylene pulse, which starts with higher dose and ends with lower dose, will extend the time of "clean boost", promoting the yield of CNTs without compromising the tube quality.

By observing the Raman spectroscopic results for CNTs grown under different temperatures, where both acetylene and methane were used together as the carbon feeding source, we found a similar trend for the change of D peak. When the growth temperature decreased, the D peak substantially went up (Figure 2.6 B), suggesting the presence of multi-walled nanotubes or amorphous carbon contamination. Apparently, though high temperature could only produce CNTs with a low yield, it turned out to be effective in terms of producing high quality CNTs. This could be attributed to the better balance between the carbon flux to the catalyst and the diffusion flux to nanotubes under high temperature. The absorption peaks of RBM spectra showed a diameter distribution of 1.48 to 1.77 nm when the temperature was higher than 915 °C. However, the peaks became dispersed when the temperature dropped below that, indicating a wider diameter

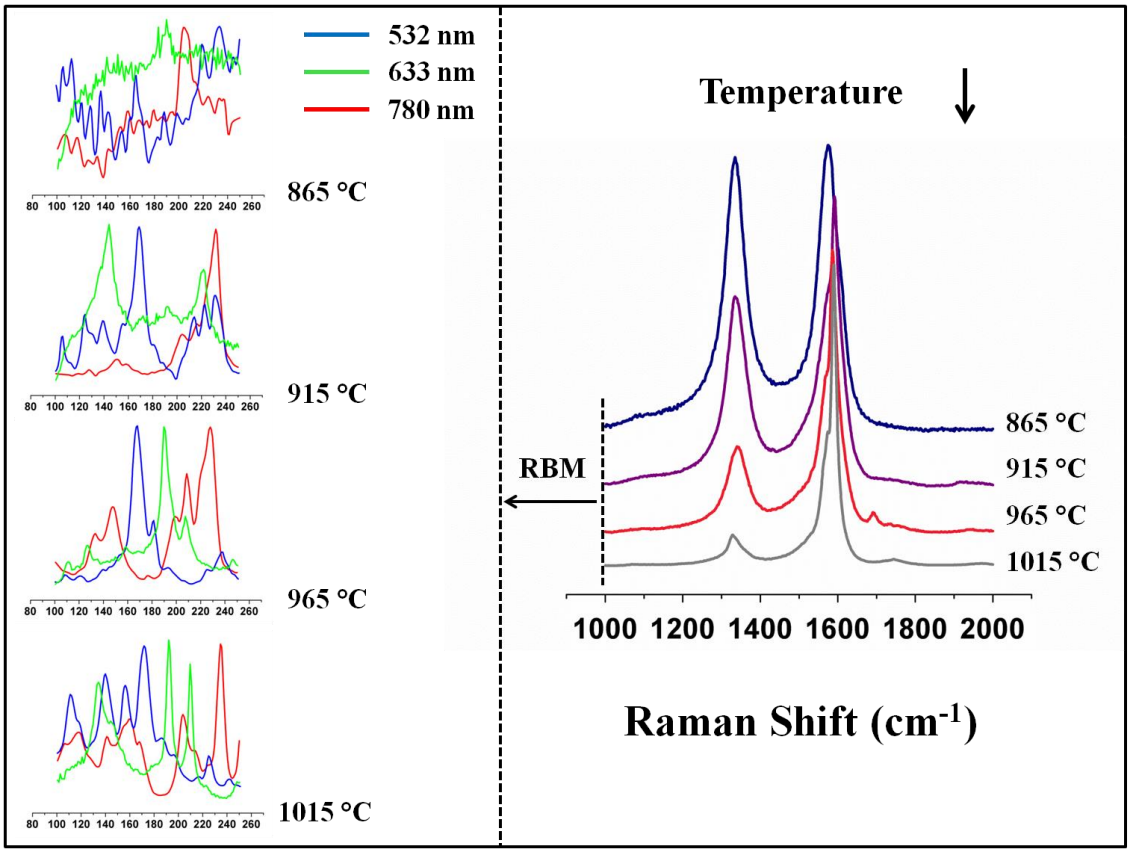

Figure 2.6 Raman spectral evolutions of as-grown CNTs prepared from different growth temperature under the same carbon feeding environment (constant C_2H_2 and CH_4 for 20 min): 865 °C (Navy); 915 °C (Purple); 965 °C (Pink); and 1015 °C (Grey), respectively. The insets on the left of each figure are zoom-in RBM spectra.

distribution. Similarly, a real-time growth temperature control, which starts with a relatively low temperature and ends with a high temperature, is possible to produce high quality CNTs with a great yield.

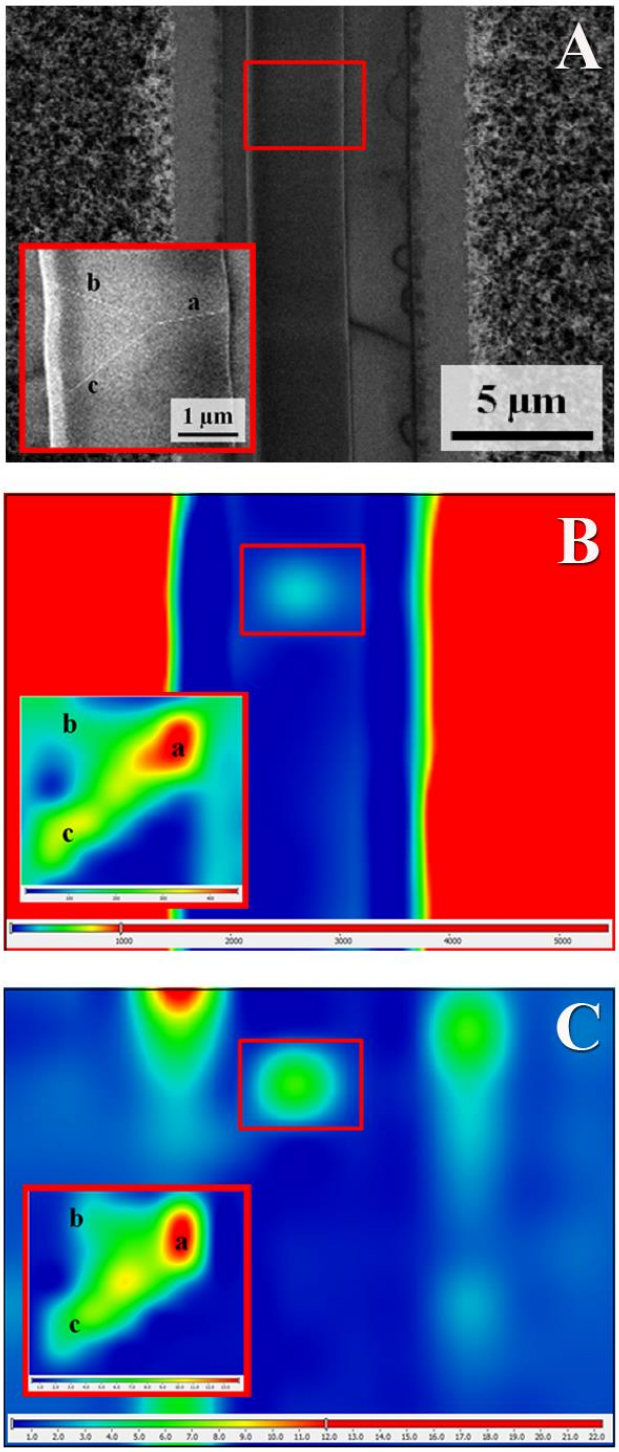

Figure 2.7 (A) SEM image of the sample treated with constant C_2H_2 and CH_4 for 20 min under 965 °C. Besides CNT forests, a suspended CNT-bridge structure has also been

observed (in red square), the insets enlarges the target areas; (B) G peak Raman mapping; and (C) G/D ratio Raman mapping. Different color scales have been used for the zoom-in pictures, as indicated at the bottom of each picture.

To monitor the quality change of CNTs, the Raman mapping has been performed for the sample prepared under 965 °C with both acetylene and methane as carbon feeding source. CNT forests as well as a suspended CNT-bridge, where a CNT rope splits into two CNT branches, have been obeserved (Figure 2.7 A). During the G peak mapping, a bright spot appeared in the middle of the trench, and the corresponding zoom-in picture showed a Y shape (Figure 2.7 B). This matches both the location and the structure of the CNT-bridge. Furthermore, through the G/D ratio mapping, we found that the G/D intensity gradually diminished from point a to point c, similarly from point a to point b (Figure 2.7 C), suggesting that the tube quality degrades as growing. This result agrees with our previous hypothesis that there might be different demands of carbon feeding gases and temperatures during different growth phases. At the initial stage, the current conditions were appropriate and high-quality CNTs were produced. When it went further into the growth stage, the demand for carbon feeding gases may be decreased and the ideal growth temperature may also be shifted. Consequently, for a typical growth procedure with constant parameters, there may be excessive resource that would bring disorder into the system either through the formation of multi-walled CNTs or the introduction of amorphus carbon.

2.4 Conclusion

In summary, we have managed to control the growth tendency and morphology of CNTs to produce CNTs from surface growth to forest growth either by adding the acetylene pulse at the beginning of the growth or adjusting the growth temperature while flowing acetylene and methane together. Though acetylene could activate more catalyst nanoparticles thus boost the yield, Raman spectrocopy shows an increasing D peak as the acetylene pulse is prolonged, which may arise from the contamination of amorphous carbon as well as the increasing amount of multi-walled CNTs. In addition, the increase of growth temperature also turns out to be effective to control the CNT morphology. Specifically, higher growth temperature tends to produce nanotubes with higher quality. Though further effort will be required to understand the potentially different demand between nucleation stage and growth stage in order to optimize CNT growth, the controllable CNT growth strategies in our study have already shown the efficiency to synthesize CNT forests, high yield suspended CNT-bridges, and combinations of both CNT-bridges and forests. The elaborate descriptions and analysis presented could provide insightful understanding for each strategy and help to further design efficient growth strategies with specific intentions.

CHAPTER 3

NANOSCALE CNT BIOMOLECULE SENSORS

3.1 Overview

Due to the ultra-high charge carrier mobility and large surface-to-volume ratio, CNTs have been considered to have great potential for biological and chemical sensing. As a matter of fact, the following intensive research proved that CNTs were versatile sensors for various sorts of molecules.[62-65]

The common technique is to coat CNT transistors with the solution of the target molecules and monitor the change of the gating curve. Figure 3.1 shows examples using CNT transistors for molecule sensing. We can find that CNT transistors are very sensitive to the electrostatic changes in the environment. The threshold gate voltage would shift once the molecule was introduced into the system. The sensing mechanism was mainly attributed to the charge transfer between CNTs and testing molecules. Besides, Star et al., also showed that this shift of the gate voltage could be reversed after the target molecule (starch) was removed (Figure 1.2 C), which indicated that CNT sensors had excellent electrochemical stability. The interactions between CNTs and biomolecules have been studied since 2006[64], when DNA was dried on top of a CNT transistor after spin-coating to observe the changes of conductance and gating voltage. The following work performed by Sorgenfrei *et al*., used a point defect in a CNT to probe DNA sequence[65]. Two-level

fluctuations in the conductance of the CNT were successfully measured in presence of a complementary DNA target. However, neither of the studies could guarantee high precision manipulation at a single-molecule level, which is important for the understanding of the fundamental process between CNTs and DNA.

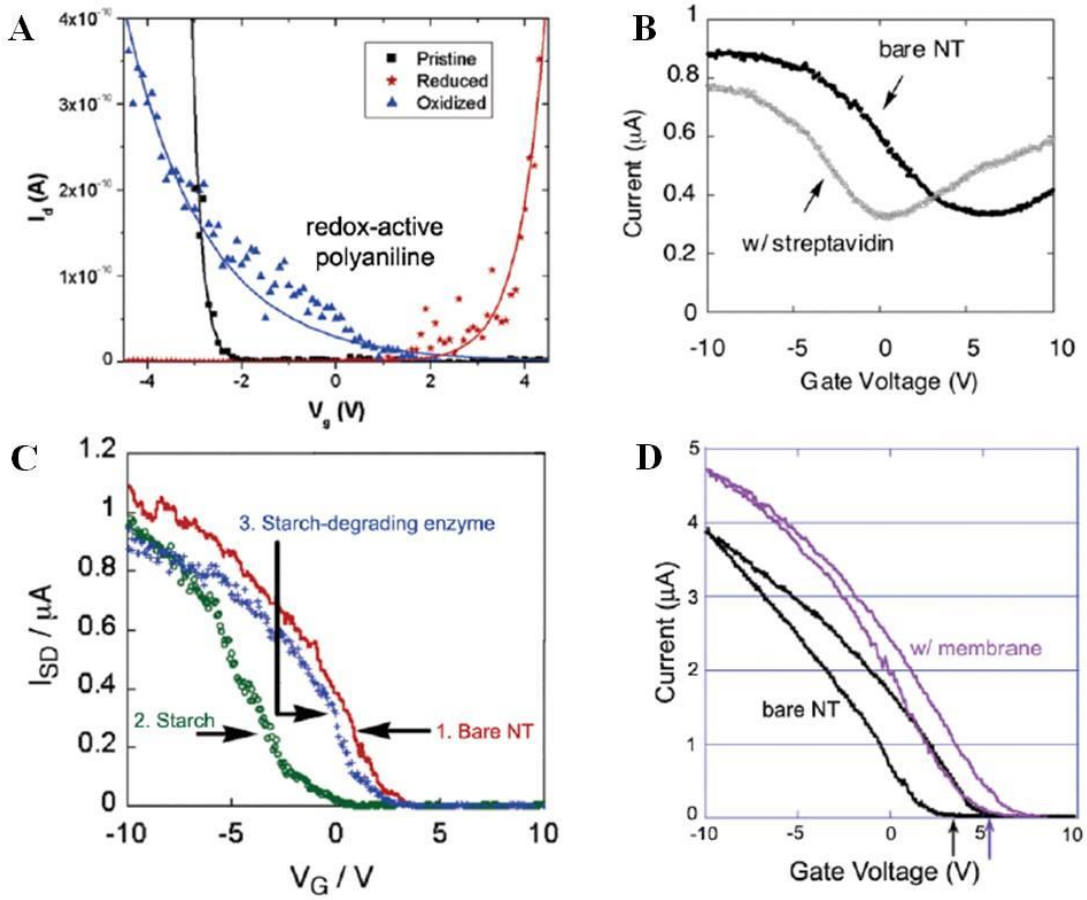

Figure 3.1 CNT transistors used for molecule sensing. The response from CNT sensors is shown for (A) redox-active polyaniline[66], (B) streptavidin[67], (C) starch and a starch-degrading enzyme[68], (D) a cell membrane[69].

In this chapter, suspended CNT transistors have been fabricated to explore the local electrostatic changes in a liquid environment. Scanning photocurrent has been utilized to image and locate the position of suspended CNTs in solution, and the optoelectronic behaviors of the CNT transistors have been systematically studied. The CNT's relation with the electrostatic potential in solution has shown its great capability for biomolecule sensing. Taking advantage of the local photocurrent response, CNT sensors are estimated to reach single-electron-charge sensitivity.

3.2 Materials and methods

3.2.1 Device fabrication

As shown in Figure 3.2, the device was pre-patterned by photolithography. In order to make suspended CNT transistors, a trench (5 μm wide and 5 μm deep) was etched into a 170 μm thick fused silica double side polished substrate by the Oxford Plasmalab 80+ RIE system. E-beam evaporation was utilized to deposit the source and drain electrodes (2 nm Ti, 40 nm Pt), which were separated by 7 μm. Similar process was used to deposit the catalyst pads (10 nm of Al_2O_3, 0.2 nm of Fe) on the top of metal electrodes. After the photolithography patterning, suspended CNTs can be directly grown to bridge between source and drain electrodes by CVD process. The pulse controlled strategy described in Chapter 2 is an efficient method to growth suspended CNT bridges. The recipe of suspended bridges listed in Appendix A is also an alternative.

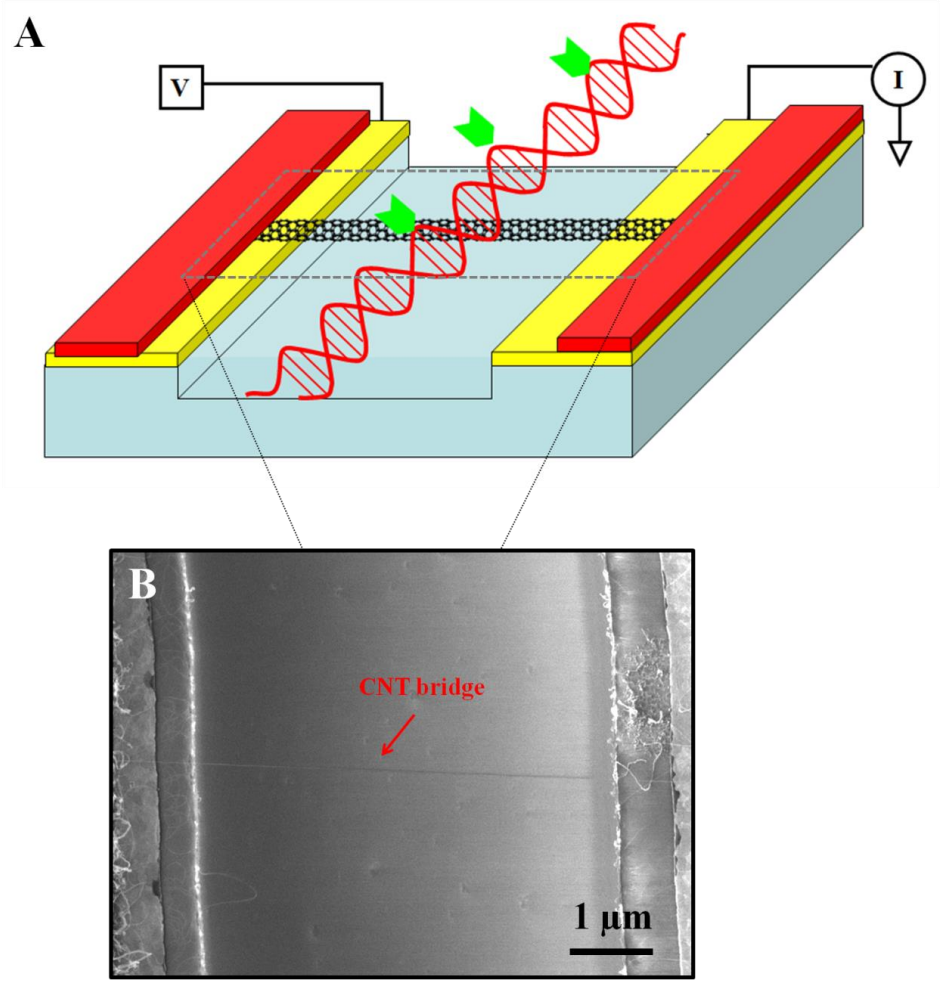

Figure 3.2 CNT transistors as biomolecule sensors (A) the schematic diagram of CNT biosensors; (B) Top-view for the CNT sensor by SEM.

3.3.2 Scanning Photocurrent measurements

A spatially scanned CW laser was used to measure the devices through a microscopic system. A collimated laser beam (λ = 785 nm) was expanded and focused to a diffraction-limited laser spot (< 500 nm) by a 60x IR enhanced water immersion

Olympus objective (NA = 1.2). Incident laser power was changed by a continuous neutral density filter. The laser beam was scanned over CNT transistors by a two-axis scanning mirror with nanometer spatial resolution. The responding current signal was collected by a preamplifier.

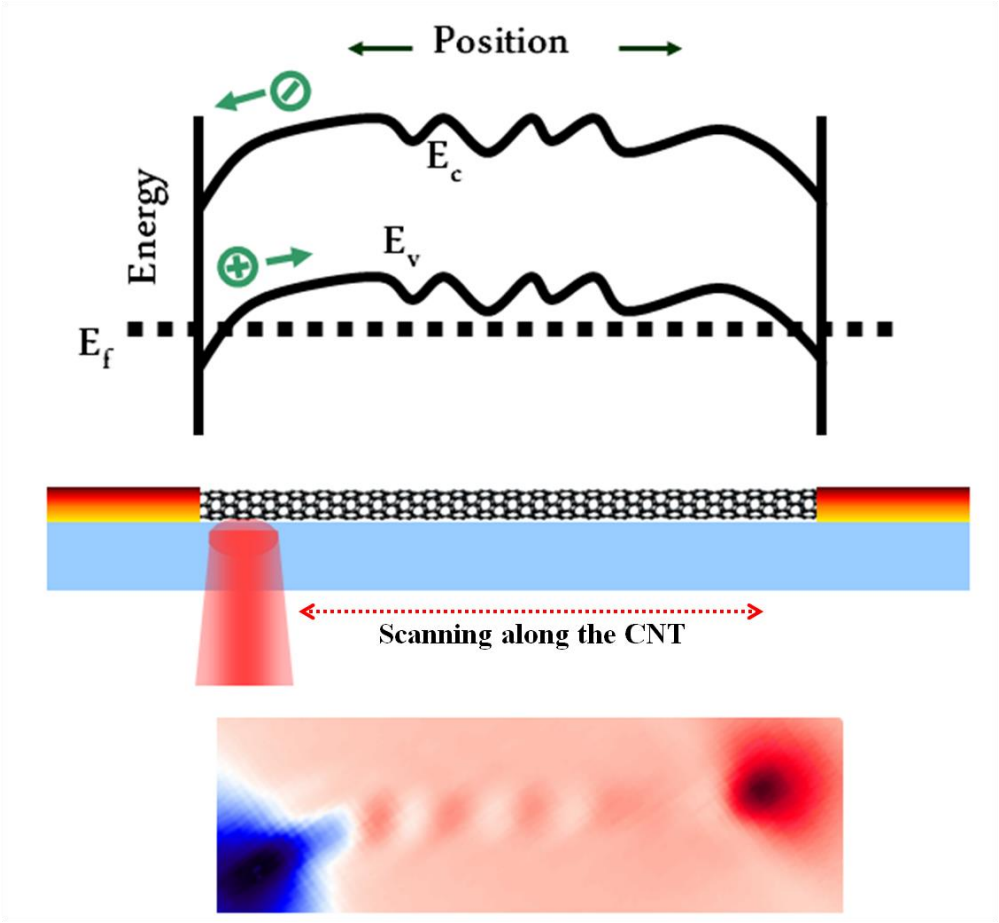

Figure 3.3 Mechanism of photocurrent imaging. The band diagram on top shows the band curvatures for the CNT transistor lying in the middle. When a laser shines on the CNT transistor, its photocurrent response can be detected by our optical setup, showing a series of dots.

Figure 3.3 illustrates the schematics of the mechanism of photocurrent generation. A CVD-grown single-walled CNT transistor usually comes along with defects, which will lead to the bending of the band structure for the single-walled CNT transistor. As a result of the carrier diffusion to reach the equilibrium of Fermi levels, built-in electric fields are formed at the band curvatures. When the single-walled CNT transistor is illuminated with laser, the electron-hole pairs will be generated and accelerated by the built-in electric fields to form the photocurrent, which can be detected and observed by our photocurrent measurement setup.

3.3 Results and discussion

3.3.1 Photocurrent of CNT sensors

In order to obtain the instant information of a CNT sensor during the biomolecule sensing in solution, a proper imaging tool is necessary. Common optical microscopes do not have the resolution to observe CNTs. Although SEM is powerful enough to reveal the details of CNT sensors, the high energy electron beam used during the imaging will also produce carbonaceous contaminations and defects on CNT bridges, resulting in the degradation of the sensor property. We thus developed an alternative method, the scanning photocurrent measurement, to achieve the instant imaging of CNT sensors. As shown in Figure 3.4 A, when the diffraction-limited laser spot was scanning over a suspended semiconducting CNT, the generated photocurrent could be detected by the preamplifier, and mapped in the scanning area.

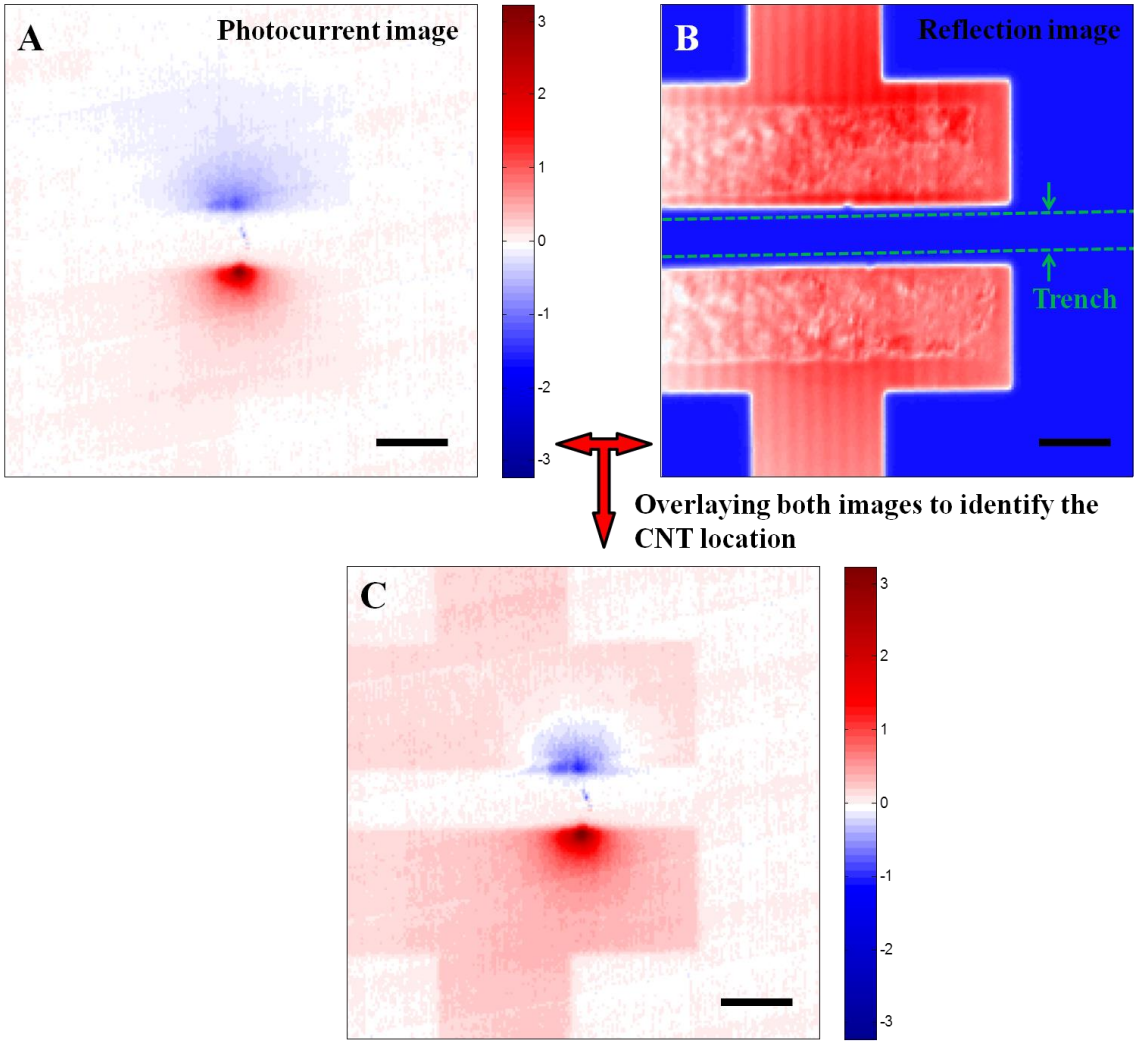

Figure 3.4 Photocurrent imaging of CNT transistors. (A) The photocurrent response is shown for a suspended CNT transistor. A 785 nm laser is used with a power of 200 µW. The color bar represents a range of nA. Strong signals were observed at the metal contacts. (B) The reflection image of the same device collected simultaneously with the photocurrent image in false color. The distance between the electrodes is 8 µm, between which lies a 5 µm trench, as specified by the green dotted lines. (C) By overlaying with

the reflection image, we are able to find the exact location of the CNT transistor and measure its position relative to the edges of the electrode pads. All scale bars are 10 μm.

The strong signals on the edges of the electrodes could be ascribed to the formation of the Schottky barriers between Pt and the CNT transistor. Due to the curvatures in the energy bands along the suspended CNT, the photo-excited carriers in different local spots would tend to flow in different directions, which led to a series of spots with different colors, revealing the physical shape of the CNT sensor. In the meantime, the reflected light was being collected by the Si photodetector. Since most of the reflected light came from the more reflective metal electrodes, the reflection image could be utilized to locate the position of the electrodes (Figure 3.4 B). Therefore, by overlaying the reflection image with the photocurrent image, we were able to identify the location of the CNT sensor relative to the contact edges (Figure 3.4 C).

Figure 3.5 shows two examples of devices with more than one CNT. An ideal device for biomolecule sensing would be the one with single CNT in order to observe the biological interaction at single molecule level without interference. Besides, the manipulation of biomolecules requires certain operating space. The presence of nearby CNTs will limit the degree of freedom for the biomolecule molecules when moving along the trench, which substantially increases the difficulty of the manipulation. Another reason could be ascribed to the variances of the gating curve between different CNTs. It will be difficult to tune the sensor through the electrolyte gate if CNTs with different threshold gating voltages are found on the same device.

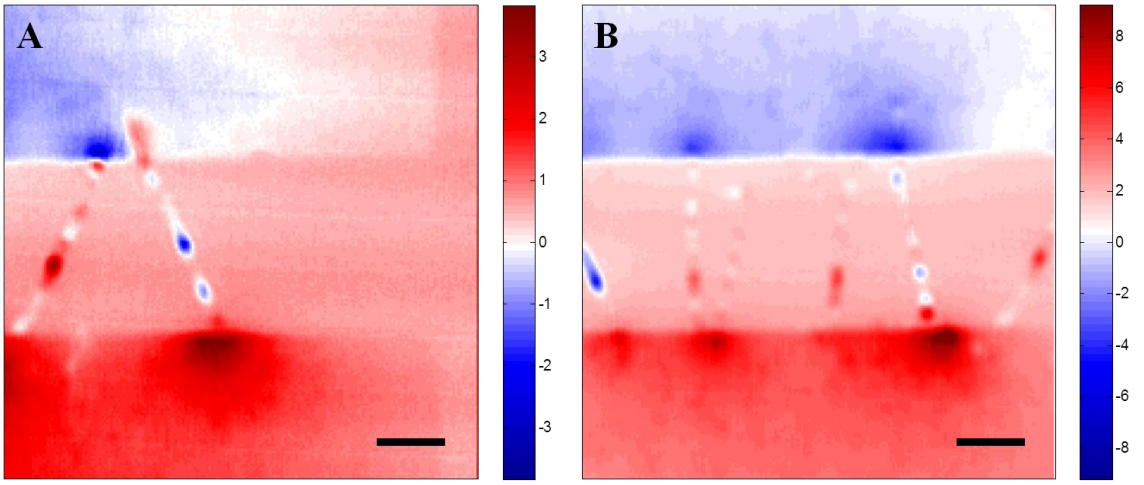

Figure 3.5 Photocurrent imaging of devices with (A) two CNTs and (B) multiple CNTs. The photocurrent intensities are in nA range. The scale bars for both images are 3 μm.

3.3.2 Electrolyte gating measurements

Gating measurement is an important method to characterize the CNT transistor and directly determine whether the CNT transistor is semiconducting. Semiconducting CNTs are more suitable for molecular sensing due to their high sensitivity to ambient changes. It is important to use semiconducting CNTs in biomolecule sensing since their optoelectronic properties could be changed by tuning the gate. Although the number of the spots from the photocurrent response could be used to infer whether or not the CNT is semiconducting, no conclusion would be drawn without gating measurement, where the conductivity of semiconducting CNTs will change while the gating voltage varies.

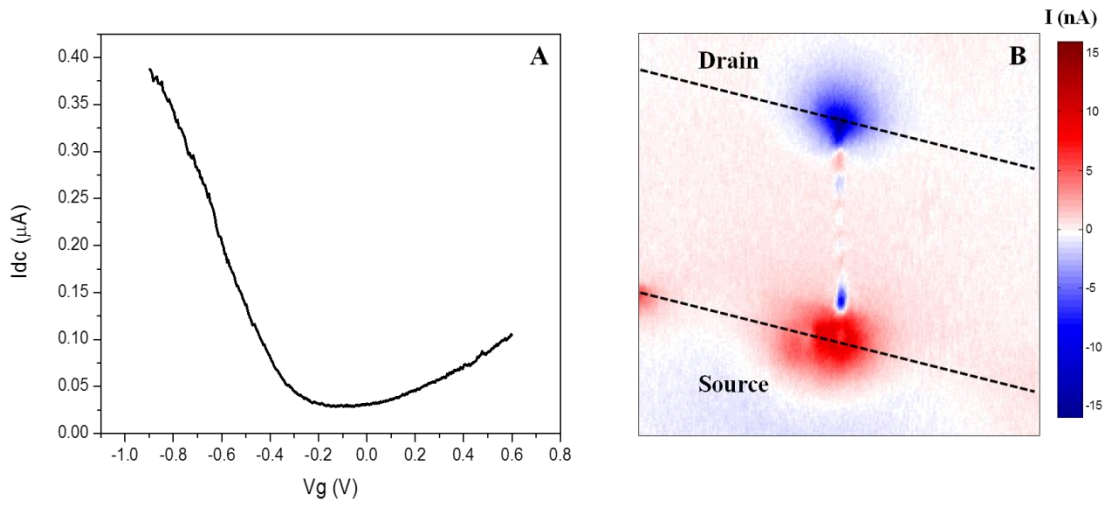

Figure 3.6 (A) the gating curve for a semiconducting CNT transistor, where $V_T \approx -0.2V$; (B) the corresponding photocurrent image. A 785 nm laser is used with a power of 200 μW. The dotted lines show the edges of the electrode.

Since the most biomolecules demand to be in aqueous environment, where the back gate is strongly screened by the solution and becomes ineffective, we have adopted the electrolyte gate to perform the gate characterization.[70] Shown in Figure 3.6 are the gating curve and the corresponding photocurrent image for a semiconducting CNT transistor. Due to the long channel length and the presence of defects, the on/off ratio for our CNT sensors is below 10^4. In the corresponding photocurrent image, multiple spots can be observed due to the curvatures in the band structure of the CNT transistor. We also found that the photocurrent response from semiconducting CNTs could be changed when an external voltage was applied through the electrolyte gate. When we introduced a gating voltage to the semiconducting CNT device in Figure 3.6, it exhibited distinct photocurrent behaviors.

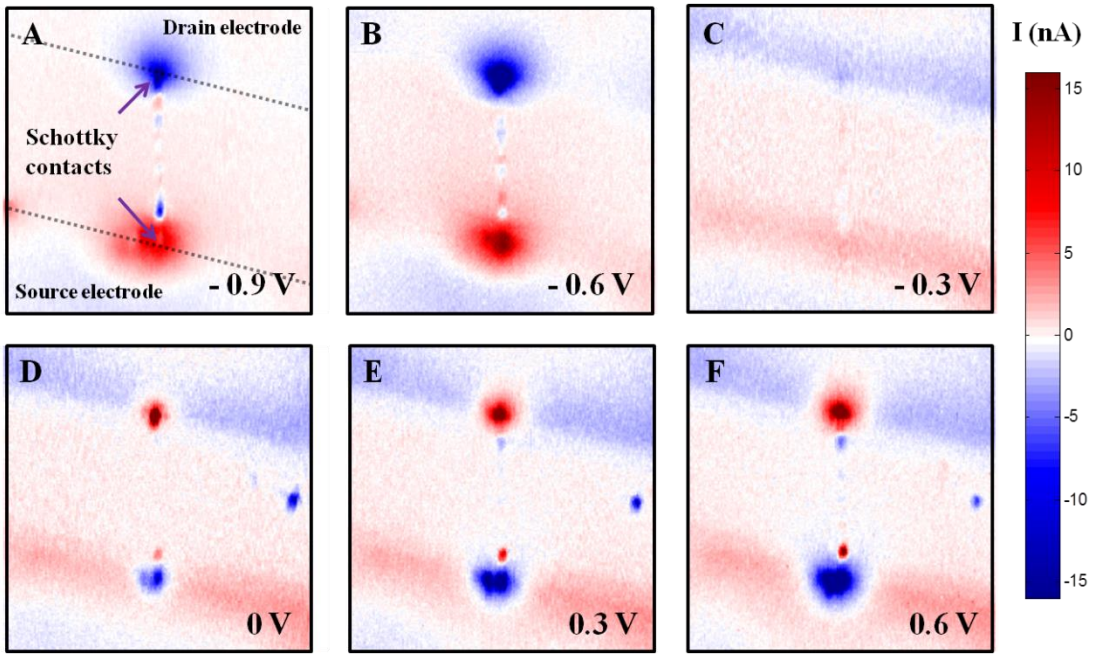

Figure 3.7 Photocurrent images of the semiconducting CNT sensor at (A) Vg = -0.9 V; (B) Vg= -0.6 V; (C) Vg= -0.3V; (D) Vg= 0V; (E) Vg= 0.3V; (F) Vg= 0.6V. The contacts between the nanotube and the metal electrodes are specified with purple arrows.

As illustrated in Figure 3.7, prominent photocurrent response was observed at Vg = -0.9 V (similarly at Vg = 0.6 V). However, when $|Vg - V_T|$ decreased, the corresponding photocurrent response became weaker and the CNT sensor was barely seen (Figures 3.7 B, C, D, E). We found that the strength of the photocurrent at the Schottky contacts was enhanced monotonically when the bias between gate voltage and threshold voltage ($Vg \approx 0.2$ V) was increasing. Furthermore, the photocurrent switched signs when the gating voltage was tuning the CNT from p-type to n-type regime, indicating a significant influence from the photovoltaic effect.

3.3.3 Estimate of the electrical sensitivity of CNT optoelectronic sensors

As previously shown in Figure 3.7, the photocurrent is measured as a function of position, typically producing a series of spots along a CNT, wherever disorder, contacts, or substrate interactions produce strong carrier separation. The center of the spots corresponds to the location of the CNT, which can be measured with precision much greater than the diffraction limit. The root-mean-square of the spatial fluctuation is about 10 nm,[71] which theoretically allows us to use a 10-nm-long segment of the CNT as a local optoelectronic nanosensor. Compared with the entire length of the CNT (~ 10 μm), the charge sensitivity can be enhanced by 1000 times. Considering that in our biological sensing system with an electrolyte gate, the electrical double layer will be formed by the ions and counterions in the aqueous solution. The capacitance across the double layer in the PBS solution at room temperature is given by

$$C[F/m^2] = 2.3\sqrt{C_0[M]}\cosh(19.5\emptyset_0[V]) \tag{4}$$

where C_0 is the concentration of PBS solution, Φ_0 is the infinite charged plane of potential used in the double layer model.[72] By applying the model adjustment proposed by Bockris et al.,[73] we are able to yield an approximate value of 0.1 F/m^2. Thus, for a typical CNT with the diameter of 1 nm, the capacitance C_{seg} is equal to

$$C_{seg} = \pi \cdot d\ [nm] \cdot C[F/m^2] \approx 0.3\ fF/\mu m \tag{5}$$

When a biomolecule gets in close proximity with a CNT sensor, it may act as a local gate on the semiconducting CNT. One electron charge in the biomolecule can shift the electrostatic potential of the 10-nm-long CNT segment by ~53 mV, which

corresponds to the photocurrent change of ~800 pA according to the gate-dependent photocurrent behavior in Figure 3.8. This current change is at least one order of magnitude larger than the electric measurement noise level of our newly-developed optoelectronic probing system.

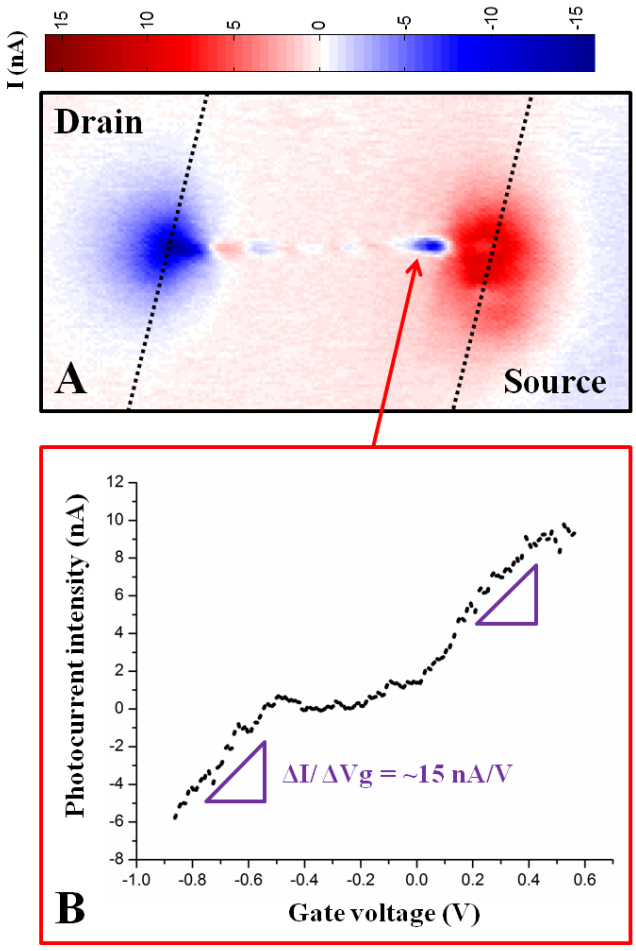

Figure 3.8 Gate-dependent photocurrent behavior for a local spot. (A) The photocurrent image for the CNT sensor. The dotted lines specify the edges of the trench. (B) Photocurrent response from the local spot (as pointed by the red arrow) while Vg sweeps from -0.9 V to 0.6 V.

3.4 Conclusion

In summary, we have fabricated suspended semiconducting CNT transistors and investigated their optoelectronic properties in an aqueous system. Through the scanning photocurrent measurement, CNT transistors have exhibited high sensitivities with the local electrostatic changes, showing great potential as biomolecule sensors. A theoretical calculation indicates that CNT optoelectronic sensors are estimated to reach single-electron-charge sensitivity.

CHAPTER 4

ENGINEERING THE STRUCTURES OF GRAPHENE RIBBONS

In Chapter 2, we systematically investigated the methods to control the growth morphology of CNTs, which could be produced in forms of surface growth, or vertically-aligned growth. Here we present the method to engineer the structures of graphene, another promising carbon nanomaterials, and explore its potentials in optoelectronic applications. Since the first report of CVD synthesis of graphene, the mechanisms of graphene growth have been intensively studied. Unlike CNTs, graphene will only be grown in the form of atomic films with one or few layers thick. However, we found that the single layer graphene ribbons could be engineered during the annealing process, where the evaporation of poly methyl methacrylate (PMMA) would curl the graphene ribbons, and thus lead to the formation of unique graphene structures. Compared to regular graphene ribbons, this new structure present high efficiency in terms of photon-induced photoresponse.

4.1 Overview

Graphene, a two dimensional material composed of a single atomic layer of carbon, has attracted significant attention due to its superb electrical, optical and mechanical properties.[1, 32, 74-76] However, the fact that graphene is inherently a zero band-

gap semi-metal has limited its implementation in potential electronic applications. A large number of theoretical and experimental studies have suggested that by modifying the morphology of graphene, it is possible to enhance certain physical properties of graphene and thus make it a more appealing building block for future electronics and photonics.[77-83] An intensive research effort has been dedicated to modify graphene morphology, leading to the rise of two feasible methods. The first method is to confine the lateral dimension of graphene ribbons in nanometers.[77-79] This method, however, is bottlenecked by the complexity of the high-precision fabrication and limited control of edge chirality. The second method usually employs three-dimensional deformations in graphene, which is less complicated and normally easy to control.[80-83] Many novel structures have been derived from this method, such as collapsed graphene wrinkles[80], folded graphene membranes[81], and crumpled graphene[82], all of which exhibit intriguing but distinct properties compared with pristine graphene.

In this chapter, we develop a facile method to alter the graphene morphology and further change its optoelectronic behaviors. By utilizing the distortion generated from the thermal degradation of poly-methyl methacrylate (PMMA), we are able to make curled graphene ribbons (CGRs) which exhibit remarkable optoelectronic response through the spatially resolved scanning photocurrent microscopy. By controlling the annealing temperature, thickness of the graphene and type of PMMA, we are able to systematically change graphene structures from free-standing ribbons to CGRs.

4.2 Materials and methods

4.2.1 Synthesis of graphene

Following the recipe of Li et al.,[34] we used Alfa Aesar 0.025 mm, 99.8% pure copper foils for the graphene growth. The copper foils with the grain size of ~100 μm were cut into stripes of ~1 cm in width. To prepare the foils for the growth of high quality graphene, acetone (10 seconds), IPA (10 seconds), and DI water were used successively to clean the copper foils to eliminate the contamination. Then silicon flatteners were used to flatten the foils. During the entire growth and subsequent transfer process, the copper foils have to be kept as flat as possible, since the wrinkles may result in cracks in graphene.

For the growth, we loaded copper foils onto a quartz boat, which was hence transferred to a horizontal furnace system. After the system was pumped down to 10 millitorr, we increased the temperature to 1000 °C and started to flow 100 sccm Ar along with 10 sccm hydrogen to anneal for 1 hour. Once the annealing was done, Ar was terminated and a mixed gas of H_2/CH_4 (5~20 sccm /100 sccm) was introduced into the furnace and stayed for 30 min. The growth of graphene was conducted at 1000 ℃ ~ 1050 ℃. After the growth, the sample was taken out of the furnace for fast-cooling.

4.2.2 Three-step wet solvent baths

The samples annealed under low temperatures (< 350 ℃) usually end up with PMMA residue, which may potentially compromise the properties of graphene. Those

residues could be well removed by overnight soaking in chloroform, which has high dissolvability for PMMA. Since the suspended graphene structures are very fragile and hardly survive from the direct drying of chloroform. Thus we use an additional two steps of wet solvent baths to preserve the structures. After the chloroform cleaning, samples have to go through a 10 min ethanol bath followed by another 10 min bath in hexamethyldisilazane (HMDS), which can be quickly dried in air and produce little surface tension during the process.

4.3 Results and discussion

4.3.1 Forming the curled structure through thermal annealing

Figure 4.1 shows the schematics of the device. The Pt electrodes were patterned on fused silica/oxidized silicon wafers by photolithography and deposited by e-beam evaporation. The source and drain electrode pads were separated by 8 μm, between which a 4-μm-deep trench was etched by RIE. Graphene was synthesized through chemical vapor deposition (CVD) on cleaned copper foils (25 μm thick) with reaction gas mixtures of CH_4/H_2=20/100 sccm at 1000 ℃. After graphene growth, an ultra-thin PMMA layer was spin-coated on top of the graphene/copper-foil stack. Then the PMMA/graphene film was transferred to the desired substrate after the underlying copper was removed by a wet etching process.

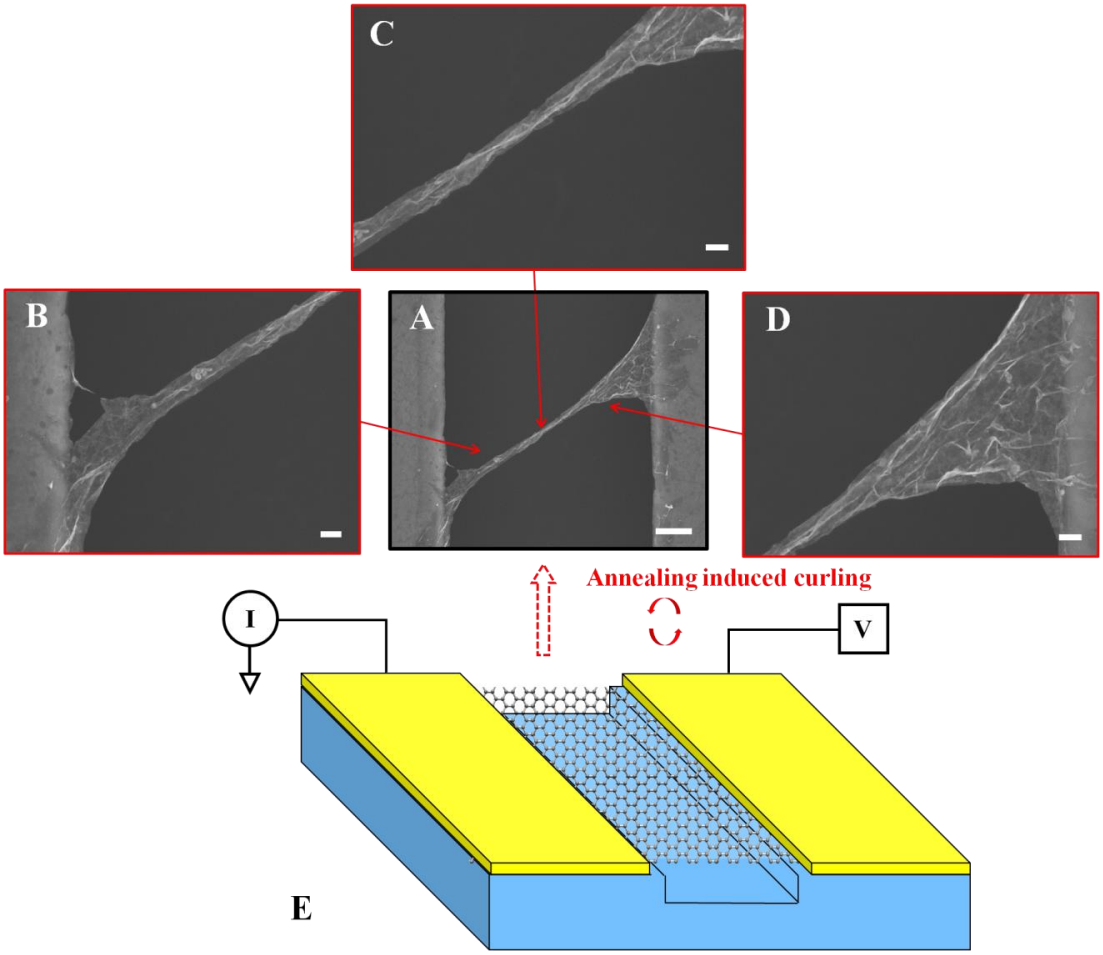

Figure 4.1 Schematic view of a typical CGR device. (A) The SEM image of a typical CGR structure. The scale bar is 1 μm. The beam accelerating voltage was set below 5 kV to prevent potential damage to the CGRs. (B), (C), and (D) represent the zoomed-in images of the different sections of the structure, as specified by the red arrows. All the scale bars in those zoomed-in figures are 200 nm. (E) The device geometry for a pre-annealed sample. 40 nm Pt was used as for source and drain electrodes. Graphene was transferred to cover the overall trench area with a length of ~ 8 mm on a die, which consisted of 30 device patterns.

Thermal annealing process was then used to remove the PMMA and to form CGRs. The sample was vacuum annealed (base pressure < 1 mTorr) at 440 °C for 30 min in the presence of 200 sccm Ar and 20 sccm H_2, allowing for complete evaporation of the PMMA[84, 85]. No further lithographic patterning was performed, and the separation of each device was achieved by physical scratching after the formation of CGRs. As illustrated in Figure 4.1 (A), after this annealing process, the suspended graphene membrane tended to form a curled structure. Wrinkles were also found in the edge regions of the suspended graphene ribbon [Figures 4.1 (B), (C), (D)], which may result from the difference between the thermal expansion coefficients of graphene and the PMMA.[86] The suspended region of the graphene membrane was susceptible to the distortion induced by the evaporation of the PMMA and was becoming curled and wrapped, while the supported graphene membrane stuck well to the substrate due to the ultrastrong adhesion between graphene and SiO_2[87], resulting in the observed morphology variance of the graphene. This unique graphene structure has been found to substantially enhance the photoresponse of graphene, showing a great potential for optoelectronic applications. In order to produce these structures in a controllable way and to understand the formation of CGRs in an experimental point of view, the roles of the different related parameters have been investigated thoroughly.

4.3.2 Influence of annealing temperature

Realizing that the annealing temperature could directly affect the thermal degradation of PMMA, we investigated the influence of temperature on the formation of CGRs. Besides the optimal annealing temperature of 440 ℃, two lower temperatures of

340 ℃ and 240 ℃ were also tested. We found that the annealing temperature was the key parameter that influences the morphology variance for CGRs. Other annealing parameters such as annealing time and heating rate did not result in significant changes. As shown in Figure 4.2 (A), when other annealing conditions were held constant during the process, we formed distinct graphene structures at each temperature. At 240 ℃, all graphene structures formed were flat free-standing ribbons. PMMA was found to degrade inefficiently at this temperature,[84, 85, 88] indicating that there may not be enough distortions during the annealing to initiate the curling of graphene. But once the annealing temperature was increased to 340 ℃, the percentage of free-standing ribbons diminished significantly while the CGRs predominated. When the annealing temperature was further increased to 440 ℃, CGRs were the dominant graphene structures while flat ribbons were hardly found.

In order to compare the photoresponse of graphene structures with differing morphologies, we performed spatially resolved scanning photocurrent measurements. For samples annealed under low temperatures (< 350 ℃), chloroform was used to remove potential PMMA residues and the graphene structures were preserved by utilizing critical point drying. As shown in Figures 4.2 (B) and (C), the photocurrent response from a graphene ribbon was usually weak, with intensity less than 1 nA in the present experimental setup. The generation of the photocurrent mostly came from the interface between the graphene and metal electrodes, which may result from potential barriers at the contacts induced by the Fermi-level alignment.[89, 90] Weak photocurrent was also observed at the edge of the trench, indicating the presence of a potential-step at the suspension interface. When the temperature was increased to 340 ℃, the curling of the

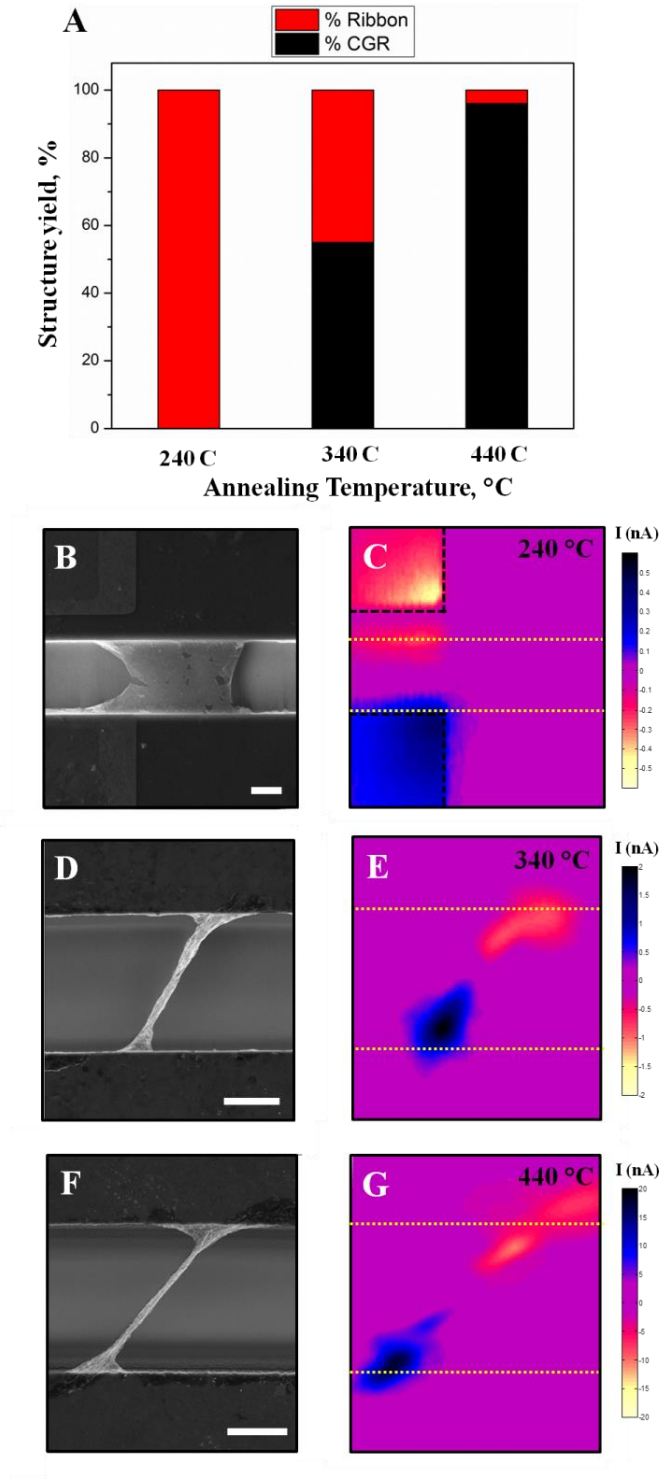

Figure 4.2 SEM and photocurrent images of CGRs at different annealing temperatures. (A) The percentage of graphene structures at different annealing temperatures. The

statistical results were obtained from a pool of over 50 graphene structures for each temperature. (B) A graphene ribbon annealed at 240 ℃. (C) The corresponding photocurrent image for the graphene ribbon annealed at 240 ℃. A diffraction-limited laser spot (< 500 nm) transmits from the transparent substrate to scan over the suspended graphene structures. The laser power was 1.2 mW for all photocurrent images. The electrode areas are specified by black dotted lines. The trench is marked by yellow dotted lines. (D) A typical CGR structure annealed at 340 ℃. (E) The corresponding photocurrent image for the CGR annealed at 340 ℃. (F) A typical CGR structure at 440 ℃. (G) The corresponding photocurrent image for the CGR annealed at 440 ℃. All the scale bars are 2 μm.

---

graphene membrane started to appear [Figure 4.2 (C)]. Unlike graphene ribbons, whose photocurrent can only be found for the ribbons between electrodes, strong photocurrent response was observed in CGRs even without metal contacts. As shown in Figure 4.2 (E), the suspended CGR structure exhibited a pronounced photocurrent with intensity in nA, which was substantially stronger than that detected in the graphene ribbon. The enhancement of photocurrent might be attributed to the interlayer interactions among tightly stacked graphene layers in the CGR, which may enhance the electron-electron interaction and further influence the intrinsic optoelectronic properties of graphene. Once we increased the annealing temperature to 440 ℃, CGRs were found to become even narrower, possible due to the higher degradation rate and more sufficient evaporation of PMMA at this temperature.[84, 85, 88] The photoresponse from CGRs was further enhanced, showing prominent photocurrent in the range of tens of nA [Figure 4.2 (G)].

4.3.3 Influence of graphene thickness

Besides the annealing temperature, the graphene thickness was found to be another important factor that influences the formation of CGRs. As discussed before, when the annealing temperature was increased to 440 ℃, most structures we obtained were CGRs. However, a few structures (< 5%) still turned out to be flat freestanding ribbons after the annealing process.

Figure 4.3 shows a typical graphene ribbon obtained after thermal annealing at 440 ℃. We found that the graphene ribbon was a part of a darker stripe easily distinguished from other regions on the substrate [Figure 4.3 (A)]. Raman spectroscopy was performed to characterize the device, since it is a non-destructive and effective tool to fingerprint for single and multi- layer graphene. As illustrated in the G mapping in Figure 4.3 (B), the Raman intensity of G band was substantially higher in the stripe than in the other substrate regions. This was indicative of thicker graphene layers in the stripe area, since the G-band intensity would increase with the number of layers in graphene.[91, 92] Individual spots were also taken on different regions of the device. As shown in Figure 4.3 (C), two prominent peaks could be observed in the corresponding Raman spectra, where the G peaks were normalized to show better comparisons with 2D peaks. In contrast to other surface regions, where I(2D)/I(G) ratio was ~ 2, the I(2D)/I(G) ratio significantly decreased to ~ 0.5 at the freestanding graphene ribbon as well as the other regions of the stripe, indicating the presence of multi-layer graphene which agreed with the observation from G-band mapping. These results suggested that the presence of multi-layer graphene might prevent the graphene membrane from curling into a CGR.

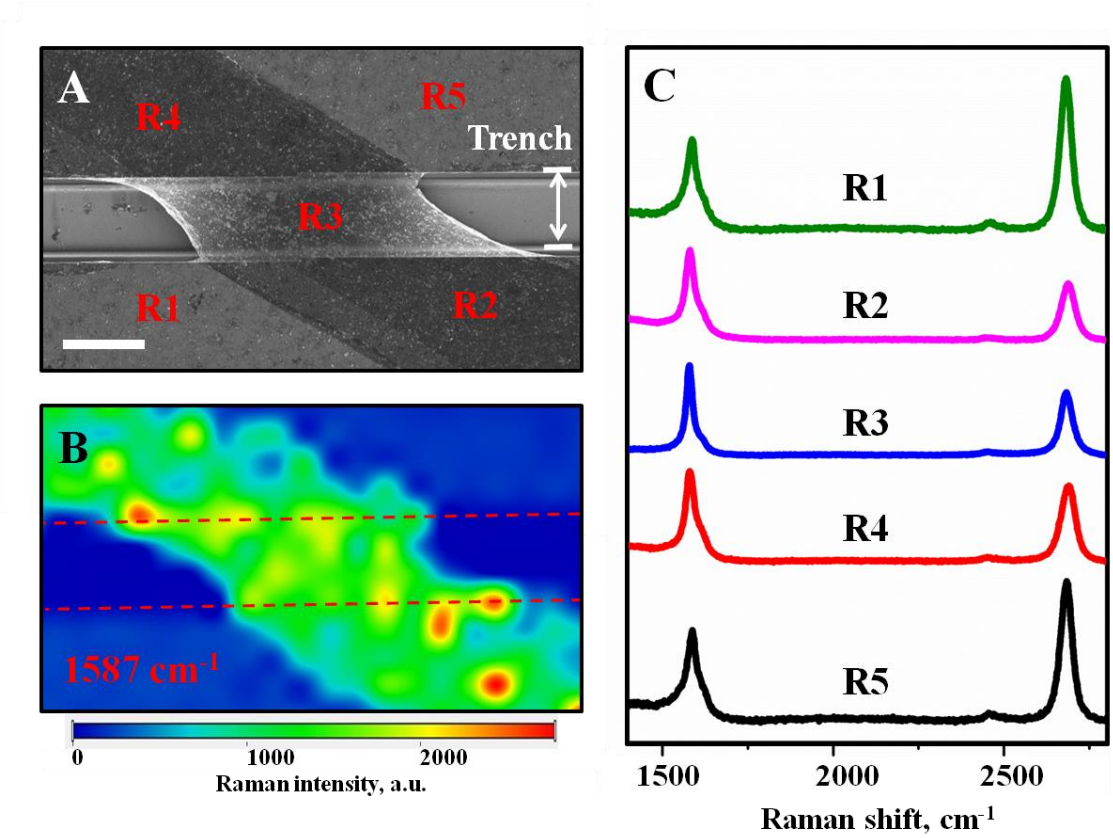

Figure 4.3 Raman spectra for the graphene ribbon annealed at 440 ℃. (A) The SEM image for the graphene ribbon with a scale bar of 5 μm. (B) The corresponding G band mapping at 1587 cm^{-1}. The trench is marked by red dotted lines. (C) Raman spectra (at λ=532 nm) with normalized G peak taken at different locations from the device. The laser power was 5 mW.

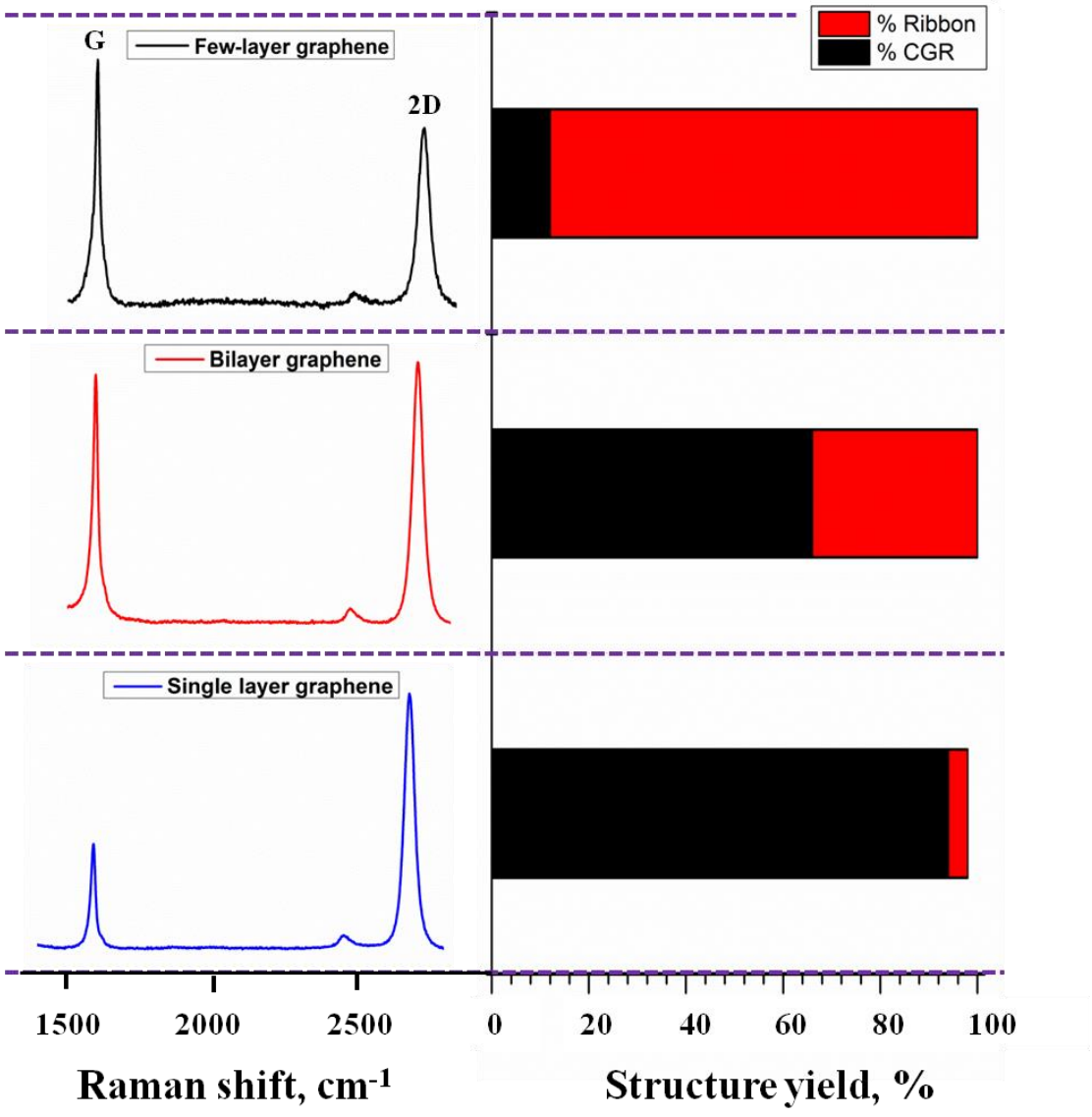

Figure 4.4 The structure yield for graphene with different number of layers. The left column shows the Raman resonance for the graphene that was used for annealing. The right column shows the percentage of different structures for the corresponding graphene.

In order to further investigate the influence of graphene layer number on the formation of CGRs, single-layer, bilayer and few-layer graphene were each transferred to separate dies and annealed under the same annealing conditions at 440 ℃. Figure 4.4 illustrates the yield of graphene structures for different layer numbers of graphene. We found that CGRs were the dominant structures when the graphene source was single layer (I(2D)/I(G) > 2). The bilayer graphene with comparable 2D and G peaks resulted in a considerably higher proportion of graphene ribbons, despite the fact that CGRs were still the main graphene structure. The overall morphology transition occurred when few-layer graphene was used, leading to an overwhelming yield of graphene ribbons. This correlation with graphene layer number may result from the difference of the thickness for the graphene films. Graphene with higher layer number may be less vulnerable to the distortion brought by PMMA evaporation, thus have less chance to form the curled structure.

4.3.4 Influence of PMMA

Table 4.1 Specifications of the PMMA and the resulting graphene structures.

PMMA	Molecular weight	Solids content	Film thickness after spinning (nm)	Percentage of CGRs	Average yield of the graphene structures per die
495K A2	495,000	2%	60	96%	41
495K A6		6%	320	89%	7
950K A2	950,000	2%	70	80%	27

Note: *All the graphene structures over the trench (on or off the device pattern) were accounted for in the statistics. The same spin-coat recipe with 4000 rpm and 45 s was applied.*

There is still another important factor that is indispensable for the formation of the CGR structures, the PMMA, which acts as a sacrificial support layer during the transfer process to guarantee the intactness of the graphene, and is the origin of the distortion leading to the morphology change of graphene during thermal annealing. Considering the wide variety of available PMMA solvents, it is important to study how PMMA with differing molecular weights and concentrations in anisole could affect CGR yield. We thus investigated how results differed between samples that used PMMA 495K A2, 495K A6 and 950K A2 that were annealed at 440 ℃ with single layer graphene. As specified in Table 4.1, all types of PMMA led to the dominant percentage of CGRs in the graphene structures obtained. However, there was a major difference in the average yield of graphene structures per die between different types of PMMA. For PMMA of the same solids content, 950K A2 with its higher molecular weight tended to break the suspended structures more easily and yield less graphene structures compared with 495 A2. A much bigger drop was found when the solids content increased. Since the thermal degradation rate constant of PMMA was independent of polymer concentration[88], the significant decrease of yield may be attributed to the increasing thickness of PMMA film resulting from the higher viscosity for 495K A6, which inevitably increased the amount of PMMA polymers that created distortions during the thermal annealing.

4.4 Conclusion

As a conclusion, we have demonstrated a simple method to curl the graphene ribbon and enhance the photocurrent response. The annealing temperature, thickness of graphene and the type of PMMA support layer have shown to be the key factors that

influence the formation of CGRs. The curling of graphene tends to take place in single layer graphene and requires relatively high annealing temperature. Besides, ultra-thin PMMA has also been shown to be necessary to obtain a decent yield of CGRs. These results have presented important progress toward the modification of graphene morphology and the production of appealing structures for optoelectronic applications.

CHAPTER 5

STUDY OF MECHANISMS OF THE PHOTORESPONSE IN CGRS

5.1 Overview

Graphene optoelectronics has become an attractive field to both theoretical and experimental researchers. The extremely high charge-carrier mobility, optical transparency, ultrafast photoluminescence, broadband absorption, and enormous tensile strength make graphene an ideal candidate for the future optoelectronic devices[1, 5, 29, 75, 93-102]. Enhancing the photon-to-electron conversion rate in graphene is the next step towards an efficient energy harvesting technology. Recent studies have shown that hot carriers can enhance the photocurrent response in graphene p-n junctions by the photothermoelectric effect (PTE)[99-101]. Moreover, this novel nonlocal hot-carrier-assisted transport regime is expected to increase power conversion efficiency in graphene-based energy-harvesting devices[99]. It is, therefore, desirable to synthesize graphene nanostructures with intrinsic PTE-induced photocurrent response.

Molecular dynamics (MD) simulations indicate that twisting a graphene nanoribbon leads to a tunable modification of the electrical structure of graphene[103-107]. The ability to change the physical properties of graphene simply by varying its morphology is an attractive option that makes the move to graphene-based photovoltaic technology more viable. Various graphene structures, such as stacked graphene

membranes[81], crumpled graphene films[82], and carbon nanoscrolls[83, 108], have been fabricated and have displayed distinct properties from pristine graphene. However, none of the above has demonstrated enhanced photocurrent response, a key component for future photovoltaics.

In Chapter 4, we have demonstrated a facile method to obtain a unique graphene structure which exhibits enhanced photoresponse. In this chapter, we further explore the optoelectronic properties of CGRs. Outstanding photocurrent enhancement has been observed, which is about two orders of magnitude greater than the photocurrent generated at the contact areas in flat graphene ribbon devices. We also investigated the nature of photoresponse in free-standing CGRs via gate-dependent scanning photocurrent microscopy. Our experimental results show that the enhanced photocurrent response in CGRs mainly originates from the PTE, while significant infrared emission may result from thermal radiation.

5.2 Materials and methods

5.2.1 Fabrication of CGR transistors

All the graphene used to fabricate the CGR devices in this chapter was all single layer graphene (SLG). SLG was grown on copper foils at 1000 ℃ in the presence of 20 sccm of methane and 100 sccm of hydrogen following the similar CVD process as presented in the previous chapter. Then a PMMA layer of 495K A2 was spin-coated on top of the graphene film that was grown on the top of the copper foil to hold the graphene

film. The copper foil was later removed through the wet etching in iron chloride solution, and then the PMMA-graphene film was transferred onto the pre-patterned chip, where 5-μm-wide and 5-μm-deep trenches were etched on 170-μm-thick transparent fused silica substrates via an Oxford 80 RIE and source and drain electrodes were deposited with 5 nm of Ti and 40 nm of Pt via an e-beam evaporator. After the device was dried in air, The sample was heated up to 440 ℃ under vacuum with a base pressure < 1 mTorr for 30 min in the presence of 200 sccm Ar and 20 sccm H_2, which led to a complete evaporation of the PMMA[109, 110]. During the evaporation, the non-suspended graphene adhered to the substrate due to the van de Waals interaction with the substrate, while the suspended part became wrinkled and crumpled, then shrank and curled into a CGR. We then separated each device by physically scratching between the electrodes with sharp needles.

5.2.2 TEM imaging

In order to fully understand the structures of CGRs, SLG was directly transferred onto TEM grids coated with lacey carbon films and similar annealing process was adopted to form CGRs. Bright-field TEM imaging was performed on an FEI Technai 20T operated at 80 kV. No obvious damage or structural transformation was observed on the CGRs under this voltage.

5.2.3 Scanning Photocurrent Measurements

The photocurrent measurement was performed through a microscope system with a spatially scanned CW laser. During the photocurrent measurements, the signals were

obtained using a preamplifier with the highest sensitivity within the measurement range. The reflection of the incident laser beam was simultaneously recorded by a Si detector. By overlapping the reflection image with the photocurrent image, the position of the sample was located. The photocurrent intensity of a CGR was analyzed by accumulating photocurrent signals in the center region of the CGR's spatial photocurrent mapping, for each incident laser power respectively.

5.3 Results and discussion

5.3.1 Structural details of CGRs and MD simulations

To explore the process of CGR formation, we collaborated with Dr. Pantelides' group in department of Physics and Astronomy at Vanderbilt University, who performed MD simulations on a 1-μm-long and 0.1-μm-wide graphene ribbon containing 3,840,000 C atoms. Each end (~ 10 nm) of the ribbon (shown in blue in Fig. 5.1B *left*) was kept flat with a restoring elastic force $F = kx$, according to the experimental conditions. Random momenta were given to a randomly selected group of atoms (shown in red dots in Fig. 5.1B *left*) to simulate the impulses given by PMMA thermal desorption, while the total momentum remained zero. The calculated morphology is in good agreement with the TEM image of a CGR, where we found that the CGR shows single-layer near the edge area (Fig. 5.1C) and has a multi-layer structure in the center region (Fig. 5.1C *inset*). The MD simulation results indicate that random momenta produced during the simulated PMMA evaporation process induce the formation of CGRs.

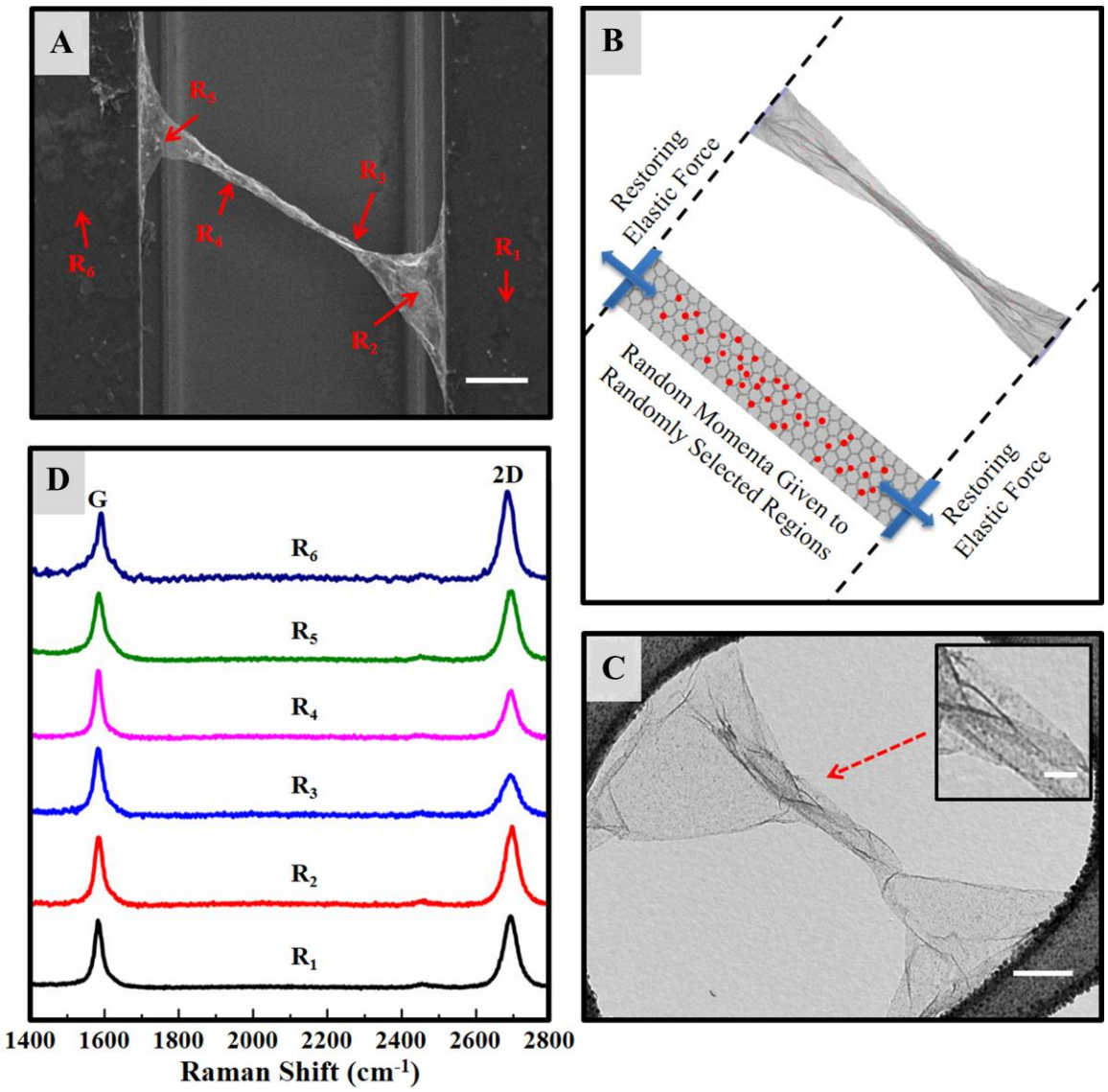

Figure 5.1 Structures and Raman Spectra of CGRs. (A) SEM image of a CGR device after annealing. The CGR was suspended across a 5-μm-wide and 5-μm-deep trench on a 170-μm-thick transparent fused silica substrate. The red arrows specify the spots where Raman spectroscopy was performed. The scale bar is 1 μm. (B) MD simulation cell with a restoring elastic force $\boldsymbol{F = kx}$ at each end and random momenta given to randomly selected regions (*red dots*) along the ribbon (*left*) and a CGR (*right*) resulted from the

ribbon on the left side. Credit Yevgeniy S. Puzyrev. (C) TEM image of a CGR. The scale bar is 200 nm. The inset shows a close-up image of the curled area with a scale bar of 50 nm. Credit Junhao Lin. (D) Raman spectra of six different regions along the CGR in (A) at 532 nm. The 2D-to-G intensity ratios are larger than 1 in the regions R_1, R_2, R_5 and R_6, indicating the presence of single layer graphene membrane. The broad 2D bands in the regions R_3 and R_4 may result from the interlayer interaction between different graphene layers within the CGR.

Raman spectroscopy was performed to inspect the resonance from the curled structure. We focused the 532 nm laser on six different spots (Fig. 5.1A), from the non-suspended to the suspended regions, to observe the Raman evolution while graphene became curled. As shown in Figure 5.1D, intense features could be found at ~ 1590 $cm^{-1}$and ~2680 cm^{-1}, corresponding to the G mode and 2D mode, respectively. We could identify the presence of single layer graphene from the sharp and symmetric shape of the 2D peak, as well as the 2D-to-G intensity ratio (>1) at the non-suspended regions (R_1, R_6). The CGR device still showed a similar behavior at R_2 and R_5 except a subtle shift of peak positions, possibly induced by the wrinkled and crumpled structures in these regions. As we moved further into the regions R_3 and R_4, where the graphene curled structure was formed, the 2D-to-G intensity ratio decreased substantially. The 2D bands also became broadened and asymmetrical, indicating that more scattering cycles were involved during second-order double resonance, which results from the interlayer interaction between different graphene layers within the CGR.

5.3.2 Enhanced photocurrent from CGR transistors

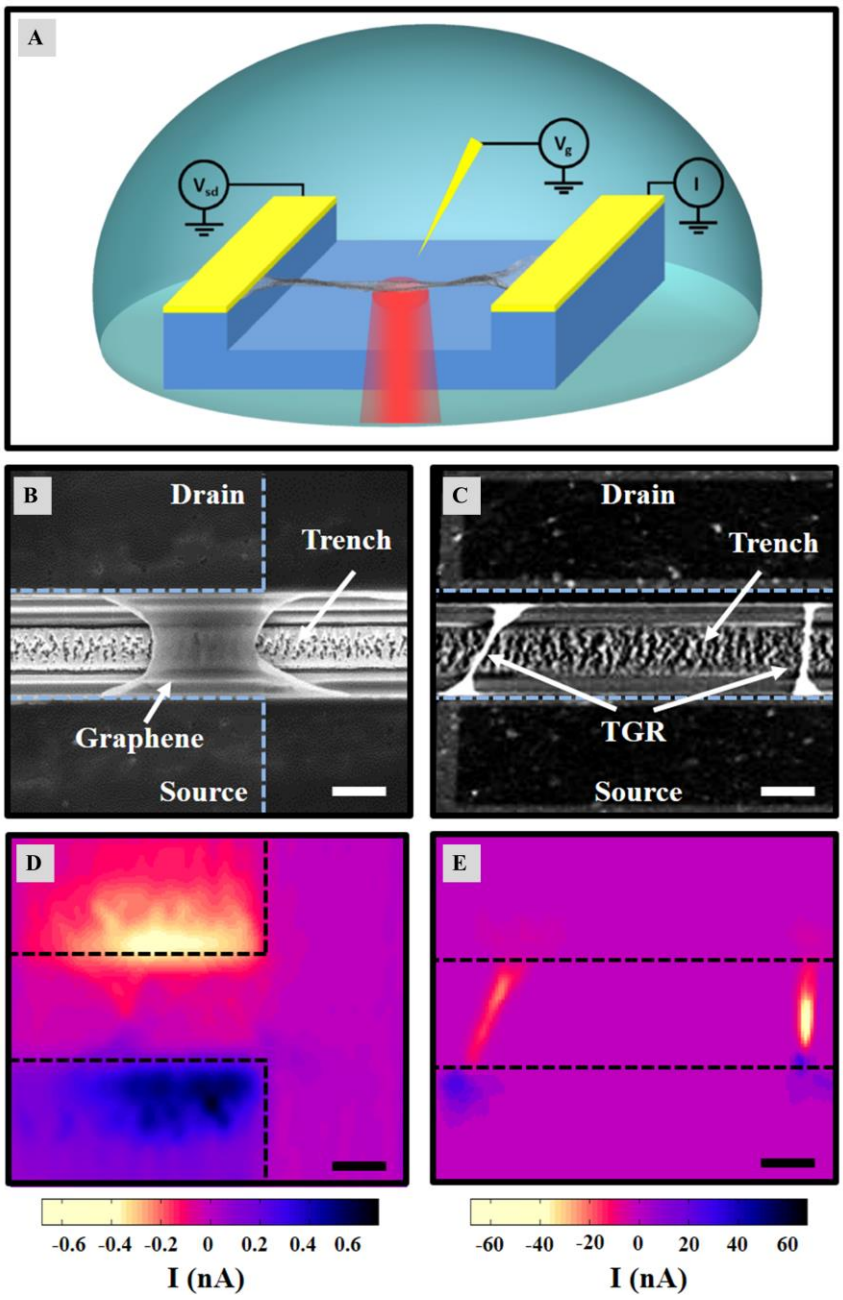

Figure 5.2 Optoelectronic response comparison between a CGR and a flat graphene ribbon. (A) Schematic diagram of the device geometry. A CGR is suspended cross a 5-μm-deep and 5-μm-wide trench on a 170-μm-thick transparent fused silica substrate.

Source and drain electrodes are used to apply a voltage across the CGR and the third electrode is used as an electrolyte gate. A diffraction-limited laser spot (< 500 nm) transmits from the transparent substrate to scan over the suspended CGR. SEM images of a suspended SLG device (B) and a suspended CGR device (C), respectively. The laser power was 1.2 mW for both images. The corresponding photocurrent images of the suspended SLG device (D) and the suspended CGR device (E), respectively. The scale bars represent 5 μm. Blue and black dashed lines are the edges of the electrodes.

To evaluate the photon-to-electron conversion efficiency of CGRs, we performed spatially resolved scanning photocurrent measurements on a suspended CGR via SPPM (Fig. 5.2A) in comparison with a flat graphene ribbon. Figure 5.2A presents a schematic diagram of a CGR device used in this study. When a diffraction-limited continuous-wave laser spot (1.2 mW, 785 nm) scans over a CGR transistor suspended on the top of a 170-μm-thick transparent fused silica substrate, the photocurrent signals are collected via a preamplifier and the refection image is recorded through a photodetector. As shown in Figure 5.2E, the photocurrent generated along a CGR is in the range of tens of nA, about two orders of magnitude greater than that generated at graphene-metal contacts in a suspended flat graphene ribbon transistor (Fig. 5.2D) and in non-suspended flat graphene ribbon transistors reported previously[99]. The intensity, sign, and symmetries of the photocurrent depend on the local morphology of CGRs.

5.3.3 Mechanisms of photocurrent generations in CGRs

In order to investigate the photocurrent generation mechanisms in CGRs, we performed gate-dependent scanning photocurrent measurements on CGR transistors. A free-standing CGR was sealed into a microfluidic chamber filled with 1.5 mM PBS solution and a gold electrode was used to change the electrochemical potential of the system. The chamber was kept in a steady stream to ensure a homogeneous concentration of ions. Figure 5.3A displays the SEM image of a CGR projected on its corresponding reflection image; the photocurrent image of this CGR is shown in Figure 5.3B, which was taken at a zero source-drain bias with a gate voltage Vg = 1.9 V. By sweeping the gate voltage from a value smaller than V_{dirac} (V_{dirac} = 1.62 V represents the Dirac point of this device) to larger than V_{dirac} while recording the photocurrent along the CGR, we obtained the gate-dependent scanning photocurrent map (Fig. 5.3C).

Three regions (R_1, R_2, and R_3) along the CGR were selected to study their photovoltage signal ($V_{pc} = I_{pc}R$) evolution as a function of the sweeping gate voltage. As shown in Figure 5.3D, the photovoltage signals in the region R_3 (R_1) exhibit strong non-monotonic gate voltage dependence and have a similar pattern to the calculated thermoelectric power (S), which may result from the PTE. However, the photovoltage response in the region R_2 shows monotonic gate voltage dependence, indicating that the photovoltaic effect (PVE), resulting from the built-in electric field, plays an important role in its photovoltage generation. It is therefore necessary to consider both PVE and PTE in the photovoltaic generation in CGRs, which can be expressed as

$$V_{PC} = V_{PVE} + V_{PTE} = \int \left(-\frac{\eta}{\sigma(n)} n_x \mathrm{e}\, \partial V + S(x)\, \partial T_e(x)\right) dx \qquad (6)$$

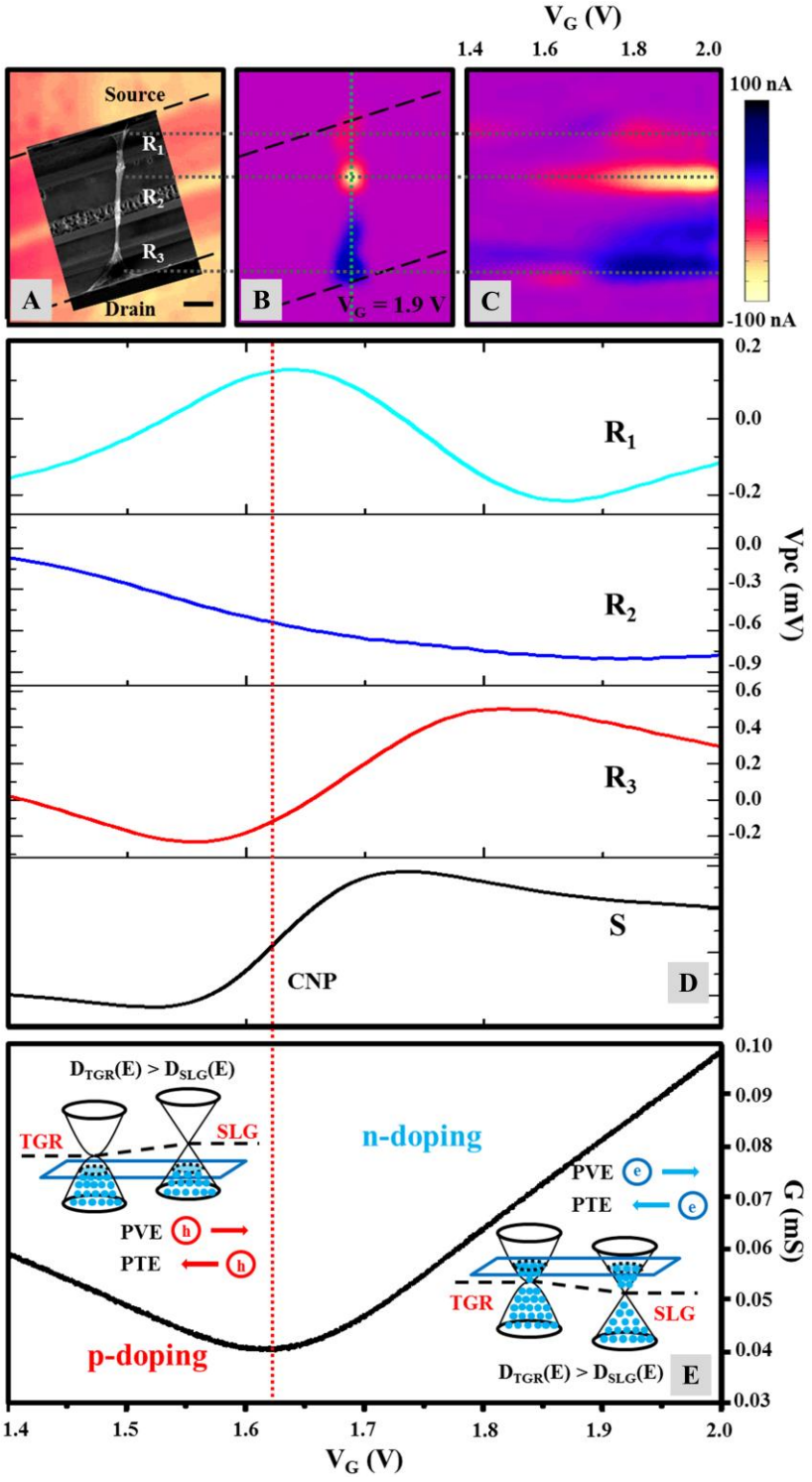

Figure 5.3 Photocurrent responses of a CGR device. (A) An SEM image of a CGR device projected on the corresponding reflection image. The scale bar is 1 μm. (B) The

corresponding photocurrent image at V_g = 1.9 V and a zero source-drain bias. The laser scanning position is indicated by the green dotted line. (C) The gate-dependent scanning photocurrent image as V_g varying from 1.4 V to 2.0 V. (D) The horizontal cuts along the dotted lines for different regions (R_1, R_2, and R_3) in the CGR as specified in the photocurrent images. The bottom curve shows the calculated Seebeck coefficient in the R_3 region. (E) Conductance measurement of the CGR device as a function of V_g. The flowing directions for different major carriers are illustrated in the inset diagrams.

---

where $\sigma(n)$ is the local conductivity at the curled area, T_e is electron temperature, η and n_x are the mobility and the density of the photoexcited carriers, respectively, and S is the Seebeck coefficient. According to the Mott relation,

$$S = -\frac{\pi^2 k_b^2 T_e}{3e} \frac{d(ln\sigma)}{dV_g} \frac{dV_g}{dE}\Big|_{E=E_F} \quad (7)$$

where $k_b$is the Boltzmann constant, e is the electron charge, and E_F is the Fermi energy. $d(ln\sigma)/dV_g$ derived from the conductance measurement plays a key role in the photovoltage generated from the PTE, whereas the contribution of PVE largely depends on the local potential gradient ΔV. The detailed calculations for the carrier mobility and Seebeck coefficient in CGR are specified in Appendix D.

As discussed previously, the relatively-low 2D-to-G intensity ratio and the broad 2D bands in the curled regions (Fig. 5.1D) may result from the interlayer interactions between graphene planes. This interlayer interaction may lead to an increase of the density of states (DOS) in the curled multi-layer region of a CGR, since the interlayer

interaction can induce a parabolic dispersion of the energy bands in multi-layer graphene as compared to a linear dispersion of the energy bands in SLG[111-113]. As a result of the Fermi level alignment, the Dirac point of a CGR is higher than that of a SLG, leading to the formation of a built-in electric field. As illustrated in Figure 5.3E, for the n-doped graphene, the photoexcited electrons flow from the CGR to the SLG due to the built-in electric field. However, according to the second law of thermodynamics, the hot carriers induced by PTE tend to diffuse to the regions with larger DOS to maximize the entropy, leading to electron flow from the SLG to the CGR. In the region R_1 (R_3), electrons flow from the SLG to the CGR and produce a negative (positive) photocurrent, which mainly results from the PTE. In the highly curled region R_2, the contribution of PVE increases, which overwhelms the PTE-induced electron flow and produces a negative current with the present experimental setup. This may indicate that the photocurrent generation depends on the local morphology of a graphene structure.

To better understand the physics behind the photocurrent generation in CGR devices, more CGR samples were fabricated and tested according for comparisons and further analysis. In order to eliminate the interference from the electrodes, we picked CGRs located far away from the electrodes (SLG hence acted as the interconnections between CGRs and electrodes). The SLG membranes used in the experiments were shown to be p-doped after growth and transfer processes.

We found that a significant slope located at the T/R_2 interface, which might be caused by the high local potential gradient. The PTE effect could be substantially enhanced at the T/R_2 interface due to the high steepness of the local potential gradient, which resulted in the overwhelming flow of photo-excited holes from the curled area to

R_2. Although counterbalanced by the diffusion of holes from the curled area into the T/R_1 interface, where lower potential gradient might be formed, the net photocurrent in the curled area would still be dominated by the negative current. Compared to PVE, the

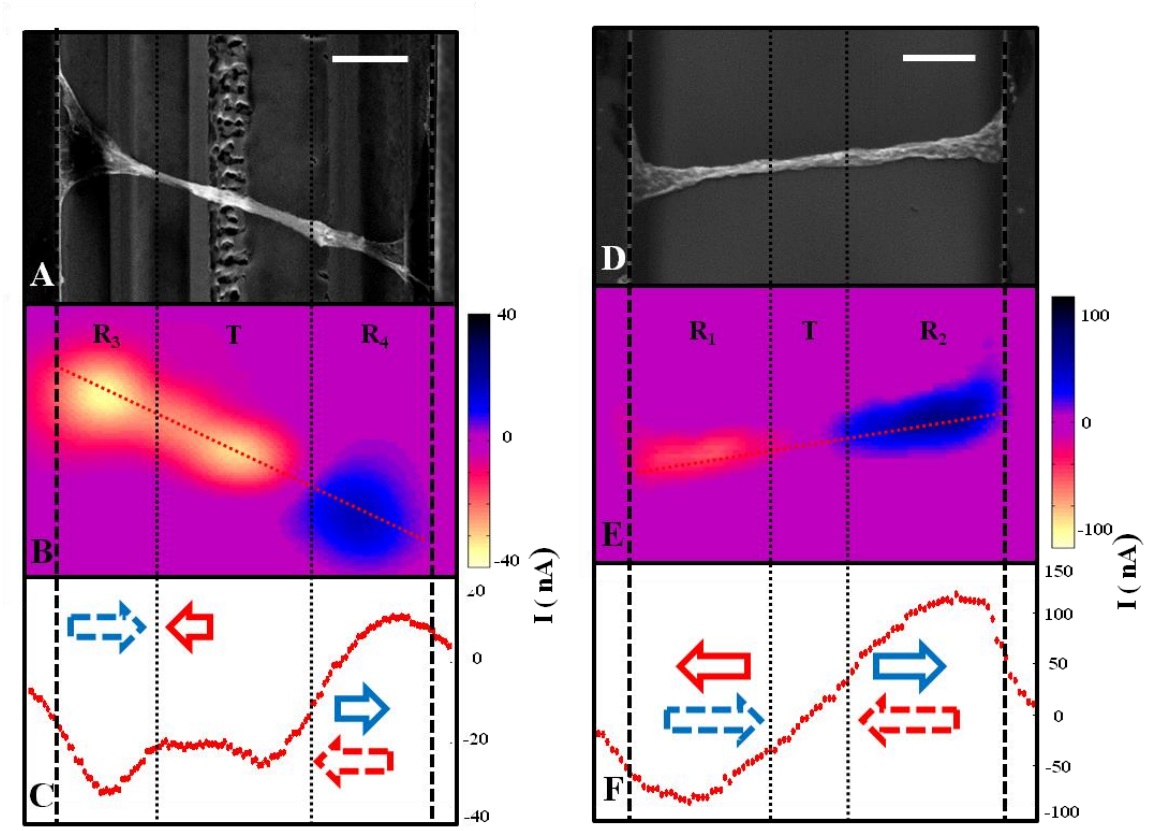

Figure 5.4 Photocurrent response of CGRs[66]. (A) and (D) SEM images of suspended CGRs. The scale bars are 1 μm. (B) and (E) the corresponding photocurrent images of CGRs. (C) and (F) Line-cuts from the photocurrent images along the CGR devices as marked in the red dotted lines. The solid arrows and the dotted arrows refer to the contributions from PVE and PTE respectively. Blue color represents the negative current in the present experimental setup and red color corresponds to the positive current.

influence from PTE was relatively weaker in the curled area, but stronger in both SLG sides. The PTE induced photocurrent might be responsible for the positive current in R_2, resulting from the hole injection from the SLG side to the curled area in the middle. Meanwhile, since PVE induced photocurrent was weaker at the R_1/T interface due to the smoother local potential gradient, PTE might be also responsible for the negative current shown in R_1, which could be attributed to the flow of holes from the SLG side to the curled area.

Besides, we also observed different photo-responses from another CGR device as shown in Figure 5.4 E. Two comparable colors could be seen in the photocurrent image. For this device, a narrow curled area was found to locate at the middle of the CGR device. Unlike the previous device, the symmetric current changes shown in Figure 5.4 E indicated that this CGR device might not have steep changes in terms of potential gradient. As a result, the photocurrent in the curled was mostly neutralized, and the net current at interfaces of R_3/T and T/R_4 was slightly overwhelmed by the PTE induced photocurrent.

5.4 Conclusions

In conclusion, the enhanced photoresponse from the free-standing CGRs has been further investigated. Gate-dependent photocurrent measurements indicate that the photocurrent signals mainly result from the PTE effect, which may be attributed to the interlayer interactions in the curled area. The experimental results provide useful insights for understanding the opto- and thermo- electronic properties of graphene based transistors.

CHAPTER 6

CONCLUSIONS

In this dissertation, the electronic and optical properties of two appealing carbon nanomaterials, CNTs and graphene, have been thoroughly studied, allowing us to get a glimpse of the fascinating nature of CNTs and graphene. This chapter will summarize the results we observed and discuss future directions for CNTs and graphene.

6.1 Research summary and future directions for CNTs

The study of material synthesis is important to the understanding of the growth mechanism. In Chapter 2, we aimed to control the growth morphology of CNTs in order to produce CNTs that can meet the requirements of different applications. Two different strategies were developed to change the growth morphology of CNTs from the low-density surface growth to the high-density forest growth. The first strategy employed a short acetylene pulse which was introduced at the beginning of the growth. We observed that by extending the acetylene pulse time, the density of as-grown CNTs could be significantly enhanced, accompanied by a morphology transition from surface growth to forest growth. However, Raman spectroscopy indicated that the quality of as-grown CNTs might be compromised when the acetylene pulse increased. In the second strategy, we showed that the growth morphology of CNTs could also be controlled by adjusting

the growth temperature. Higher temperatures tended to produce CNTs in the form of surface growth. Besides, through the Raman inspection, we also found that the quality of as-grown CNTs could be improved when the temperature increased.

CNT biosensors were developed in Chapter 3. In order to potentially observe the interaction between CNTs and biomolecules at the single molecule level, suspended semiconducting CNT transistors were fabricated and investigated in an aqueous environment where most biomolecules could survive. Scanning photocurrent measurements were employed to image and locate the position of suspended CNTs in solution. During gate-dependent photocurrent measurements, semiconducting CNTs exhibited excellent sensitivity to the environment potential changes. The photocurrent response of the CNT showed distinct behaviors at different local spots, indicating the possibility of using small segments of the CNT as local optoelectronic sensors. Through the theoretical calculation, the photocurrent change of the local sensor was in the order of hundreds of pA when a single electron was introduced into the system, which was two orders of magnitude greater than the minimum current we can measure.

There are a few interesting topics for continued exploration. In the study of the morphology control of CNTs, we have shown the possibility to produce CNTs with different morphologies within a single growth procedure (Fig. 2.4 C). Further investigations may focus on combining the surface growth with the forest growth, and potentially developing a simple method to grow all-CNT field-effect transistors that assemble both horizontally- and vertically-grown CNTs in three-dimensional structures. Besides, as we have already identified, the first 5 s of acetylene pulse time is able to promote the yield of CNTs without compromising the tube quality. A possible reason

may be due to the higher demand of acetylene for the nucleation stage than the following growth stage. This effect of "clean boost" should be further studied. It may be possible to use an acetylene pulse that decreases over time to provide high quality CNTs in any desired morphology. As demonstrated in Chapter 3, we have successfully developed a highly sensitive CNT biosensor. Exciting opportunities exist for using the CNT biosensors to observe the interactions between CNTs and different biomolecules. Currently, we have already built a dual-trap optical tweezer which is able to manipulate single biomolecules. However, it remains to be difficult to observe the single-molecule interaction due to the nanoscale Debye screening length in our system.

6.2 Research summary and future directions for graphene

Despite the extraordinary electron mobility, the optoelectronic properties of graphene are highly limited by its zero band-gap nature. In Chapter 4, we developed a simple method to enhance the photoresponse in graphene by curling the graphene ribbons through thermal annealing. The resulting graphene structures, CGRs, exhibited remarkable optoelectronic response. The photocurrent generated in CGRs was observed to be much great than that generated in flat graphene ribbons. Through the further study of different factors that influence the formation of CGRs, we found that the curling of graphene favored single layer graphene and required relatively high annealing temperature. Also, ultrathin PMMA was necessary to obtain a high yield of CGRs.

The following study in Chapter 5 further investigated the optoelectronic properties of this unique graphene structure. The TEM imaging and Raman inspection

indicated that the enhanced photoresponse might be attributed to the interlayer interaction between tightly stacked graphene layers within CGRs. During the photocurrent measurement, we observed that electrons tended to flow from the single layer graphene to the CGR, indicating a significant influence from the PTE effect. We further investigated the mechanism of the photocurrent generation in CGRs by gate-dependent photocurrent measurements. The observed photovoltage at the interfaces between CGRs and single layer graphene was in good agreement with the calculated Seebeck coefficient, indicating that the enhanced photocurrent response in CGRs mainly originated from the PTE effect.

The study of optoelectronic properties of CGRs in this thesis is just a beginning. Future investigations about the optoelectronics of CGRs can be conducted to tune their photoresponse by controlling the morphology of CGRs. We have showed in Figure 5.4 that the photoresponse of CGRs may be correlated with their local morphologies. It may be possible to make CGRs with desired photoresponse if the curling of graphene could be better controlled. A potential approach is to utilize e-beam lithography to design different patterns of graphene ribbons, such as triangular shapes and rectangular shapes, which may lead to different curling strategies and form CGRs with distinct morphologies.

Appendix A

CARBON NANOTUBE SYNTHESIS

A.1 Recipe for suspended CNT bridges

1. Check that the gas cylinders have plenty of gas (the pressure inside a full cylinder is about 2000 psi)
2. Connect flow channels at the left side of the furnace (be sure to check for gas leak with bubble solution)
3. Open the furnace lid
4. Put sample into the quartz boat and use the magnetic stir bar to slide the boat into the center of the furnace
5. Mark the correct final position of the quartz boat by drawing a line at the edge of the magnetic stir bar
6. Slide the boat out carefully until the sample rests ~ 1-2" outside the furnace
7. Start flowing Ar = 0.8 SLM
8. Check that the water is bubbling to ensure the gas flow
9. Connect the right end of the glass tube with the exhaust system
10. Close the furnace lid
11. Turn on the furnace and set the temperature to 600 °C

12. When the furnace reaches 600 °C (~ 5min), turn on H_2O=0.1 SLM, leaving the Ar on. Slide the boat into the marked position quickly (fast heating to avoid aggregation) and treat the sample for 10 min.
13. Turn off H_2O and turn on H_2=0.2 SLM, leaving the Ar on. Let H_2 flow for 15 min for thermal annealing.
14. Slide the boat carefully out until the sample rests 1-2" outside the furnace
15. Turn off the flow of H_2, leaving the Ar on
16. Raise the furnace setpoint to 815 °C and wait until the gases are stabilized (~4 min)
17. Turn on all the gases, Ar=0.8 SLM, H_2=0.2 SLM, CH_4=0.8 SLM, and C_2H_2=0.2 SCCM. Let the gases to stabilize for 3-4 min. The role of H_2 at this step is to re-activate the catalyst during the growth process. However, since H_2 might etch CNTs under high temperature, the dose should not exceed H_2=0.2 SLM.
18. Turn off the Ar and wait for at least 2 min. Then slide the boat to the marked position to start the growth.
19. Allow at least 20 min for CNTs to grow
20. Slide the boat carefully out until the sample rests 1-2" outside the furnace
21. Turn on Ar= 0.8 SLM and wait for 1 minute
22. Turn off all other gases.
23. Decease the temperature of furnace to 0 °C, and prop the lid open with the metal block to speed up the cooling process
24. At 500 °C, we can completely open the furnace lid to further speed up the cooling process

25. At 100 °C, we can open the right end of the tube and remove the sample
26. Turn off Ar and disconnect flow channels
27. Close gas tanks
28. Check if the tube or the boat is dirty (if it is, disconnect the glass tube with the gas tubing. Allow the room air to flow into the tube. Set furnace temperature to 950 °C, and clean the tube/boat for 15 minutes. If the tube/boat is too dirty to be cleaned by air, try 200 SCCM Ar through water bubbler)

A.2 Recipe for upright forest growth

1. Check that the gas cylinders have plenty of gas (the pressure inside a full cylinder is about 2000 psi)
2. Connect flow channels at the left side of the furnace (be sure to check for gas leak with bubble solution)
3. Open the furnace lid
4. Put the sample into the quartz boat and use the magnetic stir bar to slide the boat into the center of the furnace
5. Mark the correct final position of the quartz boat by drawing a line at the edge of the magnetic stir bar
6. Slide the boat out carefully until the samples rests ~ 1-2” outside the furnace
7. Make sure the valve to the vacuum pump is off (on the right side of the setup)
8. Start flowing Ar=0.8 SLM
9. Check that the water is bubbling to ensure the gas flow

10. Connect the right end of the glass tube with the exhaust system
11. Close the furnace lid
12. Turn on the furnace and set the temperature to 600 °C
13. Turn on H_2O=0.1 SLM, leaving the Ar on. Slide the boat into the marked position and treat the sample for 10 min.
14. Turn off H_2O and turn on H_2=0.2 SLM, leaving the Ar on. Let H_2 flow for 15 min for thermal annealing.
15. Slide the boat carefully out until the sample rests 1-2" outside the furnace
16. Turn off H_2, leaving Ar on
17. Raise the temperature setpoint of the furnace to 765 °C and wait until the gases are stabilized (~4 min)
18. Turn on all gases (Ar=0.8 SLM, H_2=0.2 SLM, CH_4=0.8 SLM and C_2H_2=1.2 SCCM) and stay for 3-4 min to stabilize
19. Turn off Ar and wait for at least 2 min. Then slide the boat to the marked position
20. Allow at least 30 min for CNT-forest growth
21. Slide the boat carefully out until the sample rests 1-2" outside the furnace
22. Turn on Ar= 0.8 SLM and wait for 1 minute
23. Turn off all other gases.
24. Decrease the furnace temperature to 0 °C and prop the lid open with the metal block to speed up the cooling process
25. At 500 °C, we can completely open the furnace lid to further speed up the cooling process
26. At 100 °C, we can open the right end of the tube and remove the sample

27. Turn off Ar and disconnect flow channels
28. Close gas tanks

A.3 Recipe for hot-filament forest growth

1. Check if we have plenty of gas, connect the tube properly. Make sure the C_2H_2 gauge is below the red line.
2. Put the sample on the boat and insert it to the appropriate position in the chamber (about 1 inch away from the filament), then mark the position of the tube. Slide the boat out the sample rests 5~10'' outside the furnace.
3. Purge the system with 0.2 SLM Ar for 5 min. Turn off Ar and pump the system down to 7~8 millitorrs.
4. Turn on H_2 = 0.2 SLM.
5. Turn on the hot filament. Gradually increase the voltage and current until the filament shines brightly.
6. Turn on C_2H_2 = 2.7 sccm. The filament will now become a little dimmer. Try to increase both current and voltage a little bit.
7. Turn on CH_4 = 80 sccm. Wait for 5 min until the gases mix well.
8. Turn on the furnace and heat the chamber to 650 ℃.
9. Slide the boat into the chamber and let CNTs grow for 20 min.
10. Slide the boat carefully out until the sample rests 1-2" outside the furnace.
11. Turn off the hot filament. The voltage and current should be zeroed before turn off the power.

12. Turn off all the gases.
13. Turn off the furnace and cool down the system.
14. Turn off the power of pumping machine before loose the speedivalve. (The pumping machine would be broken if the pressure of the system goes beyond 10 Torr. So under any circumstances, it's best to make sure the pressure is below 8 Torr.) Turn off the pressure gauge.

Appendix B

Photolithography fabrication

The CNT devices contain four layers of fabrication. Most fabrications were performed at Cornell Nanoscale Science & Technology Facility (CNF). Please follow the recipe layer by layer, step by step. This recipe is also able to provide devices for graphene.

B.1 Preparations of the wafers and masks

Start with a clean 4-inch wafer. This recipe has been developed for silicon wafers with a 200–1000 nm oxide or for 170–500 μm-thick fused silica wafers. With Si/SiO_2 wafers (from Nova Electronics), it is useful to check the thickness of the oxide layer using the Leitz MVSP Spectrophotometer before beginning any processing. With fused silica wafers (from Mark Optics), there is no film to measure (and one cannot use an interferometer anyway), but since both sides of the wafer look transparent and highly identical, it is useful to make a small scratch on one side to keep track of which side is up.

To create masks for each photolithography step, the steps listed below should be followed. Extra cautions have to be taken since all the mistakes made at this level will reflect to the fabrication products. Patterning errors should be avoided and the masks should be kept as clean as possible when not in use:

1. Design masks using L-Edit. Refer to the 5x Stepper manual on the CNF website for size limitations and instructions on alignment marks. Differentiate different fabrication layers with different colors.
2. Expose patterns on a new 5-inch photomask (glass coated with a thin layer of chrome and photoresist) in the GCA/MANN 3600F Optical Pattern Generator (also named PG Mask Writer). This instrument is almost always sufficient to write masks intended for 5X or 10X GCA steppers. The mask writing rate is roughly 2000 exposures/hour. Check the flash points before writing the mask. For tasks with sophisticated patterning or large workload (> 4000 flash points, usually happens for the mask intended for the contact aligner), please refer to the Heidelberg DWL66 Laser writer.
3. After the exposure, put the mask in the Hamatech Mask Plate Processor to develop (Program 2) and etch (Program 1) the mask. Strip remaining resist in the hot strip baths in the resist room for 10 min per bath (2 strip baths and 1 rinse bath). Then run through the spin rinse dryer.

B.2 Trench and GCA key:

GCA keys are the marks for the alignment of the following layers. Thus they must be added in the first lithographic step so that subsequent layers can be aligned to this first layer. To make suspended nanotubes, the trenches can be etched at this step as well. Besides, for Si/SiO_2 wafers, it is also convenient to etch holes through the SiO2 layer to

make back-gate pads at this step. The following steps illustrate the fabrication of the first layer.

1. Prime the wafer with P20, wait at least 20s before spinning. Then spin at 4000 rpm, 1000 acceleration, for 30s. The P20 primer makes the wafer hydrophobic so that the photoresist can easily stick on it.
2. Spin coat a photoresist layer above the primer. Use SPR 220 – 3.0 resist and spin at 2000 rpm, 1000 acceleration, for 30s.
3. Soft-bake the wafer at 115 C for 90s. Then cool it on the heat sink.
4. Expose the wafer using autostepper, the exposure time is ~0.35s, focus is 0.
5. Post-bake the wafer at 115 C for 90s.
6. Develop the wafer in MIF300 for 90s, rinse with DI water, and blow dry with compressed N_2. For Si/SiO2 wafers, the Hamatech-Steag Wafer Processor can be used to automatically develop the wafer.
7. Check the patterns under microscope. Make sure the trench and GCA key are well defined. Incomplete exposures will result in trenches with insufficient width during RIE etching.
8. Check the thickness of the resist using P10 profilometer.
9. Use Oxford 81 with the recipe CHF_3/O_2 to etch the trench on fused silica wafers. Before etching, make sure to do the oxygen clean using the default recipe. For Si/SiO2 wafers, etch through the oxide layer with the recipe CHF_3/O_2, and then etch into the Si substrate for 5 min with CH_4 or SF_6 plasma.
10. Clean the chamber with oxygen plasma every one hour. During this time, take out the wafer and use P10 to check the thickness of the remaining resist, as well as the

depth of arrow regions. Then estimate the etching ratio. Make sure there is enough photoresist remaining before each etching cycle. Over etching the wafer will lead to the formation of complex polymers that do not dissolve or react with any known acid/base/organic solvent in the clean room.

11. Keep etching until the remaining resist is less than 1 um thick, which happens normally after 2 – 2.5 hours of etching. Clean the residues with oxygen plasma.
12. Check the patterns under microscope.

B.3 Electrode

Metal electrodes are patterned on the surface to make contact with both ends of the CNTs and, on Si/SiO_2 substrates, to make contact with the Si back gate. If the CNTs are grown over trenches, electrodes must be defined before growth, or the CNTs will no longer be suspended; otherwise, the electrodes may be deposited after growth. If electrodes are deposited before growing nanotubes, the electrode metal must be platinum to survive the CNT growth temperature.

1. Dehydrate the wafer at 180 C for at least 5 min.
2. Prime the wafer with P20, wait at least 20s before spinning. Then spin at 4000 rpm, 1000 acceleration, for 30s.
3. Spin coat a LOR resist layer above the primer. Use LOR 5A and spin at 4000 rpm, 1000 acceleration, for 30s. The LOR resist is an ultra-thin resist that helps to make a better undercutting during the exposure, and hence make it easier for the

lift-off process. Compared to the image reversal method, LOR resist is more reliable and efficient.

4. Bake the wafer at 180 C for 5 – 10 min.
5. Spin coat a photoresist layer above LOR. Use SPR 700 – 1.2 resists and spin at 4000 rpm, 1000 acceleration, for 30s.
6. Soft-bake the wafer at 115 C for 60s. Then cool it on the heat sink.
7. Expose the wafer using autostepper, the exposure time is 0.27s, focus is 0. Remember to change the Y offset from -3.000 to -2.999. The LOR resist does not require additional exposure dose.
8. Post-bake the wafer at 115 C for 60s.
9. Develop the wafer in MIF300 for 90s. Then blow it dry.
10. Check the patterns under microscope. Make sure the trench is sitting between the electrodes.
11. (Optional) Use Oxford 81 to descum the wafer for 30s by oxygen plasma.
12. Use the odd hour evaporator to deposit 5 nm Ti followed by 40 nm Pt. The evaporation speed should be maintained between ~ 0.7 A/s and 2 A/s to obtain high quality electrodes.
13. Lift-off the photoresist and unnecessary metal in acetone for 1 – 4 hours.
14. Lift-off the residues and LOR resist in 1165 for 1 – 4 hours (overnight soaking is preferred).
15. Rinse the wafer with DI water and blow it dry.

B.4 Catalyst

Catalysts are patterned on top of the electrodes to grow CNTs. Although this layer can be finished by regular photoresist only, it's recommended to use LOR resist for better patterning. To use LOR resist, please refer to steps 1-4 on B.3 of Appendix B.

1. Prime the wafer with P20, wait at least 20s before spinning. Then spin at 4000 rpm, 1000 acceleration, for 30s
2. Spin coat a photoresist layer above the primer. Use SPR 700 – 1.2 resist and spin at 4000 rpm, 1000 acceleration, for 30s
3. Soft-bake the wafer at 115 C for 60s. Then cool it on the heat sink.
4. Expose the wafer using autostepper, the exposure time is 0.27s, focus is 0. Keep the Y offset at -2.999.
5. Post-bake the wafer at 115 C for 60s.
6. Develop the wafer in MIF300 for 90s. Then blow it dry.
7. Check the patterns under microscope. Make sure the catalyst pads aligned well on electrodes and do not cross into the trench.
8. (Optional) Use Oxford 81 to descum the wafer for 30s by oxygen plasma.
9. Use the even hour evaporator to deposit 10 nm Al_2O_3 followed by 3 A Fe. The evaporation speed of Fe should be ~ 0.3 A/s. The film thickness of Fe should be as accurate as possible to ensure the growth of single-walled CNTs.
10. Lift-off the photoresist and unnecessary residues in 1165 for 4 – 8 hours (overnight soaking is preferred).
11. Rinse the wafer with DI water and blow it dry.

B.5 Insulation layer

This layer is optional. The insulation layer is used to cover most of electrode bars and protect them from circuit short in the aqueous solution with electrolyte.

1. Dehydrate the wafer at 180 C for at least 5 min.
2. Prime the wafer with P20, wait at least 20s before spinning. Then spin at 4000 rpm, 1000 acceleration, for 30s.
3. Spin coat a LOR resist layer above the primer. Use LOR 5A and spin at 4000 rpm, 1000 acceleration, for 30s.
4. Bake the wafer at 180 C for 5 – 10 min.
5. Spin coat a photoresist layer above LOR. Use SPR 700 – 1.2 and spin at 4000 rpm, 1000 acceleration, for 30s.
6. Softbake the wafer at 115 C for 60s. Then cool it on the heat sink.
7. Expose the wafer using autostepper, the exposure time is 0.27s, focus is 0. Keep the Y offset at -2.999
8. Postbake the wafer at 115 C for 60s.
9. Develop the wafer in MIF300 for 90s. Then blow it dry.
10. Check the patterns under microscope. Make sure all electrode bars are covered by the patterns.
11. (Optional) Use Oxford 81 to descum the wafer for 30s by oxygen plasma.
12. Use the even hour evaporator to deposit 30 nm Al_2O_3.
13. Lift-off the residues and LOR resist in 1165 for 4 – 8 hours. (Overnight soaking is preferred)
14. Rinse the wafer with DI water and blow it dry.

B.6 Dice the wafers

Since fused silica wafers have no crystal axes, it is necessary to dice them using the K&S 7100 Dicing Saw. It is also good to dice Si/SiO2 wafers to avoid the device damage during manual clipping. Using the dicing saw is much messier than dicing by hand, this tool much be well practiced with dummy wafers.

1. Fused silica wafers can only be cut with the all-purpose blade. Si/SiO2 wafers can be diced with any saws. Schedule accordingly before using the dicing saw.
2. Before dicing the wafer, spin a photoresist coating to protect the features made already.
3. Use UV tapes to hold fused silica wafers with the dicing frame. Use regular blue tapes to hold Si/SiO2 wafers.
4. Fused silica wafers can only be cut with the all-purpose blade. Schedule accordingly before using the dicing saw.
5. Load the dicing frame into the tool. Enter the desired parameters of wafer thickness (170 μm for fused silica wafers, 500 μm for Si/SiO2 wafers), cutting depth, cutting schemes for 0/90 degree.
6. Align the blade for each cutting angle and starting dicing.
7. Expose the wafers under UV lamp for 10 min to remove the UV tape. Si/SiO2 chips can be directly stripped away from the blue tape.
8. Clean each chip in 1165 for 10 min and rinse with DI water.

Appendix C

GRAPHENE SYNTHESIS AND PREPARATION

C.1 Recipe for Graphene growth

1. Prepare Cu foils for graphene CVD growth. Cut the Cu foil into the desired size, and flatten the foil if necessary.
2. Treat the Cu foil with acetone for at least 10 min, followed by 10 seconds of IPA and 10 seconds of H_2O. Then blow the foil dry gently with the nitrogen gun. In order to grow high quality graphene, the Cu foil may need to be as clean as possible. For this case, an extra cleaning step by sonication may be added after soaking in acetone. Noted that although the sonication may improve graphene quality, it also makes numerous wrinkles in Cu foil, which may limit the grain size of graphene.
3. Wipe down the quartz boat with acetone, and place the Cu foil into the quartz tube. Carefully load the boat into the tube, and use the magnetic stir bar to transfer the Cu foil to the center of the tube
4. Connect the left end of the tube with the flow line, right end with the pump and vacuum flange using clamps.
5. Turn on the pump, wait 1 minute. Turn on the pressure gauge.
6. Slowly open the speedivalve to pump down the system. Purge the gas lines with argon, methane, and hydrogen respectively.

7. Wait until the pressure gets below 10 millitorr.
8. If the desired level of vacuum can't be achieved, use ethanol to check seals; the leak will lead to an obvious pressure change.
9. Before starting the growth, record the base pressure and humidity. Flow Ar (100 SCCM). The current pressure should be ~3.4 * 10^{-1} Torr.
10. Start to flow 10 SCCM of H_2.
11. Set the furnace temperature to 900 °C and annealing the sample for 1 hour.
12. After annealing, raise the temperature to 950 °C. Once the desired temperature is reached, turn off Ar and change the flow of H_2 to 100 SCCM. Meanwhile, start to flow 20 SCCM of CH_4. Adjusting the parameters at this step could result in graphene growth with different layer numbers as needed. Usually, with the present furnace system, 20 sccm CH_4 : 100 sccm H_2 at 950 °C could produce high quality single layer graphene; 20 sccm CH_4 : 100 sccm H_2 at 900 °C could produce high quality double layer graphene; 50 sccm CH_4 : 15 sccm H_2 at 900 °C could produce multi-layer graphene.
13. After 30 minutes of growth, set the temperature to zero and move the quartz boat out of the hot zone for fast cooling. Turn off H_2 and CH_4. Leave Ar flow to purge the system.
14. Restart the heater to monitor the temperature. Prop the furnace open with the metal disk.
15. When the temperature reaches 450° C, open the furnace completely.
16. Wait until the system is completely cooled down.

17. Disconnect the clamp on the right side. Slowly close the speed valve and turn off the pump. Wait until the system is fully re-pressurized by Ar.
18. Open the system and take out the boat carefully using magnetic stir bar.
19. Close all cylinders and valves, and turn off the temperature controller.

C.2 Recipe for Graphene transfer

1. Cut the graphene/Cu foil into the desired size. Flatten the graphene/Cu film and spin coat a PMMA layer at the speed of 4000 rpm for 45 s.
2. Treat the back side of graphene/Cu film by O_2 Plasma (optional). Use one piece of PDMS to cover the sides of the sample with PMMA. Turn on the vacuum for about a minute, then open 1/8 turn of the vacuum to let the oxygen in. Turn on the plasma and treat the sample for 5 s.
3. Put the PMMA/graphene/Cu film into copper etchant bath for 24 hours.
4. Transfer the PMMA/graphene film (should look clean and completely transparent) into 10% HCL bath for 2 hours to eliminate stubborn residues (optional).
5. Use 3 water baths to clean the PMMA/graphene films.
6. Transferring the graphene onto the desired substrate, leave them dry in air. An additional soft baking on hot plate at 120 °C for 30 min could help to enhance the adhesion between graphene and the substrate.
7. Remove PMMA by either wet baths (acetone/IPA) or thermal annealing beyond 440 °C.

All the water used in this recipe is DI water.

Appendix D

CALCULATIONS RELATED WITH CGR DEVICES

D.1 Calculation for the mobility:

The gate capacitance of graphene devices obeys a linear fit drawn from the equation below, [114]

$$\boldsymbol{C_g} = \frac{n(V_g)e}{V_g - V_{Dirac}} \tag{8}$$

Thus we obtain

$$\boldsymbol{n(V_g)} = \frac{C_g(V_g - V_{Dirac})}{e} \tag{9}$$

We could determine the mobility by

$$\boldsymbol{\mu} = \frac{1}{ne\rho_{xx}} = \frac{1}{C_g(V_g - V_{Dirac})\rho_{xx}} \tag{10}$$

where ρ_{xx} is the sheet resistivity of the device, which could be calculated as

$$\boldsymbol{\rho_{xx}} = R_{xx}(W/L) \tag{11}$$

Noticing that the capacitance could be calculated based on the ionic layers

$$\boldsymbol{C} = \frac{2\epsilon_0 \kappa}{d} \tag{12}$$

where d is the thickness of the ionic layer. For 0.01X PBS, d is around 7.746 nm.

In the calculation, the permittivity of water was used, κ = 79, W/L was estimated as 500 nm/7 μm = 1/14. At Vg = 2 V, Rxx = 7000 Ω.

As a result, the approximate value for the mobility is 450 $cm^2 V^{-1} s^{-1}$.

D.2 Calculation for Seebeck coefficient (conventional method):

$$\boldsymbol{S} = \frac{\pi^2 k_b^2 T}{-3e}\frac{1}{G}\frac{dG}{dV_g}\frac{dV_g}{dE}|_{E=E_F} \tag{13}$$

We can derive from equation (8) that

$$\mathbf{dV_g} = \frac{\mathrm{e}}{\mathrm{C_g}}\mathrm{dn} \tag{14}$$

Thus we obtain

$$\boldsymbol{S} = \frac{\pi^2 k_b^2 T}{-3\mathrm{C_g}}\frac{d(lnG)}{dV_g}\frac{dn}{dE}|_{E=E_F} \tag{15}$$

For single layer graphene

$$\mathrm{E_F} = \hbar \mathrm{v_F}\sqrt{\pi \mathrm{n}} \tag{16}$$

For double layer graphene

$$\mathrm{E_F} = \frac{1}{2}\sqrt{(2\hbar \mathrm{v_F})^2 \pi \mathrm{n} + 2\gamma_1^2 - 2\gamma_1\sqrt{(2\hbar \mathrm{v_F})^2 \pi \mathrm{n} + \gamma_1^2}} \tag{17}$$

where

$\hbar = 6.582\ \times 10^{-16}\mathrm{eV}\cdot \mathrm{s},\ \mathrm{v_F} = 1 \times 10^6 \mathrm{m}\cdot \mathrm{s}^{-1}, \mathrm{n} = 4.464 \times 10^{16}\mathrm{m}^{-2}, \gamma_1 = 0.39\ \mathrm{eV}$

The calculations show that

For single layer graphene, $\frac{dn}{dE}|_{E=E_F} = \ 3.623 \times 10^{17}\mathrm{eV}^{-1}\cdot \mathrm{m}^{-2}$

For double layer graphene, $\frac{dn}{dE}|_{E=E_F} = \ 3.92\ \mathrm{eV}^{-1}\cdot \mathrm{m}^{-2}$

Based on these calculation results, the maximum of the Seebeck coefficient difference is around 5 μV/K. But considering that we can not exactly separate the gating curve of single layer graphene from that of double layer graphene, the Seebeck coefficient drawn by this method may not be accurate.

D3. Alternative method to estimate the Seebeck coefficient:

From equation (7), we could obtain the maximum of the Seebeck coefficient difference as:

$$|\boldsymbol{S_1} - \boldsymbol{S_2}| = \frac{\pi^2 k_b^2 T}{3e} \cdot \frac{1}{\Delta} \tag{18}$$

At T = 400 K and using an estimate for the charge neutrality width $\Delta = 33\text{mV}$ (This value was obtained by directly reading from the raw file of the conductance measurement. The width was estimated by reading the gating range where all the values stay within 5% variance compare with the minimum point), we are able to obtain a value of 125 μV/K.

REFERENCES

1. A. K. Geim and K. S. Novoselov, *Nat Mater*, 2007, **6**, 183-191.
2. Y. Zhao, Y.-H. Kim, A. Dillon, M. Heben and S. Zhang, *Physical Review Letters*, 2005, **94**, 155504.
3. L. Zheng, M. O'connell, S. Doorn, X. Liao, Y. Zhao, E. Akhadov, M. Hoffbauer, B. Roop, Q. Jia and R. Dye, *Nature Materials*, 2004, **3**, 673-676.
4. A. Bianco, K. Kostarelos and M. Prato, *Current Opinion in Chemical Biology*, 2005, **9**, 674.
5. P. Avouris, Z. Chen and V. Perebeinos, *Nature Nanotechnology*, 2007, **2**, 605-615.
6. P. Avouris, M. Freitag and V. Perebeinos, *Nature Photonics*, 2008, **2**, 341-350.
7. H. Shimoda, B. Gao, X. Tang, A. Kleinhammes, L. Fleming, Y. Wu and O. Zhou, *Physical Review Letters*, 2001, **88**, 15502.
8. http://en.wikipedia.org/wiki/Carbon_nanotube.
9. L. Larrimore, Cornell University, 2007.
10. T. Dürkop, S. Getty, E. Cobas and M. Fuhrer, *Nano Letters*, 2004, **4**, 35-39.
11. M. S. Dresselhaus, G. Dresselhaus and P. C. Eklund, *Science of Fullerenes and Carbon Nanotubes: Their properties and Applications*, Academic Press, 1996.
12. T. W. Odom, J.-L. Huang, P. Kim and C. M. Lieber, *Nature*, 1998, **391**, 62-64.
13. M. He, H. Jiang, B. Liu, P. V. Fedotov, A. I. Chernov, E. D. Obraztsova, F. Cavalca, J. B. Wagner, T. W. Hansen and I. V. Anoshkin, *Scientific Reports*, 2013, **3**.

14. J. Liu, C. Wang, X. Tu, B. Liu, L. Chen, M. Zheng and C. Zhou, *Nature Communications*, 2012, **3**, 1199.

15. N. M. Gabor, Z. Zhong, K. Bosnick, J. Park and P. L. McEuen, *Science*, 2009, **325**, 1367-1371.

16. W. Shockley and H. J. Queisser, *Journal of Applied Physics*, 1961, **32**, 510-519.

17. M. Kumar, *Carbon Nanotube Synthesis and Growth Mechanism*, 2011.

18. D. Mendoza, P. Santiago and E. Reyes Pérez, *Revista Mexicana de Física*, 2006, **52**, 1-5.

19. K. Ghosh, M. Kumar, T. Maruyama and Y. Ando, *Carbon*, 2009, **47**, 1565-1575.

20. K. Hata, D. N. Futaba, K. Mizuno, T. Namai, M. Yumura and S. Iijima, *Science*, 2004, **306**, 1362-1364.

21. D. N. Futaba, J. Goto, S. Yasuda, T. Yamada, M. Yumura and K. Hata, *Advanced Materials*, 2009, **21**, 4811-4815.

22. Y. Li, R. Cui, L. Ding, Y. Liu, W. Zhou, Y. Zhang, Z. Jin, F. Peng and J. Liu, *Advanced Materials*, 2010, **22**, 1508-1515.

23. Y. Zhang, W. Zhou, Z. Jin, L. Ding, Z. Zhang, X. Liang and Y. Li, *Chemistry of Materials*, 2008, **20**, 7521-7525.

24. M. J. Allen, V. C. Tung and R. B. Kaner, *Chemical Reviews*, 2010, **110**, 132.

25. Y. Huang, J. Liang and Y. Chen, *Small*, 2012, **8**, 1805-1834.

26. Y. Shao, J. Wang, H. Wu, J. Liu, I. A. Aksay and Y. Lin, *Electroanalysis*, 2010, **22**, 1027-1036.

27. J. Hedberg, http://www.jameshedberg.com/scienceGraphics.php?sort=graphene&id=graphene-lattice-onSubstrate-3Dmodel.

28. A. v. d. Zande, Cornell University, 2011.

29. X. Du, I. Skachko, A. Barker and E. Y. Andrei, *Nature Nanotechnology*, 2008, **3**, 491-495.

30. R. Nair, P. Blake, A. Grigorenko, K. Novoselov, T. Booth, T. Stauber, N. Peres and A. Geim, *Science*, 2008, **320**, 1308-1308.

31. H. P. Boehm, A. Clauss, G. O. Fischer and U. Hofmann, *Zeitschrift für Anorganische und Allgemeine Chemie*, 1962, **316**, 119-127.

32. K. Novoselov, A. Geim, S. Morozov, D. Jiang, Y. Zhang, S. Dubonos, I. Grigorieva and A. Firsov, *Science*, 2004, **306**, 666-669.

33. R. Van Noorden, *Nature*, 2012, **483**, S32-S33.

34. X. Li, W. Cai, J. An, S. Kim, J. Nah, D. Yang, R. Piner, A. Velamakanni, I. Jung and E. Tutuc, *Science*, 2009, **324**, 1312-1314.

35. K. S. Kim, Y. Zhao, H. Jang, S. Y. Lee, J. M. Kim, J. H. Ahn, P. Kim, J. Y. Choi and B. H. Hong, *Nature*, 2009, **457**, 706-710.

36. S. Iijima, *Nature*, 1991, **354**, 56-58.

37. T. Guo, P. Nikolaev, A. Thess, D. Colbert and R. Smalley, *Chemical Physics Letters*, 1995, **243**, 49-54.

38. M. Meyyappan, L. Delzeit, A. Cassell and D. Hash, *Plasma Sources Science and Technology*, 2003, **12**, 205-216.

39. B. L. Allen, P. D. Kichambare and A. Star, *Advanced Materials*, 2007, **19**, 1439-1451.

40. A. Javey, J. Guo, Q. Wang, M. Lundstrom and H. Dai, *Supernovae*, 1999, **118**, 1766-1776.

41. J. Kong, H. T. Soh, A. M. Cassell, C. F. Quate and H. Dai, *Nature*, 1998, **395**, 878-881.

42. K. Hata, D. N. Futaba, K. Mizuno, T. Namai, M. Yumura and S. Iijima, *Science*, 2004, **306**, 1362-1364.

43. Y. Q. Xu, E. Flor, M. J. Kim, B. Hamadani, H. Schmidt, R. E. Smalley and R. H. Hauge, *Journal of the American Chemical Society*, 2006, **128**, 6560-6561.

44. G. Zhang, D. Mann, L. Zhang, A. Javey, Y. Li, E. Yenilmez, Q. Wang, J. P. McVittie, Y. Nishi and J. Gibbons, *Proceedings of the National Academy of Sciences of the United States of America*, 2005, **102**, 16141-16145.

45. Y. Hayamizu, T. Yamada, K. Mizuno, R. C. Davis, D. N. Futaba, M. Yumura and K. Hata, *Nature Nanotechnology*, 2008, **3**, 289-294.

46. A. Izadi-Najafabadi, T. Yamada, D. N. Futaba, H. Hatori, S. Iijima and K. Hata, *Electrochemistry Communications*, 2010, **12**, 1678-1681.

47. T. J. Simmons, D. Hashim, R. Vajtai and P. M. Ajayan, *Journal of the American Chemical Society*, 2007, **129**, 10088-10089.

48. W. Zhou, L. Ding, S. Yang and J. Liu, *Journal of the American Chemical Society*, 2009, **132**, 336-341.

49. J. Zhang, X. Wang, W. Yang, W. Yu, T. Feng, Q. Li, X. Liu and C. Yang, *Carbon*, 2006, **44**, 418-422.

50. S. Huang, M. Woodson, R. Smalley and J. Liu, *Nano Letters*, 2004, **4**, 1025-1028.

51. G. Eres, A. A. Kinkhabwala, H. Cui, D. B. Geohegan, A. A. Puretzky and D. H. Lowndes, *The Journal of Physical Chemistry B*, 2005, **109**, 16684-16694.

52. X. Fan, R. Buczko, A. A. Puretzky, D. B. Geohegan, J. Y. Howe, S. T. Pantelides and S. J. Pennycook, *Physical Review Letters*, 2003, **90**, 145501.

53. H. Qi, D. Yuan and J. Liu, *The Journal of Physical Chemistry C*, 2007, **111**, 6158-6160.

54. Y. Shibuta and S. Maruyama, *Chemical Physics Letters*, 2003, **382**, 381-386.

55. H. Zhu, K. Suenaga, A. Hashimoto, K. Urita, K. Hata and S. Iijima, *Small*, 2005, **1**, 1180-1183.

56. C. L. Pint, N. Nicholas, S. T. Pheasant, J. G. Duque, A. N. G. Parra-Vasquez, G. Eres, M. Pasquali and R. H. Hauge, *The Journal of Physical Chemistry C*, 2008, **112**, 14041-14051.

57. D. Mehn, A. Fonseca, G. Bister and J. Nagy, *Chemical Physics Letters*, 2004, **393**, 378-384.

58. W. Wang, X. Bai, Z. Xu, S. Liu and E. Wang, *Chemical Physics Letters*, 2006, **419**, 81-85.

59. A. J. Hart, A. H. Slocum and L. Royer, *Carbon*, 2006, **44**, 348-359.

60. S. K. Doorn, M. J. O'Connell, L. Zheng, Y. T. Zhu, S. Huang and J. Liu, *Physical Review Letters*, 2005, **94**, 16802.

61. S. K. Doorn, L. Zheng, J. O. C. Michael, Y. Zhu, S. Huang and J. Liu, *The Journal of Physical Chemistry B*, 2005, **109**, 3751-3758.

62. A. Jorio, R. Saito, J. Hafner, C. Lieber, M. Hunter, T. McClure, G. Dresselhaus and M. Dresselhaus, *Physical Review Letters*, 2001, **86**, 1118-1121.

63. M. S. Dresselhaus, G. Dresselhaus, R. Saito and A. Jorio, *Physics Reports*, 2005, **409**, 47-99.

64. A. Star, E. Tu, J. Niemann, J. C. P. Gabriel, C. S. Joiner and C. Valcke, *Proceedings of the National Academy of Sciences of the United States of America*, 2006, **103**, 921-926.

65. S. Sorgenfrei, C. Chiu, R. L. Gonzalez Jr, Y. J. Yu, P. Kim, C. Nuckolls and K. L. Shepard, *Nature Nanotechnology*, 2011, **6**, 126-132.

66. C. Klinke, J. Chen, A. Afzali and P. Avouris, *Nano Letters*, 2005, **5**, 555-558.

67. A. Star, J. C. P. Gabriel, K. Bradley and G. Grüner, *Nano Letters*, 2003, **3**, 459-463.

68. A. Star, V. Joshi, T. R. Han, M. V. P. Altoé, G. Grüner and J. F. Stoddart, *Organic Letters*, 2004, **6**, 2089-2092.

69. K. Bradley, A. Davis, J. C. P. Gabriel and G. Grüner, *Nano Letters*, 2005, **5**, 841-845.

70. S. Rosenblatt, Y. Yaish, J. Park, J. Gore, V. Sazonova and P. L. McEuen, *Nano Letters*, 2002, **2**, 869-872.

71. K. Balasubramanian, M. Burghard, K. Kern, M. Scolari and A. Mews, *Nano Letters*, 2005, **5**, 507-510.

72. A. J. Bard and L. R. Faulkner, *Electrochemical Methods: Fundamentals and Applications*, Wiley New York, 1980.

73. J. M. Bockris, M. Devanathan and K. Muller, *Proceedings of the Royal Society of London. Series A. Mathematical and Physical Sciences*, 1963, **274**, 55-79.

74. Y. Wu, K. A. Jenkins, A. Valdes-Garcia, D. B. Farmer, Y. Zhu, A. A. Bol, C. Dimitrakopoulos, W. Zhu, F. Xia and P. Avouris, *Nano Letters*, 2012, **12**, 3062-3067.

75. F. Bonaccorso, Z. Sun, T. Hasan and A. Ferrari, *Nature Photonics*, 2010, **4**, 611-622.

76. K. Novoselov, A. K. Geim, S. Morozov, D. Jiang, M. K. I. Grigorieva, S. Dubonos and A. Firsov, *Nature*, 2005, **438**, 197-200.

77. Y. Wu, Y.-m. Lin, A. A. Bol, K. A. Jenkins, F. Xia, D. B. Farmer, Y. Zhu and P. Avouris, *Nature*, 2011, **472**, 74-78.

78. P. Shemella, Y. Zhang, M. Mailman, P. M. Ajayan and S. K. Nayak, *Applied Physics Letters*, 2007, **91**, 042101-042101-042103.

79. Y.-W. Son, M. L. Cohen and S. G. Louie, *Physical Review Letters*, 2006, **97**, 216803.

80. W. Zhu, T. Low, V. Perebeinos, A. A. Bol, Y. Zhu, H. Yan, J. Tersoff and P. Avouris, *Nano Letters*, 2012, **12**, 3431-3436.

81. L. Ortolani, E. Cadelano, G. P. Veronese, C. Degli Esposti Boschi, E. Snoeck, L. Colombo and V. Morandi, *Nano Letters*, 2012, **12**, 5207-5212.

82. J. Zang, S. Ryu, N. Pugno, Q. Wang, Q. Tu, M. J. Buehler and X. Zhao, *Nature Materials*, 2013, **12**, 321-325.

83. X. Xie, L. Ju, X. Feng, Y. Sun, R. Zhou, K. Liu, S. Fan, Q. Li and K. Jiang, *Nano Letters*, 2009, **9**, 2565-2570.

84. J. D. Peterson, S. Vyazovkin and C. A. Wight, *The Journal of Physical Chemistry B*, 1999, **103**, 8087-8092.

85. H. Arisawa and T. Brill, *Combustion and Flame*, 1997, **109**, 415-426.

86. N. Liu, Z. Pan, L. Fu, C. Zhang, B. Dai and Z. Liu, *Nano Research*, 2011, **4**, 996-1004.

87. S. P. Koenig, N. G. Boddeti, M. L. Dunn and J. S. Bunch, *Nature Nanotechnology*, 2011, **6**, 543-546.

88. G. Madras, J. Smith and B. J. McCoy, *Industrial & Engineering Chemistry Research*, 1996, **35**, 1795-1800.

89. T. Mueller, F. Xia, M. Freitag, J. Tsang and P. Avouris, *Physical Review B*, 2009, **79**, 245430.

90. E. J. Lee, K. Balasubramanian, R. T. Weitz, M. Burghard and K. Kern, *Nature Nanotechnology*, 2008, **3**, 486-490.

91. A. Gupta, G. Chen, P. Joshi, S. Tadigadapa and P. Eklund, *Nano Letters*, 2006, **6**, 2667-2673.

92. D. Graf, F. Molitor, K. Ensslin, C. Stampfer, A. Jungen, C. Hierold and L. Wirtz, *Nano Letters*, 2007, **7**, 238-242.

93. P. Avouris, *Nano Letters*, 2010, **10**, 4285-4294.

94. S. Bae, H. Kim, Y. Lee, X. F. Xu, J. S. Park, Y. Zheng, J. Balakrishnan, T. Lei, H. R. Kim, Y. I. Song, Y. J. Kim, K. S. Kim, B. Ozyilmaz, J. H. Ahn, B. H. Hong and S. Iijima, *Nature Nanotechnology*, 2010, **5**, 574-578.

95. T. Mueller, F. N. A. Xia and P. Avouris, *Nature Photonics*, 2010, **4**, 297-301.

96. J. Park, Y. H. Ahn and C. Ruiz-Vargas, *Nano Letters*, 2009, **9**, 1742-1746.

97. C. H. Lui, K. F. Mak, J. Shan and T. F. Heinz, *Physical Review Letters*, 2010, **105**, 127404.

98. Z. P. Sun, T. Hasan, F. Torrisi, D. Popa, G. Privitera, F. Q. Wang, F. Bonaccorso, D. M. Basko and A. C. Ferrari, *ACS Nano*, 2010, **4**, 803-810.

99. N. M. Gabor, J. C. W. Song, Q. Ma, N. L. Nair, T. Taychatanapat, K. Watanabe, T. Taniguchi, L. S. Levitov and P. Jarillo-Herrero, *Science*, 2011, **334**, 648-652.

100. D. Sun, G. Aivazian, A. M. Jones, J. S. Ross, W. Yao, D. Cobden and X. D. Xu, *Nature Nanotechnology*, 2012, **7**, 114-118.

101. M. C. Lemme, F. H. L. Koppens, A. L. Falk, M. S. Rudner, H. Park, L. S. Levitov and C. M. Marcus, *Nano Letters*, 2011, **11**, 4134-4137.

102. C. F. Chen, C. H. Park, B. W. Boudouris, J. Horng, B. S. Geng, C. Girit, A. Zettl, M. F. Crommie, R. A. Segalman, S. G. Louie and F. Wang, *Nature*, 2011, **471**, 617-620.

103. P. Koskinen, *Applied Physics Letters*, 2011, **99**, 013105.

104. O. O. Kit, T. Tallinen, L. Mahadevan, J. Timonen and P. Koskinen, *Physical Review B*, 2012, **85**, 085428.

105. S. Cranford and M. J. Buehler, *Model Simul Mater Sc*, 2011, **19**, 054003.

106. K. V. Bets and B. I. Yakobson, *Nano Research*, 2009, **2**, 161-166.

107. A. Sadrzadeh, M. Hua and B. I. Yakobson, *Applied Physics Letters*, 2011, **99**, 013102.

108. L. M. Viculis, J. J. Mack and R. B. Kaner, *Science*, 2003, **299**, 1361-1361.

109. J. D. Peterson, S. Vyazovkin and C. A. Wight, *J Phys Chem B*, 1999, **103**, 8087-8092.

110. J. D. Peterson, S. Vyazovkin and C. A. Wight, *Macromol Rapid Comm*, 1999, **20**, 480-483.

111. S. Das Sarma, S. Adam, E. H. Hwang and E. Rossi, *Rev Mod Phys*, 2011, **83**, 407-470.

112. A. Luican, G. H. Li and E. Y. Andrei, *Solid State Commun*, 2009, **149**, 1151-1156.

113. D. Nezich, A. Reina and J. Kong, *Nanotechnology*, 2012, **23**, 015701.

114. A. Newaz, Y. S. Puzyrev, B. Wang, S. T. Pantelides and K. I. Bolotin, *Nature Communications*, 2012, **3**, 734.